Finite Element Analysis and Experiments on Vibration Control of Flexible Manipulators Using Piezoelectric Actuators

Abdul Kadir Muhammad

June 2015

Summary

Employment of flexible manipulators is recommended in the space and industrial applications in order to accomplish high performance requirements such as high-speed besides safe operation, increasing of positioning accuracy, and lower energy consumption, namely less weight. However, it is not usually easy to control a flexible manipulator because of its inheriting flexibility. Deformation of the flexible manipulator when it is operated must be considered by any control. Its controller system should be dealt with not only its motion but also vibration due to the flexibility of the link.

The main subjects of this research are modeling and designing of controllers to suppress vibration of flexible single-link and two-link manipulators. The manipulator systems with flexible links are continuous dynamical systems that have continuous distributions of mass and elasticity. Such systems are characterized by an infinite number of degrees of freedom. Therefore, finite element method was chosen in modeling and designing of controllers for the systems using one-dimensional and two-node element type. For controller, active-force (AF) control, a kind of robust control, was chosen and designed to deal with uncertainty. The performances of the AF-control were compared with the classical proportional (P) and proportional-derivative (PD) controls.

The single-link flexible manipulator used in this research consists of an aluminum beam as a flexible link, a clamp-part, a servo motor to rotate the link, a piezoelectric actuator to control vibration and a base. Modeling of the system was prefaced by kinematics analysis in global and rotational coordinate frames. Equations of motion of the flexible single-link manipulator were derived using finite element method. Computational codes on time history responses, Fast Fourier Transform (FFT) processing and eigenvalues - eigenvectors analysis were developed to calculate the dynamic behavior of the link. An end-effector that treated as a concentrated mass was introduced to demonstrate a complete flexible single-link manipulator system. Furthermore, a control scheme using a piezoelectric actuator was designed to suppress the vibration of the system. A proportional (P), a proportional-derivative (PD) and an active-force (AF) controls strategies were designed and compared their performances through the calculations and experiments. Based on the calculated results, the effect of D-controller was very small compared to P-controller, therefore using a P-controller is sufficient for experiment. The calculated and experimental results show the superiority of the proposed AF- control compared to the P and PD ones to suppress the vibration of the flexible single-link manipulator.

The flexible two-link manipulator used in this research consists of two aluminum beams as flexible links, two clamp-parts, two servo motors to rotate the links, piezoelectric actuators to control vibration and a base. Modeling of the system was prefaced by kinematics analysis in global and rotational coordinate frames. Equations of motion of the flexible two-link manipulator were derived using finite element method. Computational codes on time history responses, FFT processing and eigenvalues - eigenvectors analysis were developed to calculate the dynamic behavior of the links. An end-effector that treated as a concentrated mass was introduced to demonstrate a complete flexible two-link manipulator system. Furthermore, a control scheme using one and two piezoelectric actuators was designed to suppress the vibration of the system. Two proportional, two proportional-derivative and two active-force controls strategies were designed and compared their performances through the calculations and experiments. Based on the calculated results, the effect of the second piezoelectric actuator was small compare to the first one. Therefore, using one piezoelectric actuator is sufficient for experiment. The calculated and experimental results have revealed that the proposed control scheme can effectively suppress the vibration of the flexible two-link manipulator even though using only one piezoelectric actuator as well as the effectiveness of the proposed PD-control compared to the P and AF ones to suppress the vibration of the system.

Contents

Chapter 1

Introduction

1.1 Background

Employment of flexible manipulators is recommended in the space and industrial applications in order to accomplish high performance requirements such as high-speed besides safe operation, increasing of positioning accuracy, and lower energy consumption, namely less weight. However, it is not usually easy to control a flexible manipulator because of its inheriting flexibility. Deformation of the flexible manipulator when it is operated must be considered by any control. Its controller system should be dealt with not only its motion but also vibration due to the flexibility of the link.

The main subjects of this research are modeling and designing of controllers to suppress vibration of flexible single-link and two-link manipulators using piezoelectric actuators. The manipulator systems with flexible links are continuous dynamical systems that have continuous distributions of mass and elasticity. Such systems are characterized by an infinite number of degrees of freedom. Therefore, finite element method was chosen in modeling and designing controllers for the systems. For controller, active-force (AF) control, a kind of robust control, was chosen and designed to deal with uncertainty of the systems. The performances of the AF-control were compared with the classical proportional (P) and proportional-derivative (PD) controls.

1.2 Literature Review

A review of published papers dealing with the use of finite element analysis (FEA) on modeling and designing of controllers for active vibration suppression of flexible manipulators is given in this sub chapter. The papers were reviewed based on the purposes of this research. The summary of the literature review is shown in Fig. 1.1.

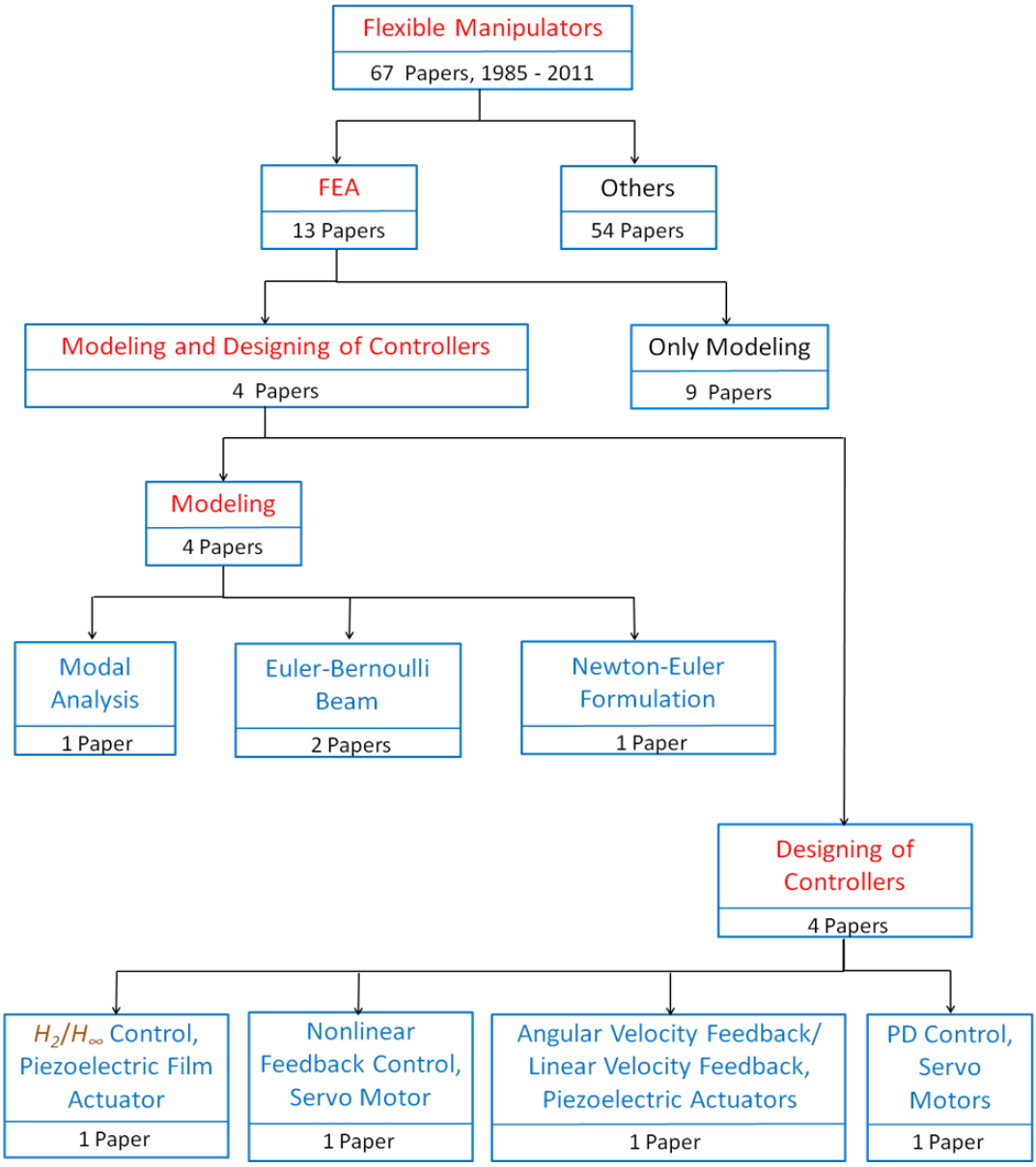

Fig. 1.1 Summary of the literature review

There are 67 [1-67] papers discussed about flexible manipulators reached by the author. The reviewed papers were published in year of 1985-2011. As far as the author reached, there are 13 of the reviewed papers [1-13] dealt with the use of FEA on modeling and designing of controllers for active vibration suppression of flexible manipulators. There are 9 of the FEA papers [5-13] discussed about dynamic modeling of flexible manipulators but only 4 of the FEA papers [1-4] discussed about dynamic modeling as well as designing controllers on active vibration suppression of flexible manipulators.

A modeling method of the flexible multibody systems based on modal analysis using finite element was utilized by Nishidome and Kajiwara [1] for a flexible two-link manipulator. The model was described as a state space form. Gurses et al [2] as well as Ge et al [3] used the Euler-Bernoulli beam theory in modeling of a flexible single-link manipulator. Gammara-Rosado and Yuhara [4] derived dynamic equations of a flexible two-link manipulator using the Newton-Euler formulation and finite element analysis based on elementary beam theory.

Nishidome and Kajiwara [1] constructed their control system with a designed dynamic compensator based on the mixed of H_2/H_∞. They used two servo motors to rotate the manipulator and two piezoelectric films as sensor and actuator for vibration suppression of the flexible two-link manipulator. They showed the effectiveness of their technique through calculations and experiments. Gurses et al [2] used angular velocity feedback control (AVF), linear velocity feedback (LVF) control and the combination of the AVF and LVF to suppress vibration of a flexible single-link manipulator by three piezoelectric actuators. The effectiveness of their results was shown by simulations and experiments. Ge et al [3] employed a nonlinear feedback controller for a motor to drive

and suppress vibration of a flexible single-link manipulator. They showed the effectiveness of their technique through calculations. Gammara-Rosado and Yuhara [4] used proportional-derivative (PD) controller for two motors to rotate and suppress vibration of a flexible two-link manipulator. The effectiveness of their results was shown by simulations.

1.3 Purposes of Research

The purposes of this research are listed as follows

1. To derive equations of motion of flexible single-link and two-link manipulators by finite element method.
2. To develop the computational codes in order to perform dynamics simulations with vibration control for flexible single-link and two-link manipulators.
3. To propose an effective control scheme for flexible single-link and two-link manipulators using three control strategies, namely proportional, proportional-derivative and active-force controls.
4. To confirm the calculated results by experiments of flexible single-link and two-link manipulators.

1.4 Structure of Dissertation

The dissertation is structured in the following manner. Chapter 1 presents the background, literature review, purposes of the research and structure of the dissertation. The literature review is addressed to the use of finite element method in modeling and designing controllers to suppress vibration of flexible manipulators.

Chapter 2 presents a study of computational simulations on vibration control of a flexible single-link manipulator using finite element analysis. Modeling of the system was prefaced by kinematics analysis in global and rotational coordinate frames. Equations of motion of the flexible single-link manipulator were derived using finite element method based on one-dimensional and two-node element. Dynamic simulations of the system with vibration control were performed using three types of computational models. The vibration control scheme with a piezoelectric actuator is presented using three control strategies. Calculated uncontrolled and controlled time history responses for the flexible single-link systems are presented to show the effectiveness of the proposed control scheme and strategies to suppress the vibration of the system. In

Chapter 3 presents an experimental study on vibration control of a flexible single-link manipulator using a piezoelectric actuator. The experiments were carried out to validate the formulation, computational codes and modeling of the flexible single-link manipulator presented in chapter 2. Experimental set-up and method are also presented in this chapter. Dynamic measurements of the system with vibration control are carried out using two types of experimental models. Experimental uncontrolled and controlled time history responses for the flexible single-link systems are presented to show the validity of the proposed control scheme and strategies to suppress the vibration of the system.

Chapter 4 presents a study of computational simulations on vibration control of a flexible two-link manipulator using finite element analysis. Modeling of the system was prefaced by kinematics analysis in global and rotational coordinate frames. Equations of motion of the flexible two-link manipulator were derived using finite element method based on one-dimensional and two-node element type. Dynamic simulations of the

system with vibration control were performed using four types of computational models. The vibration control scheme with one and two piezoelectric actuators is presented using three control strategies. Calculated uncontrolled and controlled time history responses for the flexible two-link systems are presented to show the effectiveness of the proposed control scheme and strategies to suppress the vibration of the system.

Chapter 5 presents an experimental study on vibration control of a flexible two-link manipulator using a piezoelectric actuator. The experiments were carried out to validate the formulation, computational codes and modeling of the flexible two-link manipulator presented in chapter 3. Experimental set-up and method are also presented in this chapter. Dynamic measurements of the system with vibration control are carried out using three types of experimental models. Experimental uncontrolled and controlled time history responses for the flexible single-link systems are presented to show the validity of the proposed control scheme and strategies to suppress the vibration of the system.

Finally, chapter 6 presents conclusions of the research. Additionally, references of reviewed literature and a list of publications as core of the dissertation are given.

Chapter 2

Formulation and Computational Simulations on Vibration Control of a Flexible Single-link Manipulator Using Finite Element Method

2.1 Introduction

The purposes of study presented in this chapter are to derive the equations of motion of a flexible single-link system by a finite element method, to develop the computational codes in order to perform dynamics simulations with vibration control and to propose an effective control scheme of a flexible single-link manipulator using three control strategies, namely proportional (P), proportional-derivative (PD) and active-force (AF) controls.

The flexible manipulator used in this chapter consists of an aluminum beam as a flexible link, a clamp-part, a servo motor to rotate the link, a piezoelectric actuator to control vibration and a base. Computational codes on time history responses, FFT (Fast Fourier Transform) processing and eigenvalues - eigenvectors analysis were developed to calculate the dynamic behavior of the link. An end-effector that treated as a concentrated mass was introduced to demonstrate a complete flexible single-link manipulator system. Furthermore, the P, PD and AF controls strategies were designed to suppress the vibration of the system. It was done by adding bending moments generated

by the piezoelectric actuator to the single-link. Finally, their performances were compared through the calculations.

2.2 Formulation by Finite Element Method

The link has been discretized by finite elements. Every finite element (Element *i*-th) has two nodes namely Node *i* and Node (*i*+1). Every node (Node *i*) has two degrees of freedom, namely the lateral deformation $v_i(x,t)$, and the rotational angle $\psi_i(x,t)$. The length, the cross-sectional area and the area moment of inertia around *z*-axis of every element are denoted by l_i, S_i and I_{zi} respectively. Mechanical properties of every element are denoted as Young's modulus E_i and mass density ρ_i.

2.2.1 Kinematics

Figure 2.1 shows the position vector of an arbitrary point *P* in the link in the global and rotating coordinate frames. Let the link as a flexible beam has a motion that is confined in the horizontal plane as shown in Fig. 2.1. The *O* – *XY* frame is the global coordinate frame while *O* – *xy* is the rotating coordinate frame fixed to the root of the link (*z*-axis is fixed). The unit vectors in *X*, *Y*, *x* and *y* axes are denoted by ***I***, ***J***, ***i*** and ***j***, respectively. A motor is installed on the root of the link. The rotational angle of the motor when the link rotates is denoted by $\theta(t)$. The position vector $\boldsymbol{r}(x,t)$ of the arbitrary point *P* in the link at time $t = t$, measured in the *O* – *XY* frame shown in figure 1 is expressed by

$$\boldsymbol{r}(x,t) = X(x,t)\boldsymbol{I} + Y(x,t)\boldsymbol{J}\,, \tag{2.1}$$

where

$$X(x,t) = x\cos\theta(t) - v(x,t)\sin\theta(t)\,, \tag{2.2}$$

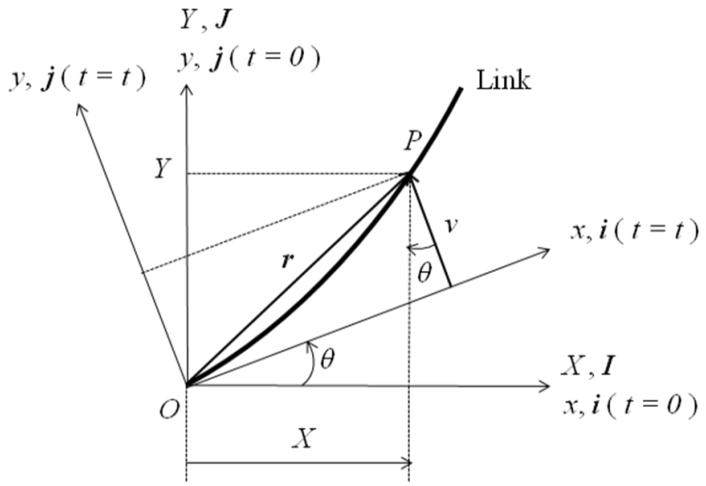

$O - XY$: Global coordinate frame
$O - xy$: Rotating coordinate frame

Fig. 2.1 Position vector of an arbitrary point P on the link in the global and rotating coordinate frames

and

$$Y(x,t) = x\sin\theta(t) + v(x,t)\cos\theta(t)\,. \tag{2.3}$$

The velocity of P is given by

$$\dot{\boldsymbol{r}}(x,t) = \dot{X}(x,t)\boldsymbol{I} + \dot{Y}(x,t)\boldsymbol{J}\,. \tag{2.4}$$

2.2.2 Finite Element Procedure

Figure 2.2 shows the rotating coordinate frame and the link divided by one-dimensional and two-node elements. Then, Fig. 2.3 shows the element coordinate frame of Element i, and an arbitrary point P in Element i. Here, there are four boundary conditions together at nodes i and (i+1) when the one-dimensional and two-node element is used. The four boundary conditions are expressed as nodal deformation vector as follow

$$\boldsymbol{\delta}_i = \begin{Bmatrix} v_i & \psi_i & v_{i+1} & \psi_{i+1} \end{Bmatrix}^T, \tag{2.5}$$

Then, the hypothesized deformation has four constants as follows [69]

$$v_i = a_1 + a_2 x_i + a_3 x_i^{\,2} + a_4 x_i^{\,3}, \tag{2.6}$$

where x_i is position coordinate of the arbitrary point P in the x_i-axis of the element coordinate frame. Furthermore, the relation between the lateral deformation v_i and the rotational angle ψ_i of the Node i is given by

$$\psi_i = \frac{\partial v_i}{\partial x_i}. \tag{2.7}$$

Substituting Eq. (2.6) to Eq. (2.7) gives

$$\psi_i = a_2 + 2a_3 x_i + 3a_4 x_i^{\,2}, \tag{2.8}$$

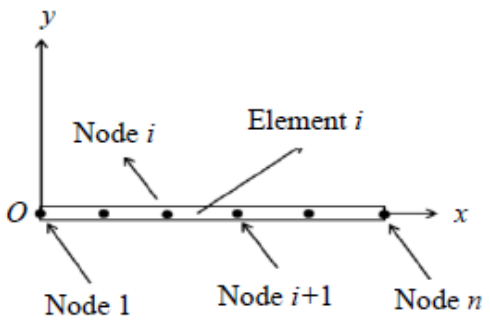

$O - xy$: Rotating coordinate frame

Fig.2.2 Rotating coordinate frame and the link divided by the one-dimensional and two-node elements

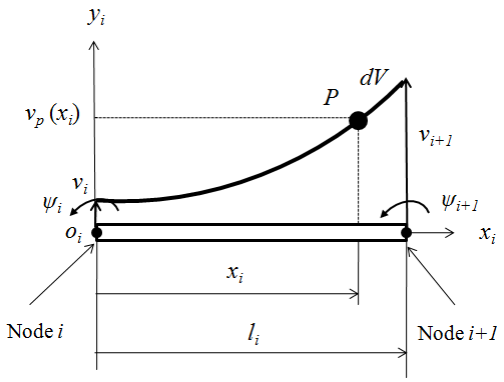

$o_i - x_i\, y_i$: Element coordinate frame of Element i

Fig.2.3 Element coordinate frame of Element i

The constants can be obtained from the values of v_i and ψ_i at Node i, $x_i = 0$, and at Node (i+1), $x_i = l_i$, that are

$$a_1 = v_i\,, \tag{2.9}$$

$$a_2 = \psi_i\,, \tag{2.10}$$

$$a_3 = \frac{1}{l_i^{\,2}}\left(-3v_i + 3v_{i+1} - 2\psi_i l_i - \psi_{i+1} l_i\right), \tag{2.11}$$

$$a_4 = \frac{1}{l_i^{\,3}}\left(2v_i - 2v_{i+1} + \psi_i l_i + \psi_{i+1} l_i\right). \tag{2.12}$$

Substituting Eqs. (1.9), (1.10), (1.11) and (1.12) to Eq. (1.6) gives

$$v_i(x_i) = \left\{1 - \frac{3x_i^{\,2}}{l_i^{\,2}} + \frac{2x_i^{\,3}}{l_i^{\,3}}, x - \frac{2x_i^{\,2}}{l_i} + \frac{x_i^{\,3}}{l_i^{\,2}}, \quad \frac{3x_i^{\,2}}{l_i^{\,2}} - \frac{2x_i^{\,3}}{l_i^{\,3}}, -\frac{2x_i^{\,2}}{l_i} + \frac{x_i^{\,3}}{l_i^{\,2}}\right\} \begin{Bmatrix} v_i \\ \psi_i \\ v_{i+1} \\ \psi_{i+1} \end{Bmatrix}, \tag{2.13}$$

where

$$v_i(x_i) = \boldsymbol{N}\boldsymbol{\delta_i}\,. \tag{2.14}$$

Corresponding to Eq. (2.14), the shape function matrix, $\boldsymbol{N}$ can be observed on Eq. (2.13) as follows

$$\boldsymbol{N} = \left\{1 - \frac{3x_i^{\,2}}{l_i^{\,2}} + \frac{2x_i^{\,3}}{l_i^{\,3}}, x - \frac{2x_i^{\,2}}{l_i} + \frac{x_i^{\,3}}{l_i^{\,2}}, \quad \frac{3x_i^{\,2}}{l_i^{\,2}} - \frac{2x_i^{\,3}}{l_i^{\,3}}, -\frac{2x_i^{\,2}}{l_i} + \frac{x_i^{\,3}}{l_i^{\,2}}\right\}. \tag{2.15}$$

Moreover, from mechanics of materials, the strain of Node i can be defined by

$$\varepsilon_i = -y_i \frac{\partial^2 v_i}{\partial x_i^{\,2}}, \tag{2.16}$$

where y_i is position coordinate of the arbitrary point P in the y_i-axis of the element coordinate frame.

The strains ε_i is related to the nodal deformation vector $\boldsymbol{\delta}_i$ of Element i by $\boldsymbol{B}_i$ - matrix as follows

$$\varepsilon_i = \boldsymbol{B}_i \boldsymbol{\delta}_i . \tag{2.17}$$

Substituting second derivative of Eq. (2.13) into Eq. (2.16) gives

$$\varepsilon_i = y_i \left\{ \frac{6}{l_i^2} - \frac{12x_i}{l_i^3}, \frac{4}{l_i} - \frac{6x_i}{l_i^2}, \quad -\frac{6}{l_i^2} + \frac{12x_i}{l_i^3}, \frac{2}{l_i} - \frac{6x_i}{l_i^2} \right\} \begin{Bmatrix} v_i \\ \psi_i \\ v_{i+1} \\ \psi_{i+1} \end{Bmatrix}. \tag{2.18}$$

Corresponding to Eq. (2.17), $\boldsymbol{B}_i$ –matrix can be observed on Eq. (2.18) as follows

$$\boldsymbol{B}_i = \left\{ -\frac{6}{l_i^2} + \frac{12x_i}{l_i^3}, -\frac{4}{l_i} + \frac{6x_i}{l_i^2}, \quad \frac{6}{l_i^2} - \frac{-12x_i}{l_i^3}, -\frac{2}{l_i} + \frac{6x_i}{l_i^2} \right\}, \tag{2.19}$$

Furthermore, the stress and strain of Element i are related by

$$\sigma_i = \boldsymbol{D}_i \varepsilon_i , \tag{2.20}$$

where $\boldsymbol{D}_i$ is a square symmetric matrix that depends on the mechanical properties of Element i, in this case can be reduced as Young's modulus E.

2.2.3 Kinetic Energy

The kinetic energy for Element i is defined as [68]

$$\boldsymbol{T}_i = \frac{1}{2} \int_{V_i} \rho_i \dot{\boldsymbol{r}}^T \dot{\boldsymbol{r}} dV , \tag{2.21}$$

where ρ_i and V_i are the mass density and volume of Element i, respectively.

Then, based on Eqs. (2.3), (2.4) and (2.5), the velocity square of P can be obtained as

$$\dot{\boldsymbol{r}}^T \dot{\boldsymbol{r}}(x,t) = x^2 \dot{\theta}^2 + \dot{v}^2 + v^2 \dot{\theta}^2 + 2x\dot{v}\dot{\theta} . \tag{2.22}$$

Moreover, the value of x can be defined as follow

$$x = l_{1-i} + x_i , \tag{2.23}$$

where l_{1-i} is length from Node 1 to Node i

$$l_{1-i} = l_1 + l_2 + ... + l_{i-1} . \tag{2.24}$$

Substituting Eq. (2.23) to Eq. (2.22) gives

$$\dot{\boldsymbol{r}}^T \dot{\boldsymbol{r}}(x_i, t) = (l_{1-i} + x_i)^2 \dot{\theta}^2 + \dot{v}^2 + v^2 \dot{\theta}^2 + 2(l_{1-i} + x_i)\dot{v}\dot{\theta}, \tag{2.25}$$

Substituting Eq. (2.25) to Eq. (2.21) gives the kinetic energy for Element i of the link as follows

$$\boldsymbol{T}_i = \frac{7}{6} m_i {l_{1-i}}^2 \dot{\theta}^2 + \frac{1}{2} \dot{\boldsymbol{\delta}}_i^T \boldsymbol{M}_i \dot{\boldsymbol{\delta}}_i + \frac{1}{2} \boldsymbol{\delta}_i^T \dot{\theta}^2 \boldsymbol{M}_i \boldsymbol{\delta}_i + \dot{\theta} \boldsymbol{f}_i^T \dot{\boldsymbol{\delta}}_i , \tag{2.26}$$

where

$$\boldsymbol{f}_i^T = \frac{\rho_i S_i l_i}{60} \begin{Bmatrix} 30l_{1-i} + 9l_i & 5l_{1-i}l_i + 2{l_i}^2 & 21l_i & -5l_{1-i}l_i + 3{l_i}^2 \end{Bmatrix}. \tag{2.27}$$

Furthermore, the mass matrix $\boldsymbol{M}_i$ of Element i can be expressed as

$$\boldsymbol{M}_i = \rho_i \int_{V_i} \boldsymbol{N}^T \boldsymbol{N}_i dV_i = \rho_i \int_0^{l_i} \boldsymbol{N}^T \boldsymbol{N}_i S_i dx_i . \tag{2.28}$$

Substituting Eq. (2.15) to Eq. (2.28) gives

$$\boldsymbol{M}_i = \frac{\rho_i S_i l_i}{420} \begin{bmatrix} 156 & 22l_i & 54 & -13l_i \\ 22l_i & 4{l_i}^2 & 13l_i & -3{l_i}^2 \\ 54 & 13l_i & 156 & -22l_i \\ -13l_i & -3{l_i}^2 & -22l_i & 4{l_i}^2 \end{bmatrix}. \tag{2.29}$$

2.2.4 Strain Energy

The strain energy for Element i is defined as [68]

$$\boldsymbol{U}_i = \frac{1}{2} \int_{V_i} {\varepsilon_i}^T \sigma_i dV_i . \tag{2.30}$$

Substituting Eqs. (2.17) and (2.20) to Eq. (2.30) gives

$$\boldsymbol{U}_i = \frac{1}{2}\boldsymbol{\delta}_i^T \left[\int_\tau \boldsymbol{B}_i^T \boldsymbol{D}_i \boldsymbol{B}_i d\tau \right] \boldsymbol{\delta}_i . \tag{2.31}$$

Equation (2.31) can be rewritten as

$$\boldsymbol{U}_i = \frac{1}{2}\boldsymbol{\delta}_i^T \boldsymbol{K}_i \boldsymbol{\delta}_i . \tag{2.32}$$

Substituting Eq. (2.17) and E to Eq. (2.31) within integral limit of 0 to l_i gives

$$\boldsymbol{U}_i = \frac{1}{2}\frac{E_i I_{z_i}}{l_i^3} \begin{Bmatrix} v_i \\ \psi_i \\ v_{i+1} \\ \psi_{i+1} \end{Bmatrix}^T \begin{bmatrix} 12 & 6l_i & -12 & 6l_i \\ 6l_i & 4l_i^2 & -6l_i & 2l_i^2 \\ -12 & -6l_i & 12 & -6l_i \\ 6l_i & 2l_i^2 & -6l_i & 4l_i^2 \end{bmatrix} \begin{Bmatrix} v_i \\ \psi_i \\ v_{i+1} \\ \psi_{i+1} \end{Bmatrix}. \tag{2.33}$$

Corresponding to Eq. (2.32), the stiffness matrix $\boldsymbol{K}_i$ can be observed on Eq. (2.33) as follows

$$\boldsymbol{K}_i = \frac{E_i I_{zi}}{l_i^3} \begin{bmatrix} 12 & 6l_i & -12 & 6l_i \\ 6l_i & 4l_i^2 & -6l_i & 2l_i^2 \\ -12 & -6l_i & 12 & -6l_i \\ 6l_i & 2l_i^2 & -6l_i & 4l_i^2 \end{bmatrix}. \tag{2.34}$$

2.2.5 Equations of Motion

Substituting Eqs. (2.26) and (2.32) into Lagrange's equation, the equation of motion for Element *i* of the link can be obtained as follows

$$\boldsymbol{M}_i \ddot{\boldsymbol{\delta}}_i + \boldsymbol{C}_i \dot{\boldsymbol{\delta}}_i + \left[\boldsymbol{K}_i - \dot{\theta}^2 \boldsymbol{M}_i \right] \boldsymbol{\delta}_i = \ddot{\theta} \boldsymbol{f}_i . \tag{2.35}$$

The damping matrix $\boldsymbol{C_i}$ for Element *i* can be calculated by using the Rayleigh damping factor α as follows

$$\boldsymbol{C}_i = \alpha \boldsymbol{K}_i . \tag{2.36}$$

Finally, for the whole link which is discretized as *n* elements, the sum of kinetic and strain energies from element 1 to *n* are respectively given by

$$\boldsymbol{T}_n = \sum_{i=1}^{n} \boldsymbol{T}_i \,, \tag{2.37}$$

$$\boldsymbol{U}_n = \sum_{i=1}^{n} \boldsymbol{U}_i \,. \tag{2.38}$$

The equation of motion of the whole system is given by adapting Eqs. (2.37) and (2.38) and considering the boundary conditions as follows

$$\boldsymbol{M}_n \ddot{\boldsymbol{\delta}}_n + C_n \dot{\boldsymbol{\delta}}_n + \left[\boldsymbol{K}_n - \dot{\theta}^2 \boldsymbol{M}_n\right]\boldsymbol{\delta}_n = \ddot{\theta}\, \boldsymbol{f}_n \,. \tag{2.39}$$

2.3 Computational Models

In this chapter, we defined and used three types of computational models of the flexible single-link manipulator.

2.3.1 Model C1.1

A model of a flexible single-link with a clamp-part was used as Model C1.1. Figure 2.4 shows Model C1.1. The link and the clamp-part were discretized by 5 elements and 1 element respectively. The clamp-part is much rigid than the link. Therefore Young's modulus of the clamp-part was set in 1,000 times of the link's. A strain gage is bonded to the position of Node 3 of the flexible link (0.11 m from the origin of the link).

2.3.2 Model C1.2

A model of the single - link manipulator, the clamp-part and the piezoelectric actuator was defined as Model C1.2. Figure 2.5 shows Model C1.2. The link including the clamp-part and actuator were discretized by 35 elements. The clamp-part is more rigid than the link. Therefore Young's modulus of the clamp-part was set in 1,000 times

of the link's. The piezoelectric actuator was bonded to a one-side surface of Element 4. A schematic representation on modeling of the piezoelectric actuator is shown in Fig. 2.7. Furthermore, a strain gage was bonded to the position of Node 6 of the single-link (0.11 m from the origin). Physical parameters of the single-link model and the piezoelectric actuator are shown in Table 2.1.

The piezoelectric actuator suppressed the vibration of the flexible link manipulator by adding bending moments at Nodes 3 and 6, M_3 and M_6 to the flexible link. The bending moments are generated by applying voltages $+E$ to the piezoelectric actuator as shown in Fig. 2.7. The relation between the bending moments and the voltages are related by

$$M_3 = -M_6 = d_1 E \,. \tag{2.40}$$

Here d_1 is a constant quantity.

Furthermore, the voltage to generate the bending moments is proportional to the strain ε of the single-link due to the vibration. The relation can be expressed as follows

$$E = \pm \frac{1}{d_2} \varepsilon \,. \tag{2.41}$$

Here d_2 is a constant quantity. Then, d_1 and d_2 will be determined by comparing the calculated results and experimental ones.

2.3.3 Model C1.3

Figure 2.6 shows Model C1.3 that an end-effector of the single-link manipulator is considered. Model C1.3 is used to show that the proposed control strategies are also suitable for such system. The end-effector is presented by adding a concentrated mass to

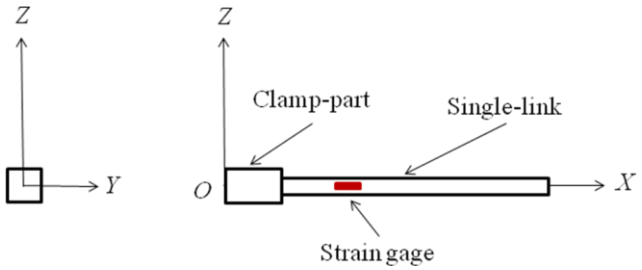

Fig.2.4 Model C1.1: Only flexible single-link

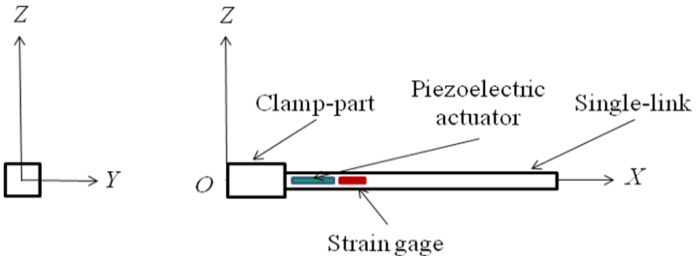

Fig.2.5 Model C1.2: Flexible single-link with piezoelectric actuator

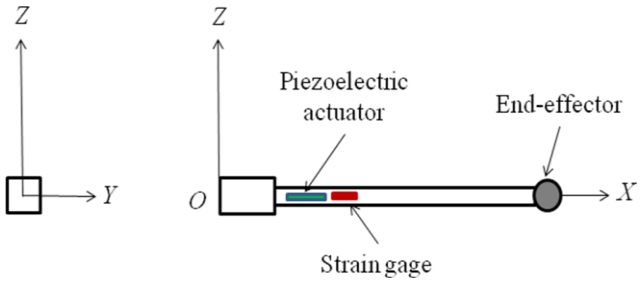

Fig.2.6 Model C1.3: Flexible single-link with piezoelectric actuator and end-effector

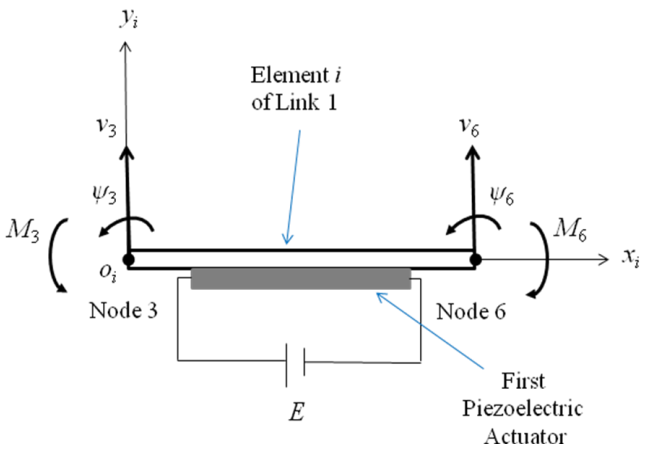

Fig.2.7 Modeling of piezoelectric actuator (top view)

Table 2.1 Physical parameters of the single-link and the piezoelectric actuator

l : Total length	m	3.91×10^{-1}
l_l : Length of the link	m	3.50×10^{-1}
l_c : Length of the clamp-part	m	4.10×10^{-2}
l_a : Length of the actuator	m	2.00×10^{-2}
S_l : Cross section area of the link	m^2	1.95×10^{-5}
S_c : Cross section area of the clamp-part	m^2	8.09×10^{-4}
S_a : Cross section area of the actuator	m^2	1.58×10^{-5}
I_{zl} : Cross section area moment of inertia around z-axis of the link	m^4	2.75×10^{-12}
I_{zc} : Cross section area moment of inertia around z-axis of the clamp-part	m^4	3.06×10^{-8}
I_{za} : Cross section area moment of inertia around z-axis of the actuator	m^4	1.61×10^{-11}
E_l : Young's Modulus of the link	GPa	7.03×10^{1}
E_c : Young's Modulus of the clamp-part	GPa	7.00×10^{4}
E_a : Young's Modulus of the actuator [70]	GPa	4.40×10^{1}
ρ_l : Density of the link	kg/m^3	2.68×10^{3}
ρ_c : Density of the clamp-part	kg/m^3	9.50×10^{2}
ρ_a : Density of the actuator [70]	kg/m^3	3.33×10^{3}
α : Damping factor of the link	s	2.50×10^{-4}

Model C.1.2. Therefore, the kinetic energy of the tip element was increased due to the concentrated mass.

Applying the kinetic energy and the strain energy to Lagrange's equation, so the equation of motion of the tip element containing the concentrated mass is given by

$$\left[\boldsymbol{M}_i + \boldsymbol{M}_{i_{cm}}\right]\ddot{\boldsymbol{\delta}}_i + \boldsymbol{C}_i\dot{\boldsymbol{\delta}}_i + \left[\boldsymbol{K}_i - \dot{\theta}^2\left(\boldsymbol{M}_i + \boldsymbol{M}_{i_{cm}}\right)\right]\boldsymbol{\delta}_i = \ddot{\theta}\left\{\boldsymbol{f}_i + \boldsymbol{f}_{i_{cm}}\right\}, \tag{2.42}$$

where the vector of $\boldsymbol{f}_{icm}$ is given by

$$\boldsymbol{f}_{icm} = m_c\left\{0 \quad 0 \quad -\left(l_{1-i} + l_i\right) \quad 0\right\}^T. \tag{2.43}$$

The concentrated mass matrix M_{icm} can be expressed as

$$\boldsymbol{M}_{icm} = \begin{bmatrix} 0 & 0 & 0 & 0 \\ 0 & 0 & 0 & 0 \\ 0 & 0 & m_c & 0 \\ 0 & 0 & 0 & 0 \end{bmatrix}. \tag{2.44}$$

where m_c is the mass of the concentrated mass.

2.4 Control Scheme and Strategies

A control scheme to suppress the vibration of the single-link was designed using the piezoelectric actuator. It was done by adding bending moments generated by the piezoelectric actuator to the single-link. Therefore, the equation of motion of the system become

$$\boldsymbol{M}_n\ddot{\boldsymbol{\delta}}_n + \boldsymbol{C}_n\dot{\boldsymbol{\delta}}_n + \left[\boldsymbol{K}_n - \dot{\theta}^2\boldsymbol{M}_n\right]\boldsymbol{\delta}_n = \ddot{\theta}\,\boldsymbol{f}_n + \boldsymbol{u}_n, \tag{2.45}$$

where the vector u_n containing M_3 and M_6 is the control force generated by the actuator to the single-link.

To drive the actuator, three different control strategies namely P, PD and AF controls have been designed and examined. Their performances were compared through calculations.

2.4.1 Proportional Control

Substituting Eq. (2.41) to Eq. (2.40) gives

$$M_3 = -M_6 = \frac{d_1}{d_2}\varepsilon. \tag{2.46}$$

Based on Eq. (2.46), the bending moments for P-control can be defined in *s*-domain as follows

$$\boldsymbol{U}_n(s) = \boldsymbol{G}_{C1}(s)\big(\varepsilon_d(s) - \varepsilon_6(s)\big), \tag{2.47}$$

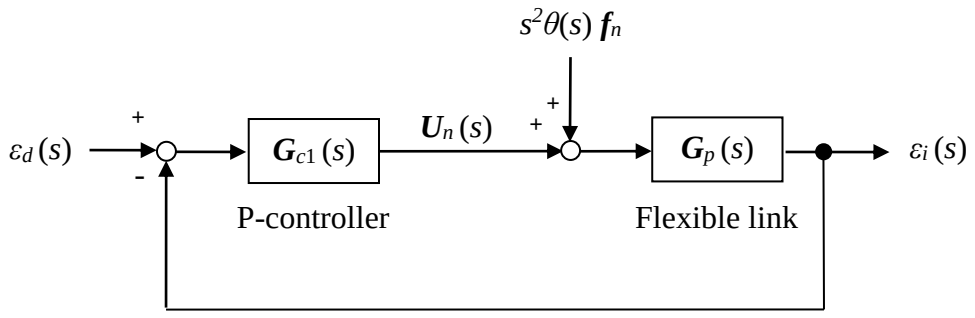

ε_d : Desired strain — ε_i : Measured strains at Node i
θ : Rotation angle of the motor — $\boldsymbol{U}_n$: Applied bending moments

Fig. 2.8 Block diagram of proportional control of the flexible single-link manipulator

where ε_d and ε_6 denote the desired and measured strains at Node 6, respectively.

The gain of P- controller can be written by a vector in *s*-domain respectively as follows

$$\boldsymbol{G}_{C1}(s) = \{0 \quad 0 \quad 0 \quad 0 \quad 0 \quad K_p \quad 0 \quad 0 \quad 0 \quad 0 \quad 0 \quad -K_p \quad \ldots \quad 0\}^T, \tag{2.48}$$

where K_p is proportional gain of the P-controller.

A block diagram of the P-control strategy for the single-link system is shown in Fig. 2.8.

2.4.2 Proportional-Derivative Control

Based on Eq. (2.46), the bending moments for PD-control can be defined in *s*-domain as follows

$$\boldsymbol{U}_n(s) = \boldsymbol{G}_{C2}(s)\left(\varepsilon_d(s) - \varepsilon_6(s)\right), \tag{2.49}$$

where ε_d and ε_6 denote the desired and measured strains at Node 6, respectively.

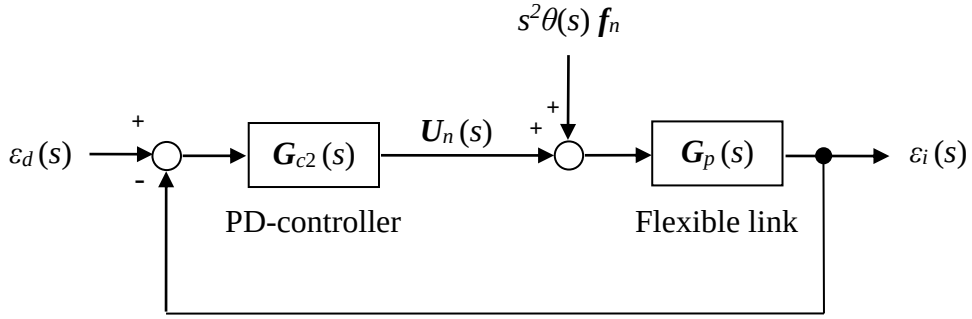

ε_d : Desired strain — ε_i : Measured strains at Node i

θ : Rotation angle of the motor — $\boldsymbol{U}_n$: Applied bending moments

Fig. 2.9 Block diagram of proportional-derivative control of the flexible single-link manipulator

The gain of PD-controller can be written by a vector in *s*-domain respectively as follows

$$\boldsymbol{G}_{C2}(s) = \{0 \quad 0 \quad 0 \quad 0 \quad 0 \quad (K_p + K_d) \quad 0 \quad 0 \quad 0 \quad 0 \quad 0 \quad -(K_p + K_d) \quad \ldots \quad 0\}^T, \quad (2.50)$$

where K_p and K_d are proportional and derivative gains of the PD-controller.

A block diagram of the PD-control strategy for the single-link system is shown in Fig. 2.9.

2.4.3 Active-force Control

Figure 2.10 shows a block diagram of the AF control that is proposed in this study. In this strategy, vibration of the system is controlled by canceling bending moments acting at Nodes 3 and 6 due to the base excitation (excitation bending moments). The following steps are the way to estimate and cancel the excitation bending moments.

Firstly, the strain, ε_6 at Node 6 is measured to estimate the lateral deformation, v_6 at Node 6. Substituting Eq. (4.6) to Eq. (4.16) considering the boundary conditions then the relation between the strain and the lateral deformation can be defined as follows

$$\frac{v_6}{\varepsilon_6} = -\frac{x^2(x-3l)}{6y(x-l)} = A, \tag{2.51}$$

where l, x and y are the length of the link, the position of Node 6 in x and y directions, respectively.

Secondly, the actual force in the s-domain acting at Node 6 can be defined in the form of the Newton's equation of motion as follows

$$F_6(s) = M_{ii(i=11)}\, s^2\, v_6, \tag{2.52}$$

where $M_{ii(i=11)}$ is the component of the mass matrix corresponding to v_6.

Thirdly, the bending moments acting at Nodes 3 and 6 are estimated using the following equation

$$\boldsymbol{U}_{nt}(s) = \pm F_6(s)\boldsymbol{d}\,, \tag{2.53}$$

The vector $\boldsymbol{d}$ that represents the position vector from the reference point to the position where the excitation force acting can be written as follows

$$\boldsymbol{d} = \{0 \quad 0 \quad 0 \quad 0 \quad 0 \quad l_2 \quad 0 \quad 0 \quad 0 \quad 0 \quad 0 \quad l_2 \quad \ldots \quad 0\}^T, \tag{2.54}$$

where l_2 is distance from the reference point to the position where the excitation force acting.

Fourthly, based on Fig. 2.10, the excitation bending moments can be calculated as

$$\boldsymbol{U}_{ne}(s) = K_{pa}\left\{\boldsymbol{U}_{nt}(s) - \boldsymbol{U}_n(s)\right\}, \tag{2.55}$$

where K_{pa} is the non-dimensional proportional gain of the proposed AF control.

Finally, the bending moments applying as a control force to control the vibration of the system can be calculated as follows

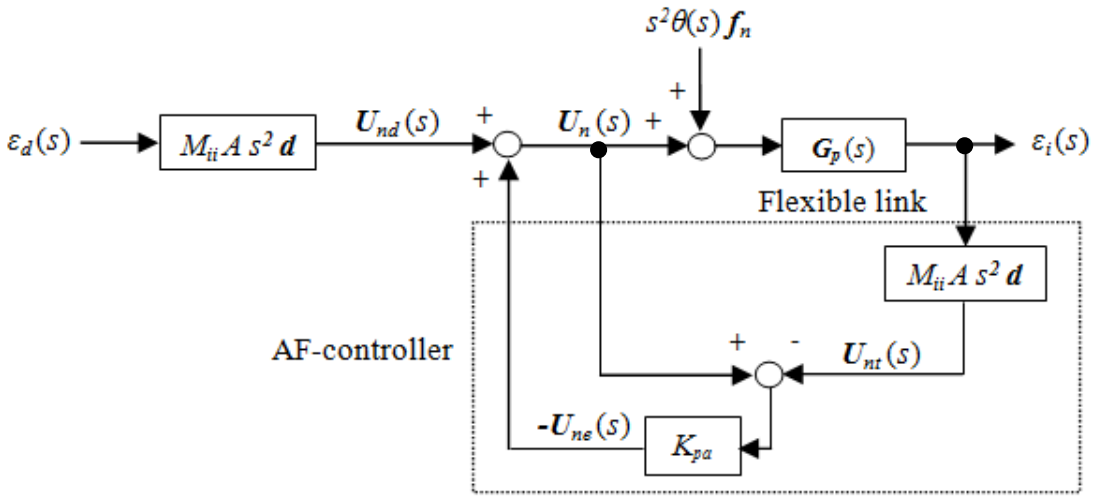

ε_d : Desired strain
θ : Rotation angle of the motor
A : Conversion from ε_i to v_i
$\boldsymbol{U}_{nd}$: Desired bending moments
$\boldsymbol{U}_{ne}$: Excitation bending moments
ε_i : Measured strains at Node i
M_{ii} : Component of mass matrix
$\boldsymbol{d}$: Position vector
$\boldsymbol{U}_n$: Applied bending moments
$\boldsymbol{U}_{nt}$: Bending moments

Fig. 2.10 Block diagram of active-force control of the flexible single-link manipulator

$$\boldsymbol{U}_n(s) = -\boldsymbol{U}_{ne}(s) + \boldsymbol{U}_{nd}(s), \tag{2.56}$$

where $\boldsymbol{U}_{nd}(s)$ is the desired bending moments which is zero. The negative of $\boldsymbol{U}_{ne}(s)$ indicates that the bending moments were used to cancel the vibration of the system.

2.5 Calculated Results

2.5.1 Time History Response on Free Vibration

Model C1.1 was used to calculate time history response of strains for the flexible single-link manipulator using an impulse force as an external one. Computational codes on time history response of strains for Model C1.1 were developed based on formulation explained in Sub-Chapter 2.2. Figure 2.11 shows the calculated time history response of strains at Node 3 of Model C1.1 under the impulse force.

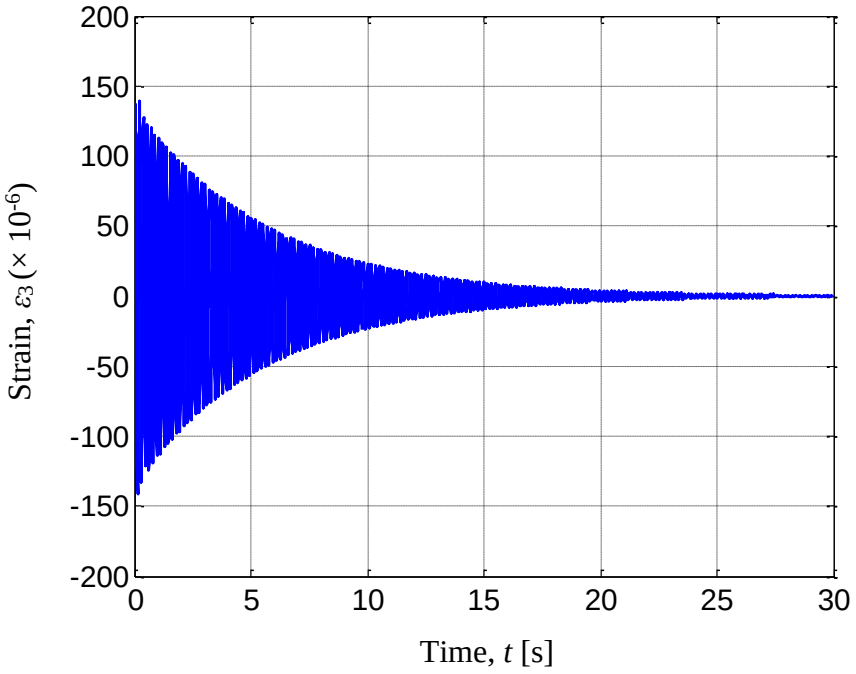

Fig. 2.11 Calculated time history response of strains on free vibration at Node 3 of Model C1.1

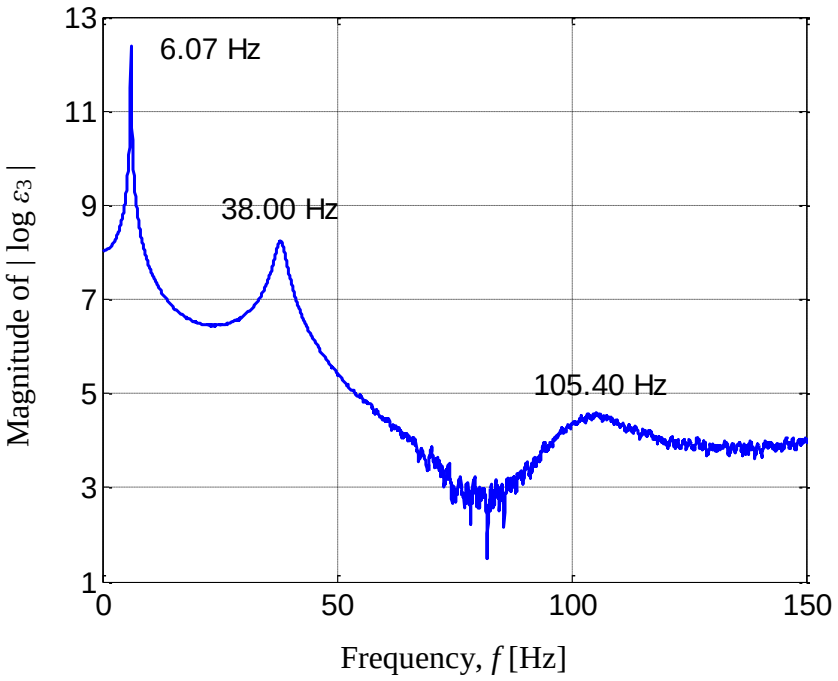

Fig. 2.12 Calculated natural frequencies of Model C1.1

2.5.2 Fast Fourier Transform Processing

The calculated time history response of strains on free vibration of Model C1.1 was transferred by FFT processing to find its frequencies. Figure 2.12 show the calculated natural frequencies of the flexible link manipulator. The first, second and third calculated natural frequencies are 6.07 [Hz], 38.00 [Hz] and 105.40 [Hz], respectively.

2.5.3 Eigenvalues and Eigenvectors Analysis

Eigenvalues - eigenvectors analysis for the flexible single-link manipulator was done using Model C1.1. Computational codes on eigenvalues - eigenvectors analysis were developed to find natural frequencies and vibration modes. The calculated results for the first, second and third natural frequencies were 6.10 [Hz], 38.22 [Hz], and 107.19 [Hz] respectively. Vibration modes of the natural frequencies are shown in Figs. 2.13, 2.14 and 2.15.

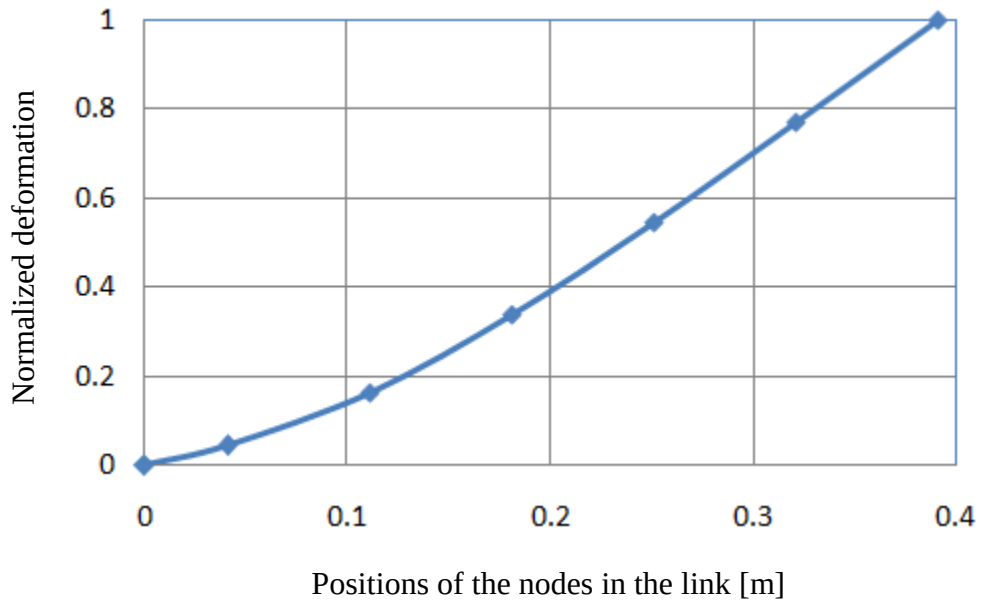

Fig. 2.13 First vibration mode and natural frequency (f_1 = 6.10 Hz) of Model C1.1

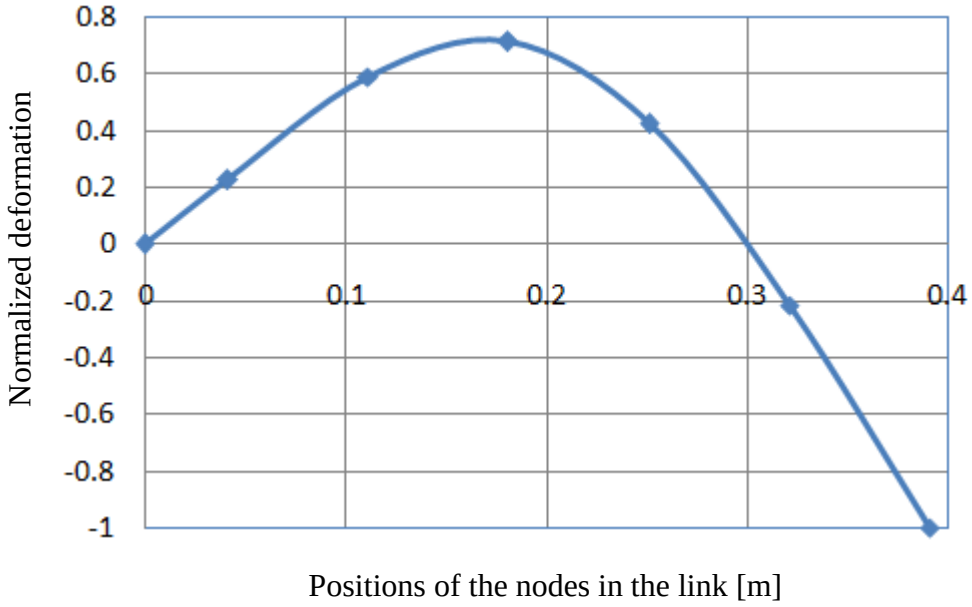

Fig. 2.14 Second vibration mode and natural frequency (f_2 = 38.22 Hz) of Model C1.1

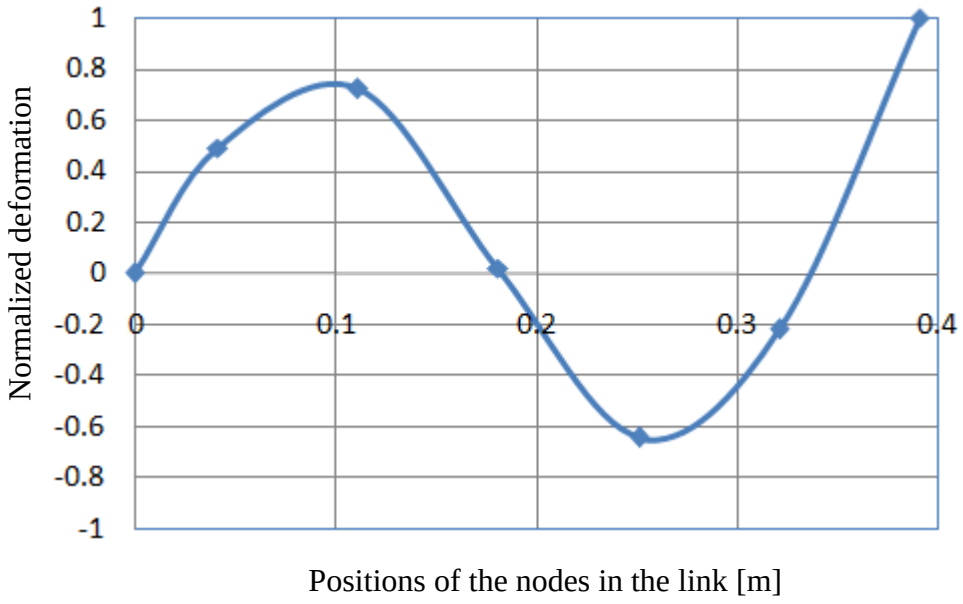

Fig. 2.15 Third vibration mode and natural frequency (f_3 = 107.19 Hz) of Model C1.1

2.5.4 Time History Response due to Base Excitation

Another calculation was done to find time history response of strains for the flexible single-link manipulator due to the base excitation generated by rotation of the

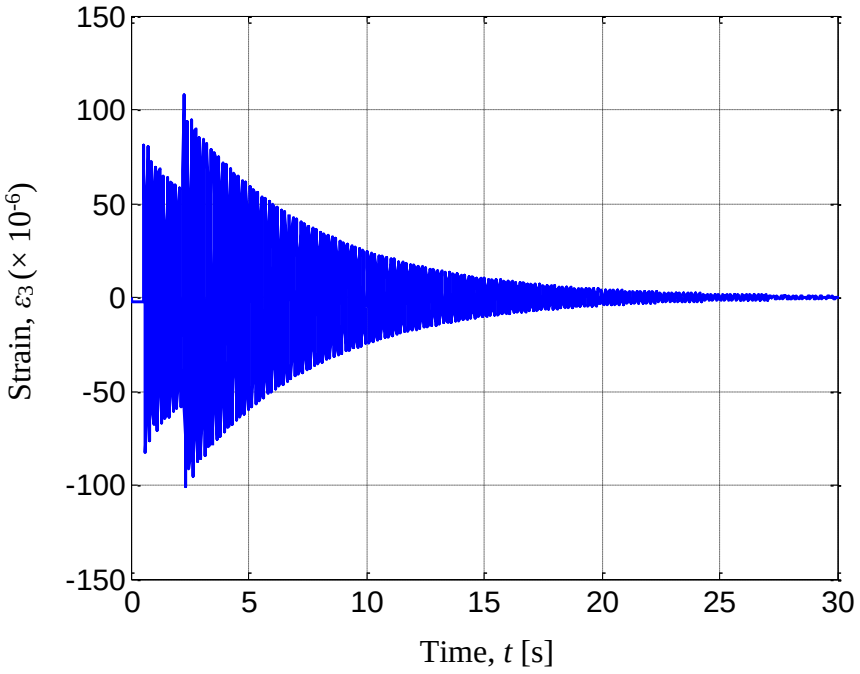

Fig. 2.16 Calculated time history response of strains due to base excitation at Node 3 of Model C1.1

motor. Computational codes on time history response of strains using Model C1.1 were developed based on the formulation explained in Sub-Chapter 2.2. In the calculation, the motor was rotated by the angle of $\pi/2$ radians (90 degrees) within 2.05 seconds. Figure 2.16 shows the calculated time history responses of strains at Node 3 of Model C1.1 under the base excitation.

2.5.5 Time History Responses on Uncontrolled and Controlled System for Model C1.2

Time history responses of strains on the uncontrolled and controlled systems were calculated when the motor rotated by the angle of $\pi/2$ radians (90 degrees) within 0.68 [s]. Time history responses of strains on the controlled system were calculated for Model C1.2 under three control strategies shown in Figs 2.8, 2.9 and 2.10.

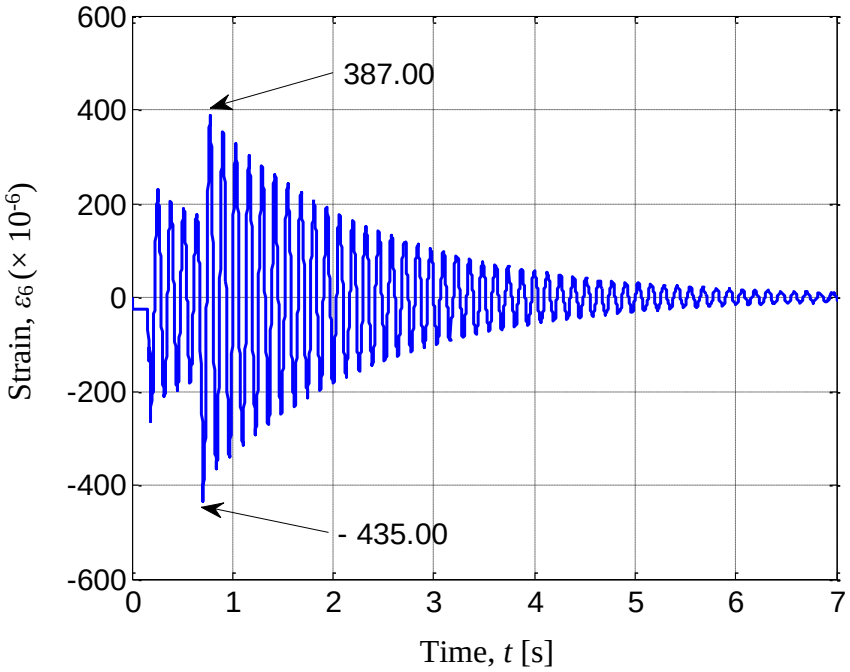

Fig. 2.17 Calculated time history response of strains at Node 6 for uncontrolled Model C1.2 due to base excitation

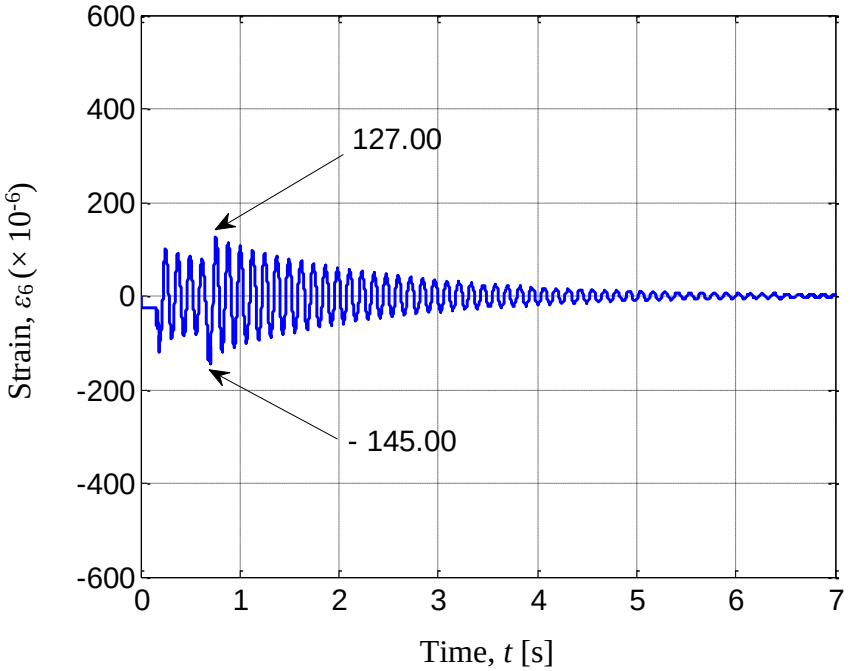

Fig. 2.18 Calculated time history response of strains at Node 6 for controlled Model C1.2 due to base excitation using P-controller (K_p = 30 [Nm])

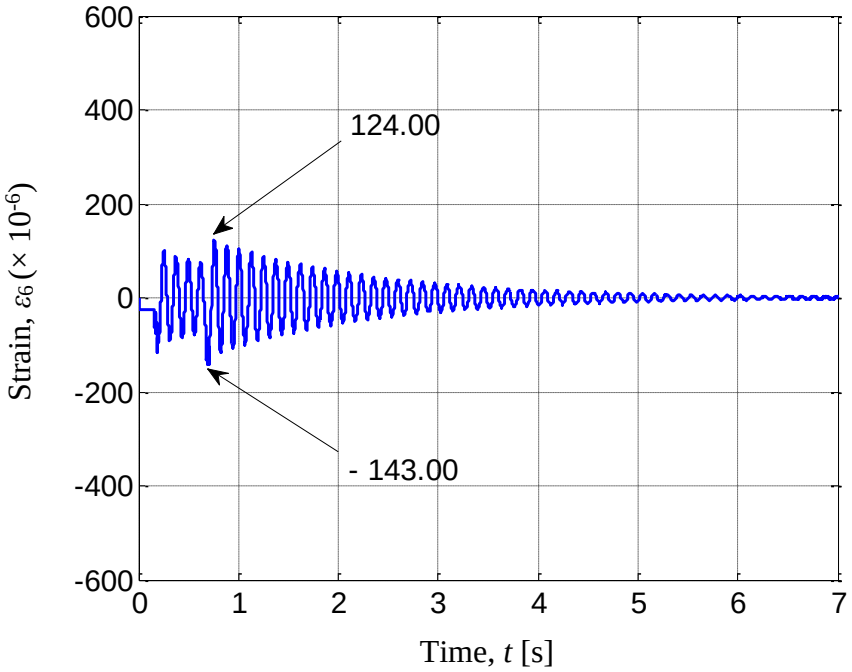

Fig. 2.19 Calculated time history response of strains at Node 6 for controlled Model C1.2 due to base excitation using PD-controller (K_p = 30 [Nm], K_d = 0.02 [Nm])

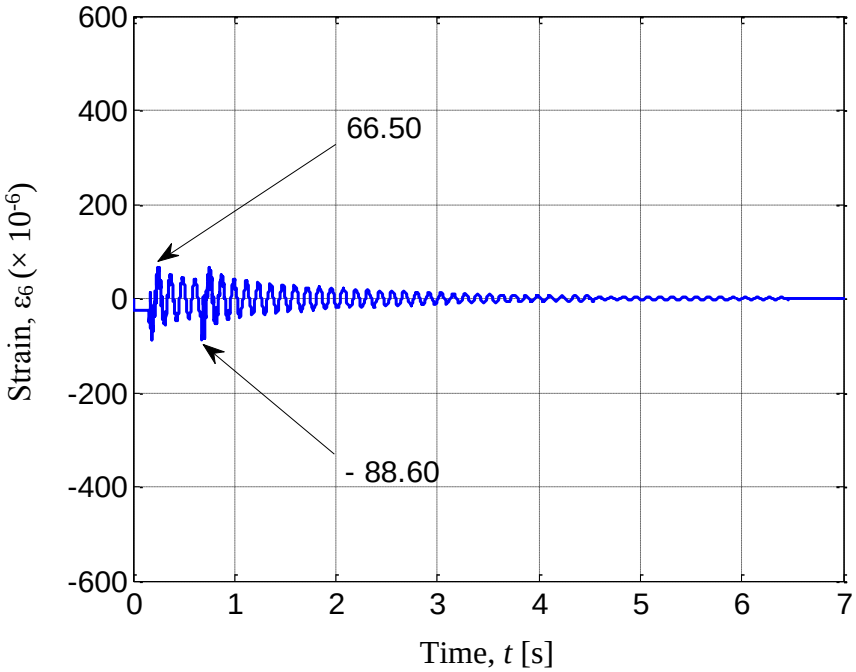

Fig. 2.20 Calculated time history response of strains at Node 6 for controlled Model C1.2 due to base excitation using AF-controller (K_{pa} = 0.4 [-])

Examining several gains of the P, PD and AF controllers leaded to K_p = 30 [Nm], K_d = 0.02 [Nms] and K_{pa} = 0.4 [-] as the better ones. Figures 2.17 to 2.20 show the calculated time history responses of strains at Node 6 for uncontrolled and controlled Model C1.2. The maximum and minimum strains of uncontrolled system in positive and negative sides were 387.00×10^{-6} and -435.00×10^{-6}, as shown in Fig. 2.17. By using P-controller they became 127.00×10^{-6} and $-145.00\times10^{-}$, as shown in Fig. 2.18. By adding D-gain they became -124.00×10^{-6} and -143.00×10^{-6}, as shown in Fig. 2.19. Moreover, by using AF-controller they became 66.50×10^{-6} and -88.60×10^{-6}, as shown in Fig. 2.20.

Figures 2.21, 2.22 and 2.23 show control force namely bending moment at Node 6 for Model C1.2 generated by the piezoelectric actuator using P, PD and AF controllers, respectively.

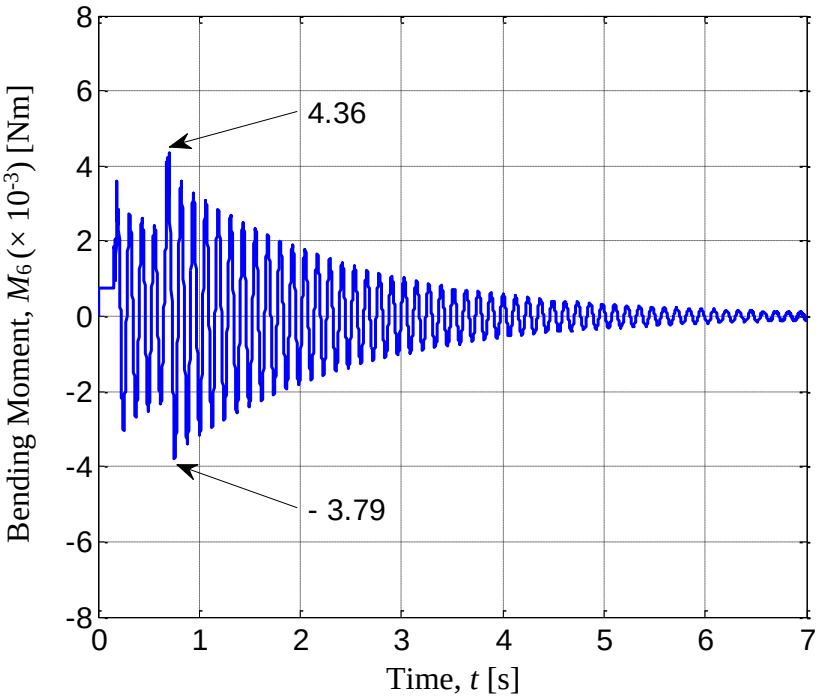

Fig. 2.21 Calculated time history response of bending moment at Node 6 for Model C1.2 generated by the piezoelectric actuator using P-controller (K_p = 30 [Nm])

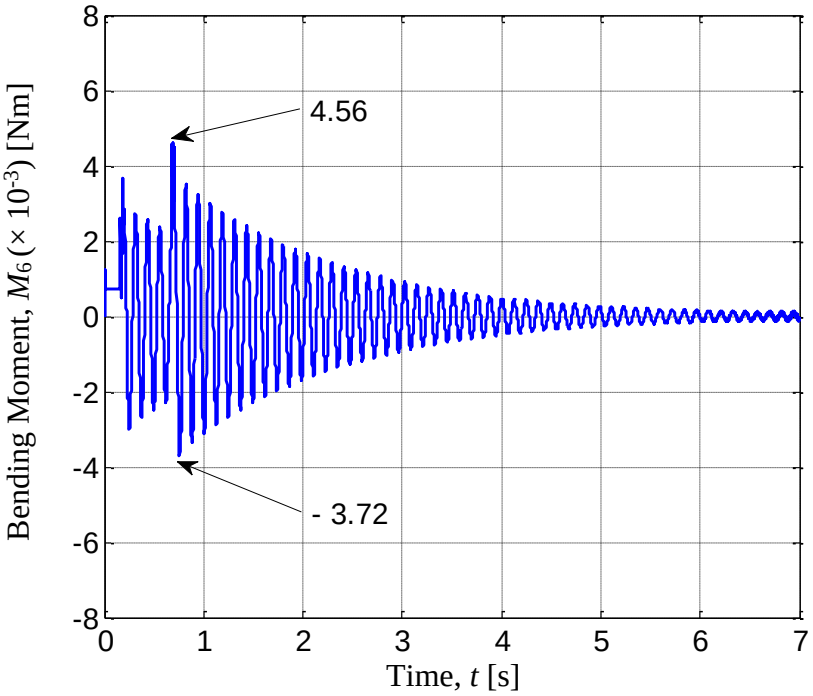

Fig. 2.22 Calculated time history response of bending moment at Node 6 for Model C1.2 generated by the piezoelectric actuator using PD-controller (K_p = 30 [Nm], K_d = 0.02 [Nm])

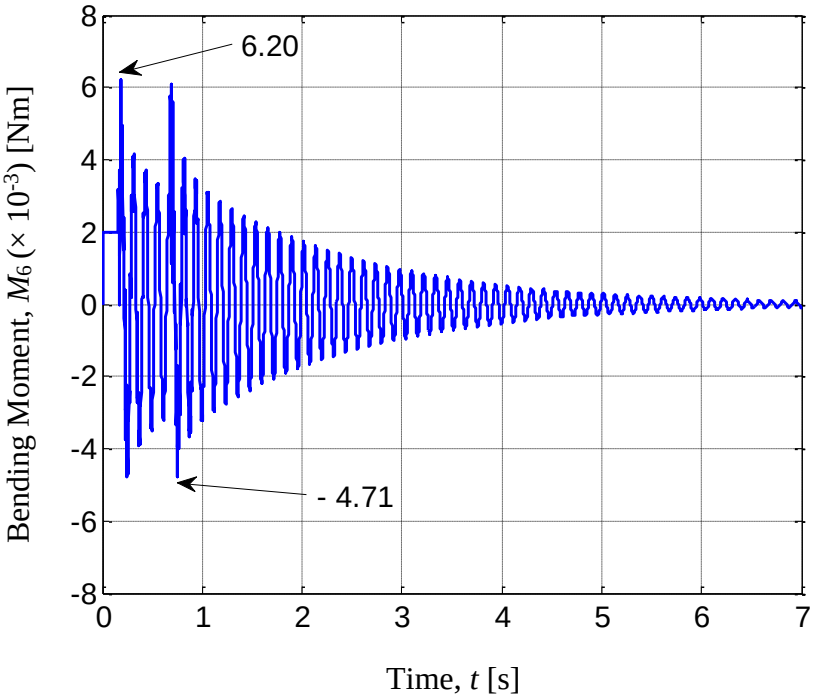

Fig. 2.23 Calculated time history response of bending moment at Node 6 for Model C1.2 generated by the piezoelectric actuator using AF-controller (K_{pa} = 0.4 [-])

2.5.6 Time History Responses on Uncontrolled and Controlled System for Model C1.3

Time history responses of strains on the uncontrolled and controlled systems were calculated when the motor rotated by the angle of $\pi/2$ radians (90 degrees) within 0.68 [s]. Time history responses of strains on the controlled system were calculated for Model C1.3 under three control strategies shown in Figs 2.8, 2.9 and 2.10.

Examining several gains of the P, PD and AF controllers leaded to K_p = 30 [Nm], K_d = 0.02 [Nms] and K_{pa} = 0.4 [-] as the better ones. Figures 2.24 to 2.27 show the calculated time history responses of strains at Node 6 for uncontrolled and controlled Model C1.3. The maximum and minimum strains of uncontrolled system in positive and negative sides were 454.00×10^{-6} and -467.00×10^{-6}, as shown in Fig. 2.24. By using P-controller they became 290.00×10^{-6} and $-296.00\times10^{-}$, as shown in Fig. 2.25.

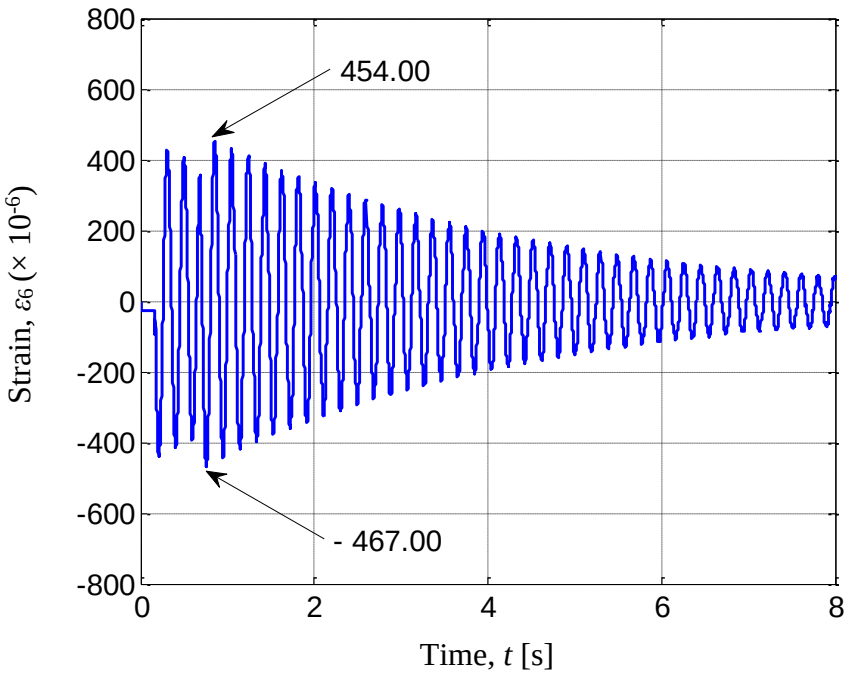

Fig. 2.24 Calculated time history response of strains at Node 6 for uncontrolled Model C1.3 due to base excitation

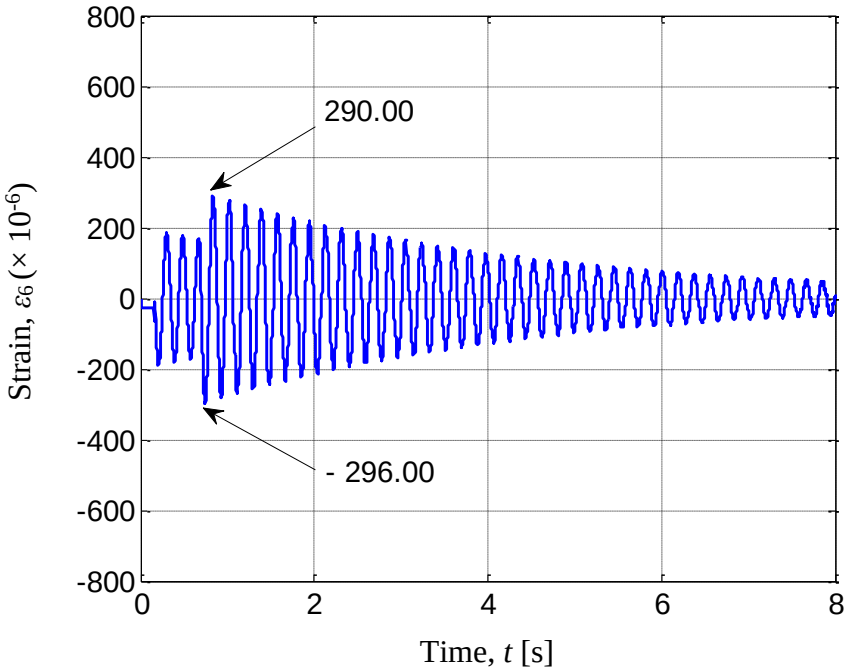

Fig. 2.25 Calculated time history response of strains at Node 6 for Controlled Model C1.3 due to base excitation using P-controller (K_p = 30 [Nm])

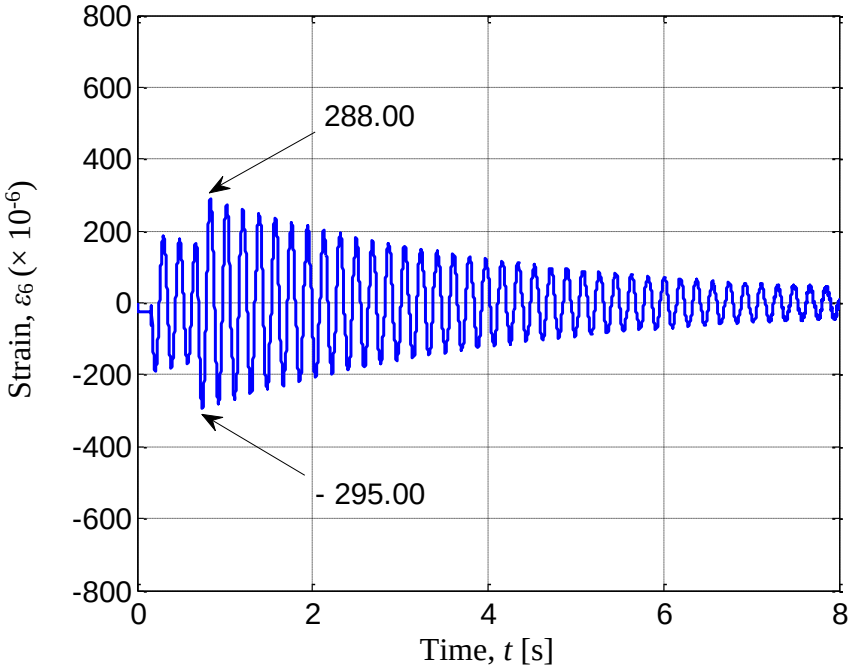

Fig. 2.26 Calculated time history response of strains at Node 6 for Controlled Model C1.3 due to base excitation using PD-controller (K_p = 30 [Nm], K_d = 0.02 [Nm])

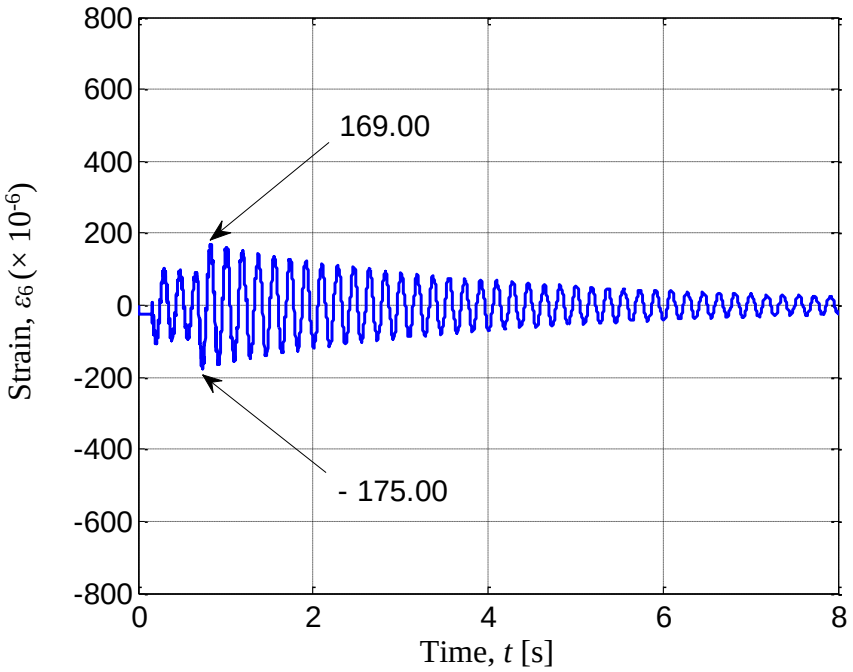

Fig. 2.27 Calculated time history response of strains at Node 6 for Controlled Model C1.3 due to base excitation using AF-controller (K_{pa} = 0.4 [-])

By adding D-gain they became -288.00×10^{-6} and -295.00×10^{-6}, as shown in Fig. 2.26. Moreover, by using AF-controller they became 169.00×10^{-6} and -175.00×10^{-6}, as shown in Fig. 2.27.

2.6 Conclusions

The equations of motion for the flexible single-link manipulator had been derived using the finite element method. Computational codes had been developed in order to perform dynamic simulations of the system. Calculated results on time history responses, natural frequencies and vibration modes have been presented. The proportional (P), proportional-derivative (PD) and active-force (AF) controls strategies were designed to suppress the vibration of the system. Their performances were compared through the calculations. Based on the calculated results, the effect of D-controller was very small

compare to P-controller, therefore using a P-controller will be sufficient for experiment. The calculated results show the superiority of the proposed AF control compared to the P and PD ones to suppress the vibration of the flexible single-link manipulator.

Chapter 3

Experiments on Vibration Control of a Flexible Single-link Manipulator Using a Piezoelectric Actuator

3.1 Introduction

The purposes of study presented in this chapter are to validate the formulation, the computational codes and modeling of the single-link system presented in Chapter 2 through experiments and to validate the proposed control scheme and strategies of the flexible single-link manipulator.

The flexible manipulator used in this study consists of an aluminum beam as a flexible link, a clamp-part, a servo motor to rotate the link, a piezoelectric actuator to control vibration and a base. Experiments on time history responses and FFT (Fast Fourier Transform) processing were carried out to present the dynamic behavior of the link. Furthermore, the P and AF controls strategies were implemented to suppress the vibration of the system. They were carried out using the piezoelectric actuator. Finally, their performances were compared through the experiments.

3.2 Experimental Models

In this chapter, we developed and used two types of experimental models of the flexible single-link manipulator.

3.2.1 Model E1.1

A model of the flexible single-link with the clamp-part and the servo motor was used as Model E1.1. Figure 3.1 shows Model E1.1. The link is attached to the motor through the clamp-part. A strain gage is bonded to the position of 0.11 [m] from the origin of the link. The motor is mounted to the base. Model E1.1 was used to validate the dynamic behavior of the link. In the experiments, the motor was operated by an independent motion controller.

3.2.2 Model E1.2

A model of the single-link manipulator, the clamp-part, the servo motor and the piezoelectric actuator was defined as Model E1.2. Figure 3.2 shows Model E1.2. The piezoelectric actuator was bonded to a one-side surface of the link. Figure 3.3 shows the piezoelectric actuator with its clamped mechanism. A strain gage is bonded to the position of 0.11 [m] from the origin of the link. The motor is mounted to the base. Model E1.2 was used to implement the control scheme and strategies designed in the previous chapter. In the experiments, the motor was operated by an independent motion controller. Physical parameters of the single-link models and the piezoelectric actuator are shown in Table 2.1.

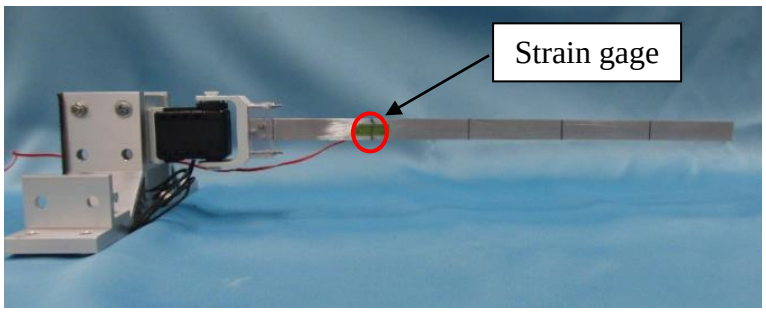

Fig.3.1 Model E1.1: Only flexible single-link

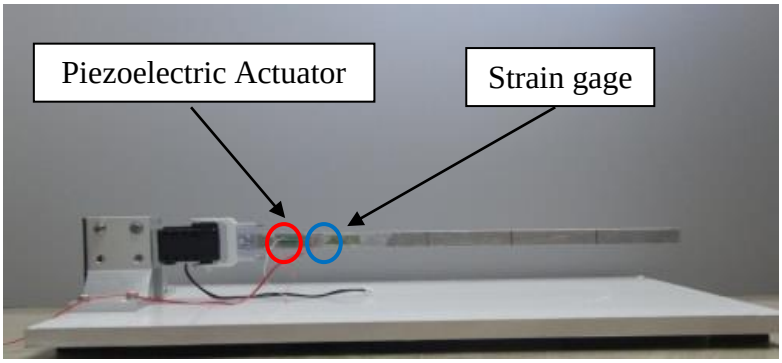

Fig.3.2 Model E1.2: Flexible single-link with piezoelectric actuator

(a) Front view (b) Top view

Fig.3.3 Piezoelectric actuator with clamped mechanism

Table 2.1 Physical parameters of the single-link and the piezoelectric actuator
(previously shown in Page 18)

l : Total length	m	3.91×10^{-1}
l_l : Length of the link	m	3.50×10^{-1}
l_c : Length of the clamp-part	m	4.10×10^{-2}
l_a : Length of the actuator	m	2.00×10^{-2}
S_l : Cross section area of the link	m^2	1.95×10^{-5}
S_c : Cross section area of the clamp-part	m^2	8.09×10^{-4}
S_a : Cross section area of the actuator	m^2	1.58×10^{-5}
I_{zl} : Cross section area moment of inertia around z-axis of the link	m^4	2.75×10^{-12}
I_{zc} : Cross section area moment of inertia around z-axis of the clamp-part	m^4	3.06×10^{-8}
I_{za} : Cross section area moment of inertia around z-axis of the actuator	m^4	1.61×10^{-11}
E_l : Young's Modulus of the link	GPa	7.03×10^{1}
E_c : Young's Modulus of the clamp-part	GPa	7.00×10^{4}
E_a : Young's Modulus of the actuator	GPa	4.40×10^{1}
ρ_l : Density of the link	kg/m^3	2.68×10^{3}
ρ_c : Density of the clamp-part	kg/m^3	9.50×10^{2}
ρ_a : Density of the actuator	kg/m^3	3.33×10^{3}
α : Damping factor of the link	s	2.50×10^{-4}

3.3 Control Scheme and Strategies

The control scheme used in the experiments was presented in previous chapter. As stated in the conclusions of Chapter 2, based on the calculated results, the effect of D-controller was very small compare to P-controller.

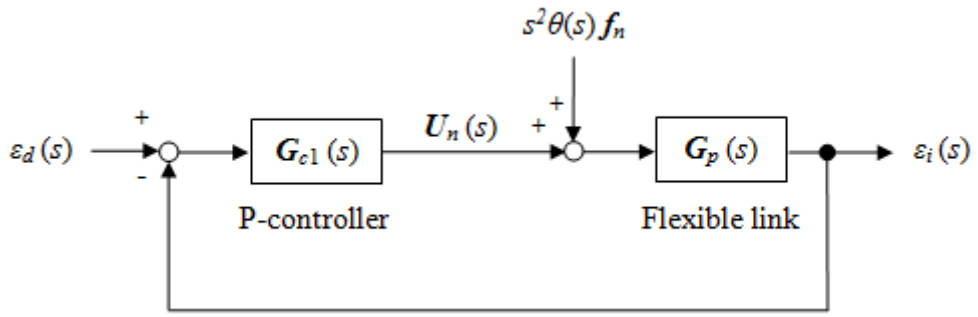

ε_d : Desired strain
θ : Rotation angle of the motor
ε_i : Measured strains at Node i
$\boldsymbol{U}_n$: Applied bending moments

Fig. 2.8 Block diagram of proportional control of the flexible single-link manipulator (previously shown in Page 20)

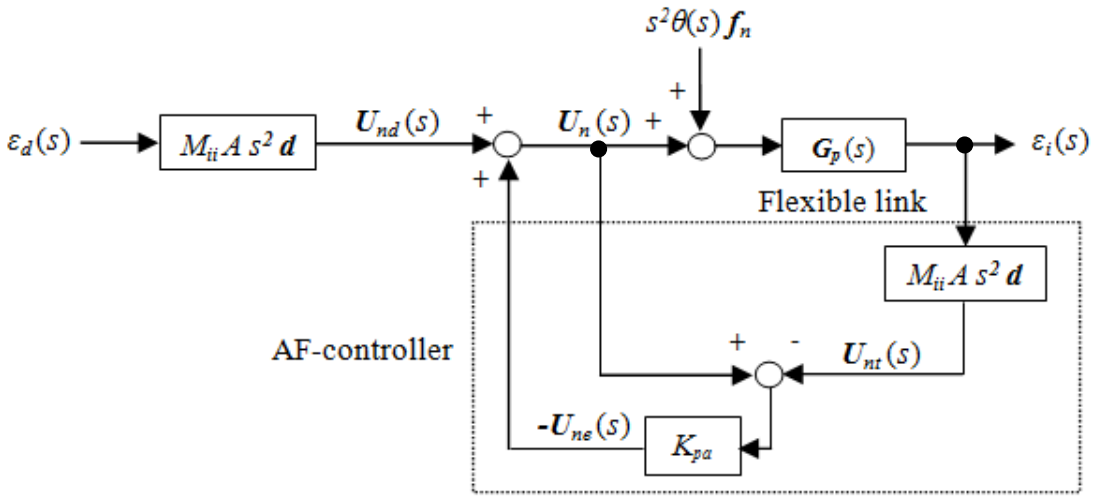

ε_d : Desired strain
θ : Rotation angle of the motor
A : Conversion from ε_i to v_i
$\boldsymbol{U}_{nd}$: Desired bending moments
$\boldsymbol{U}_{ne}$: Excitation bending moments
ε_i : Measured strains at Node i
M_{ii} : Component of mass matrix
$\boldsymbol{d}$: Position vector
$\boldsymbol{U}_n$: Applied bending moments
$\boldsymbol{U}_{nt}$: Bending moments

Fig. 2.10 Block diagram of active-force control of the flexible single-link manipulator (previously shown in Page 23)

Therefore, to drive the actuator, only P and AF control strategies will be implemented. Their performances were compared through the experiments. Figs. 2.8 and 2.10 show the block diagrams of the P and AF control strategies.

3.4 Experimental Set-up

3.4.1 System Configuration

In order to investigate the validity of the proposed control strategies, an experimental set-up was designed. The schematic representation and experimental set-up are shown in Figs. 3.3 and 3.4. The flexible single-link manipulator consists of the flexible aluminum beam, the clamp-part, the servo motor and the base. The flexible link was attached to the motor through the clamp-part. In the experiments, the motor was operated by an independent motion controller. A strain gage was bonded to the position of 0.11 [m] from the origin of the link.

The piezoelectric actuator was attached on one side of the flexible link to provide the blocking force against vibrations. A Wheatstone bridge circuit was developed to measure the changes in resistance of the strain gage in the form of voltages. An amplifier circuit was designed to amplify the small output signal of the Wheatstone bridge.

Furthermore, a data acquisition board and a computer that have functionality of A/D (analog to digital) conversion, signal processing, control process and D/A (digital to analog) conversion were used. The data acquisition board connected to the computer through USB port. Finally, the controlled signals sent to a piezo driver to drive the piezoelectric actuator in its voltage range.

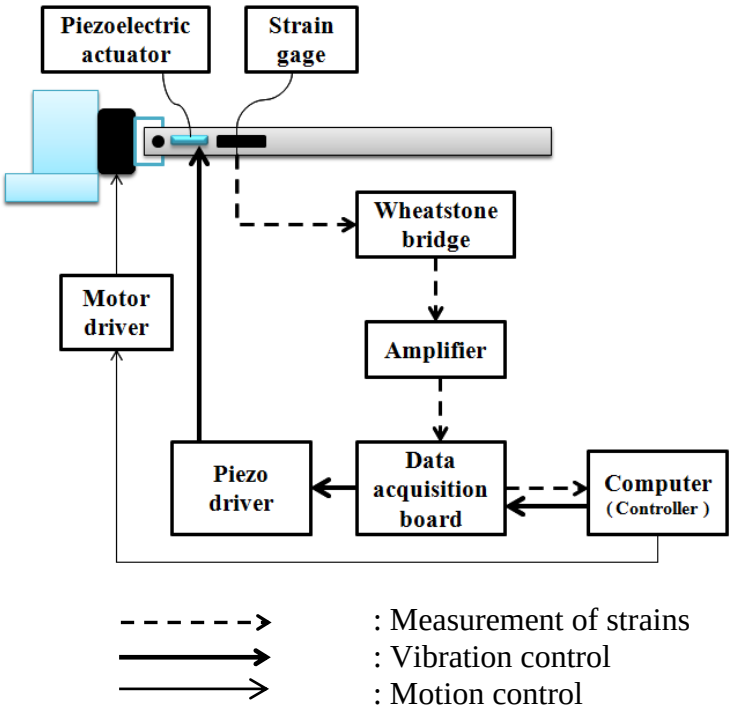

Fig.3.3 Schematics of measurement and control of the flexible single-link manipulator

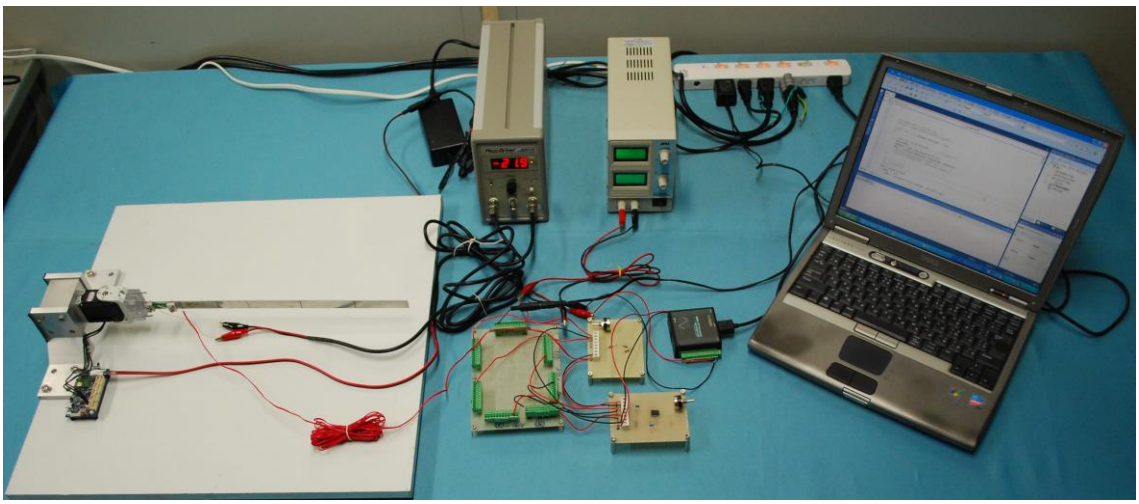

Fig.3.4 Experimental set-up of the flexible single-link manipulator

3.4.2 Wheatstone Bridge

A Wheatstone bridge circuit was designed to convert the change in resistance of the strain gage to voltage signal. The designed bridge has three 120 Ω resistors connected to the strain gage which has a variable resistance of 120 ± 0.8 Ω. Excitation

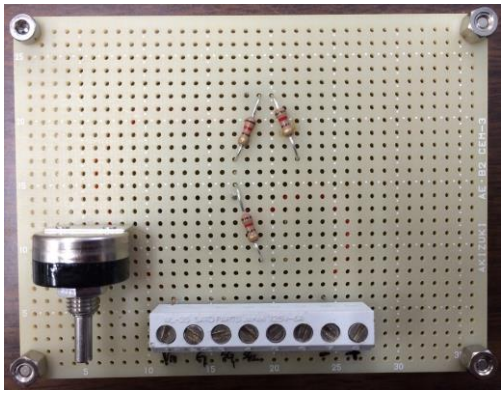

Fig.3.5 Wheatstone bridge

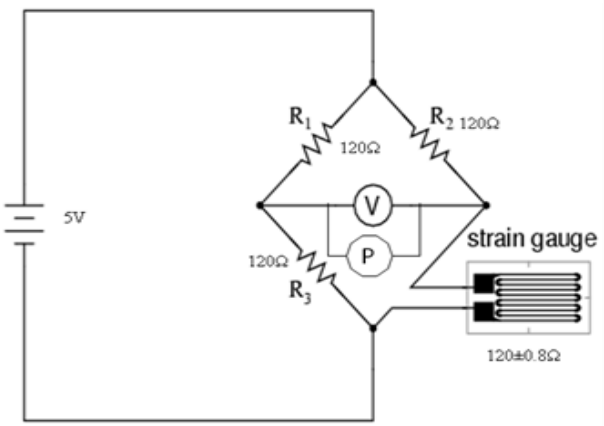

Fig.3.6 Circuit of the Wheatstone bridge

voltage of to drive the bridge, V_{ex} is 5 [V]. Output voltage and variable potentiometer are denoted by *V* and *P*. The Wheatstone bridge and its circuit are shown in Figs. 3.5 and 3.6.

3.4.3 Amplifier

Output signals of the Wheatstone bridge circuit were in milli-Volt [mV] so that it is difficult for data acquisition system to sense the signals. Therefore, a bridge amplifier was designed to amplify the signals. An INA128 amplifier IC was used in this circuit. A

single external resistor was used to set any gain in range of 1 to 10,000. The gain, G can be set using the following equation

$$G = 1 + \frac{50{,}000}{R_G} \tag{3.1}$$

where R_G is the external resistor. A 100 [μF] capacitor attached to the amplifier in order to reduce noises occurred during experiments. The Amplifier and its circuit are shown in Figs. 3.7 and 3.8.

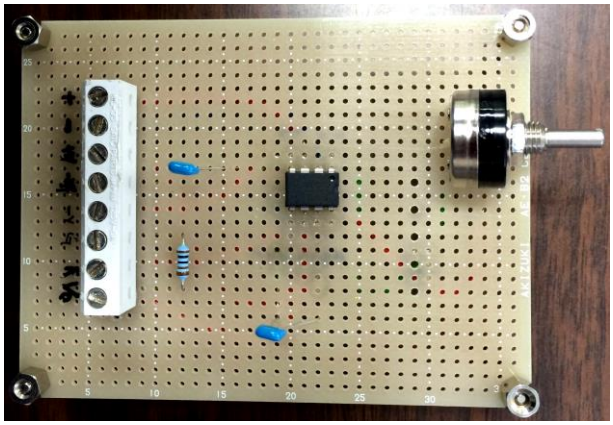

Fig.3.7 Wheatstone bridge

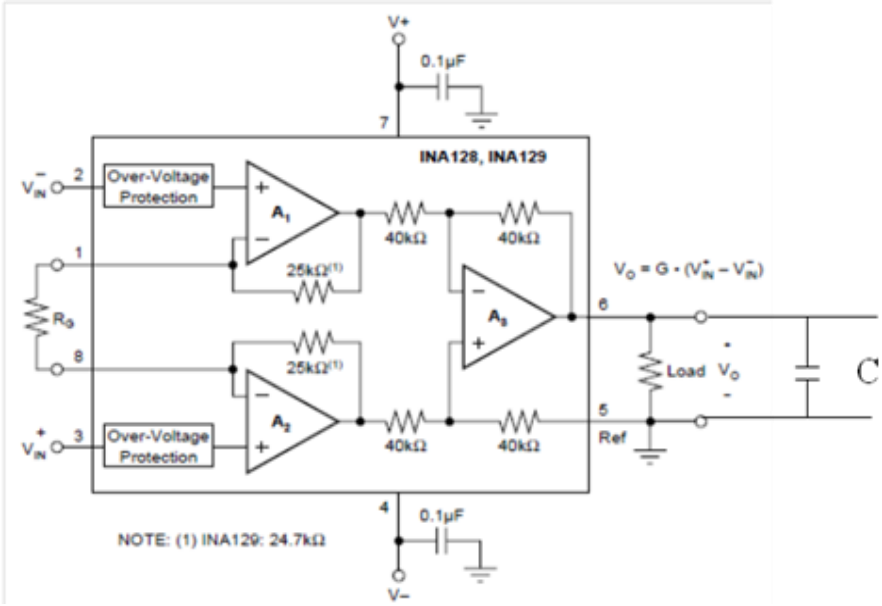

Fig.3.8 Circuit of the amplifier (INA128)

3.4.4 Data Acquisition Board

An AIO-160802AY-USB data acquisition board was used in the experiments. The board has four functions namely analog to digital (A/D) conversion, data acquisition, signal conditioning and digital to analog (D/A) conversion. Input and output ranges of the board are -10 [V] to 10 [V], respectively. The A/D and D/A conversion speeds are 10 [μs/channel], respectively. The board was supported by C++ program. The data acquisition board is shown in Fig. 3.9.

Fig.3.9 AIO-160802AY-USB data acquisition board

3.4.5 Piezo Driver

An M-26116 piezo driver was used to drive the piezoelectric actuator. Input and output ranges of the driver are -10 [V] to 10 [V] and -15 [V] to 150 [V], respectively. The driver gains are 15 [-] and 30 [-]. The piezo driver is shown in Fig. 3.10.

Fig.3.10 M-26116 piezo driver

3.4.6 Power Board

A power board circuit was designed for voltages distribution to the Wheatstone bridge and the amplifier. The power board has two input voltages namely 5 [V] and 12 [V] and three output voltages namely 5 [V], 12 [V] and -12 [V]. A TE 1-1222 DC-DC converter was attach to power board to convert unipolar input voltage of 12 [V] to bipolar output voltage of ±12 [V]. The power board and its circuit are shown in Figs. 3.11 and 3.12.

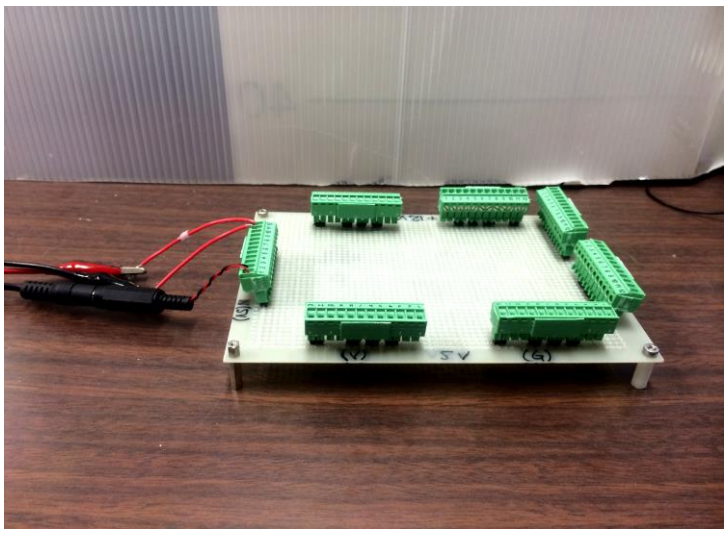

Fig.3.11 Power board

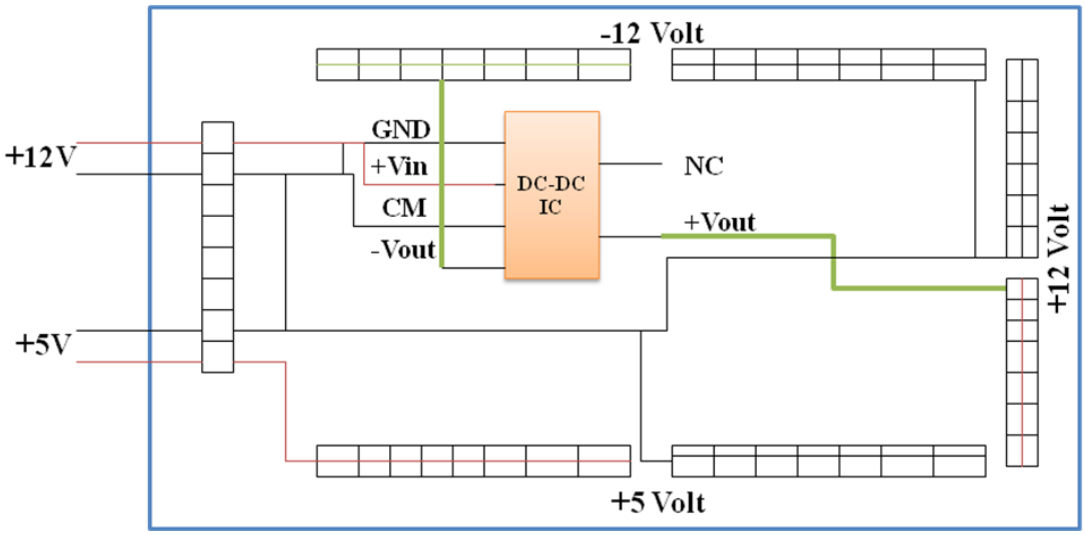

Fig.3.12 Circuit of the power board [69]

3.4.7 PCD-300A

A PCD-300A device was used in data acquisition of strains in the experiments of free vibration. The device input channel was connected to the strain gage while the output channel was connected to a computer to save and display the strains data. The PCD-300A is shown in Fig. 3.13.

Fig.3.13 PCD-300A device [70]

3.5 Experimental Method

The rotation of the motor was set from 0 to $\pi/2$ radians (90 degrees) within 0.68 [s]. The outputs of strain gage were converted to voltages by the Wheatstone bridge and magnified by the amplifier. The noises that occur in the experiment were reduced by a 100 [μF] capacitor attached to the amplifier. The output voltages of the amplifier sent to the data acquisition board and the computer for control process. The control strategies were implemented in the computer using the visual C++ program. The analog output voltages of the data acquisition board sent to the input channel of the piezo-driver to generate the actuated signals for the piezoelectric actuator.

3.6 Experimental Results and Validations of Computational Simulations

3.6.1 Time History Response on Free Vibration

An experiment on free vibration was carried out to measure time history response of strains for the flexible single-link manipulator using an impulse force as an external one. The experiment on free vibration was carried out using Model E1.1 at the same position in the calculation. Figure 3.14 shows the experimental time history response of strains under the impulse force at 0.11 [m] from the origin of the link.

Furthermore, as shown in Chapter 2, Fig. 2.11 shows the calculated time history response of strains at Node 3 of Model C1.1 under the impulse force. The results presented in Figs. 3.14 and 2.11 show the validity of the formulation and computational codes for time history response of strains on free vibration, and the modeling of the single-link system (Model C.11).

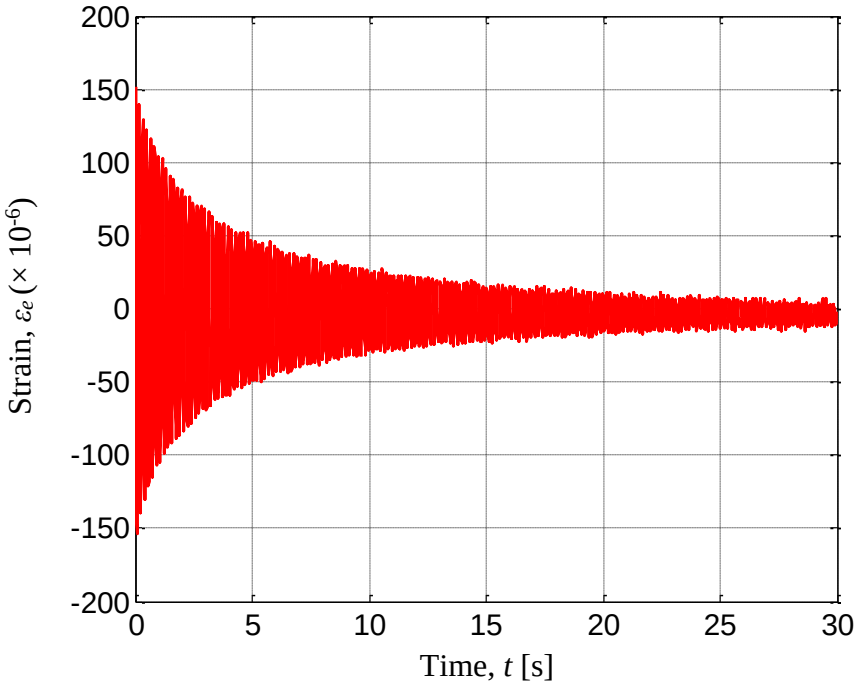

Fig. 3.14 Experimental time history response of strains on free vibration at 0.11 [m] from the origin of the single-link

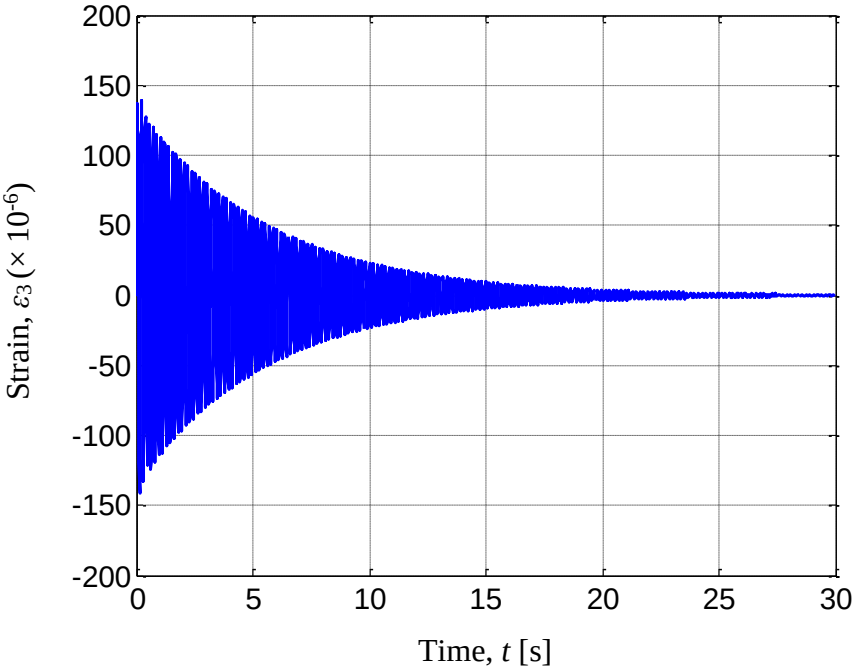

Fig. 2.11 Calculated time history response of strains on free vibration at Node 3 of Model C1.1 (previously shown in Page 24)

3.6.2 Fast Fourier Transform Processing

The experimental time history response of strains on free vibration of the flexible single-link (Model E1.1) was transferred by FFT processing to find its frequencies.

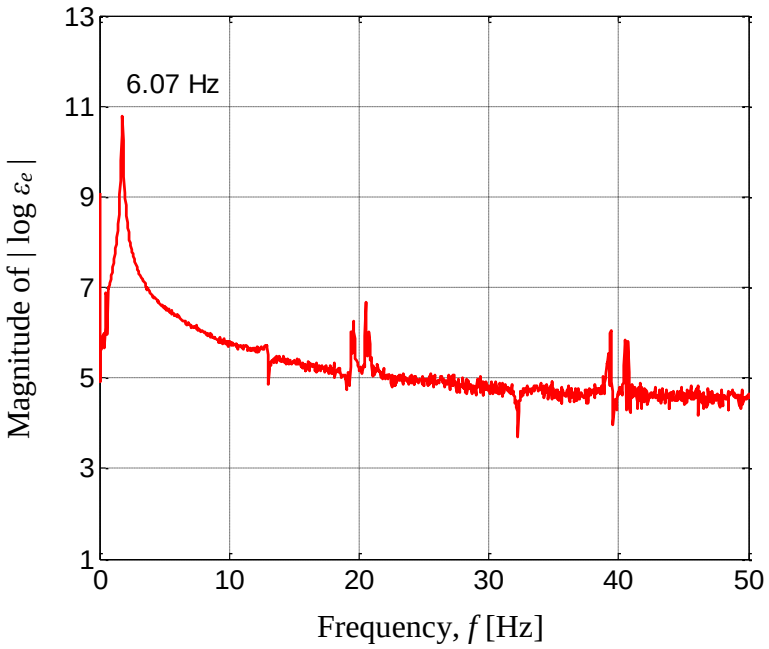

Fig. 3.15 Experimental natural frequency of the flexible single-link

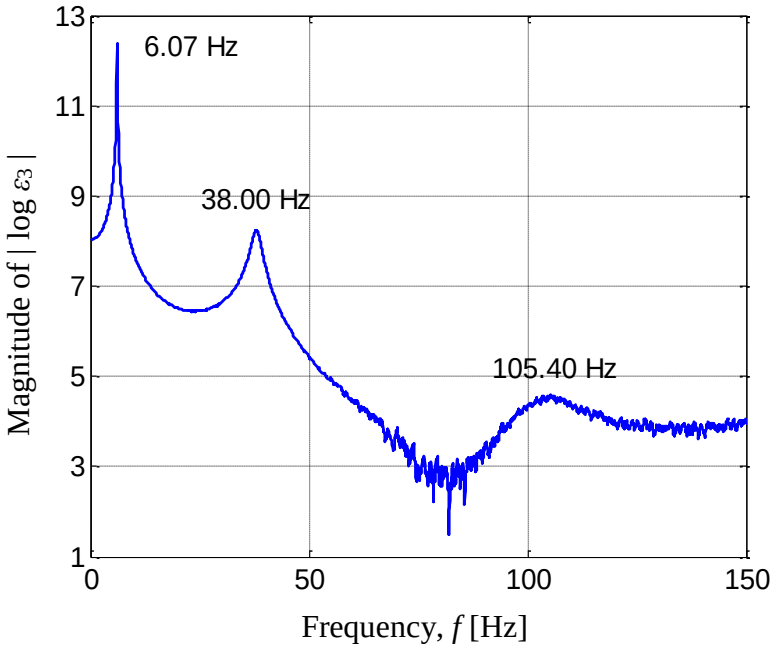

Fig. 2.12 Calculated natural frequencies of Model C1.1 (previously shown in Page 24)

Figure 3.15 shows the experimental time history response of strains on the free vibration at the same position in the calculation (0.11 [m] from the origin of the single-link system). Furthermore, as shown in Chapter 2, Fig. 2.12 shows the calculated natural frequencies. The first experimental natural frequency, 6.07 [Hz] well agreed with the calculated one. The second and third experimental natural frequencies could not be measured. However, in the calculation they could be obtained as 38.00 [Hz] and 105.40 [Hz]. The results presented in Figs. 3.15 and 2.12 show the validity of the formulation and computational codes for natural frequencies, and modeling of the single-link system (Model C.11).

3.6.3 Time History Response due to Base Excitation

Another experiment was carried out to investigate time history response of strains for the flexible single-link manipulator due to the base excitation generated by rotation of the motor. The experiment was carried out using Model E1.1 at the same position in the calculation. In the experiment, the motor was rotated by the angle of $\pi/2$ radians (90 degrees) within 2.05 [s]. Figure 3.16 shows the experimental time history response of strains due to the base excitation at 0.11 [m] from the origin of the link.

Furthermore, as shown in Chapter 2, Fig. 2.16 shows the calculated time history response of strains at Node 3 of Model C1.1 due to the base excitation. The results presented in Figs. 3.16 and 2.16 show the validity of the formulation and computational codes for time history response of strains due to the base excitation, and the modeling of the single-link system (Model C.11).

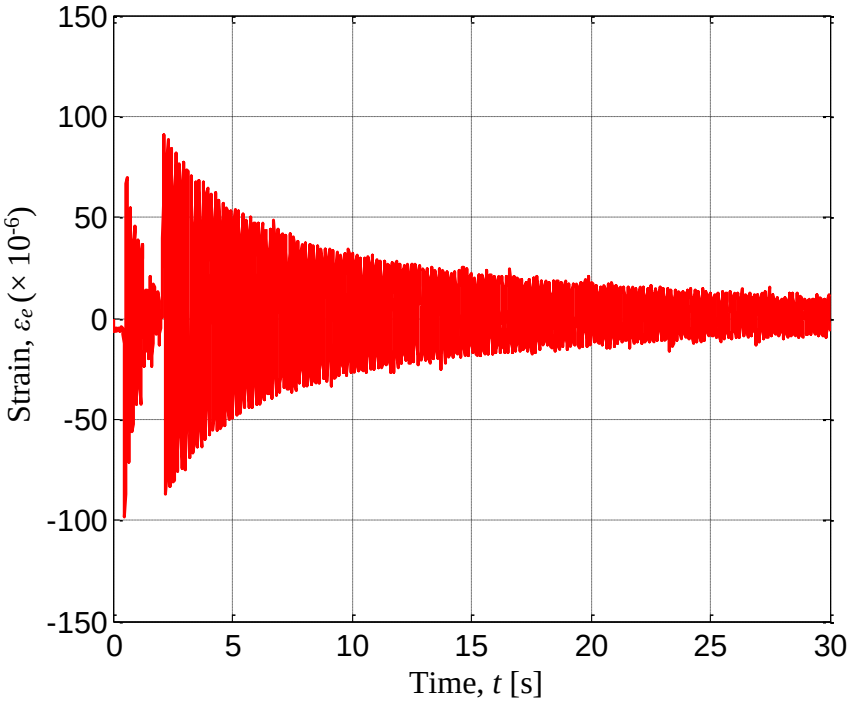

Fig. 3.16 Experimental time history response of strains due to the base excitation at 0.11 [m] from the origin of the link

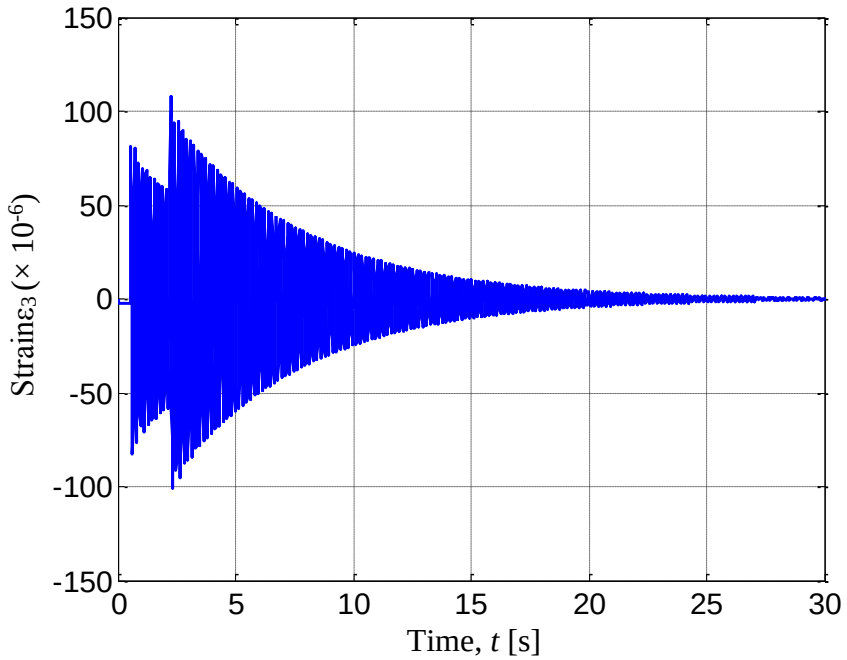

Fig. 2.16 Calculated time history response of strains due to base excitation at Node 3 of Model C1.1 (previously shown in Page 27)

3.6.4 Time History Responses on Uncontrolled and Controlled System

Experimental time history responses of the strains on the uncontrolled and controlled systems were measured using Model E1.2 when the motor rotated by the angle of $\pi/2$ radians (90 degrees) within 0.68 [s]. Experimental time history responses of strains on the controlled system were measured under two control strategies shown in Figs. 2.9 and 2.10.

Furthermore, the experimental proportional and active-force gains that are non-dimensional gains, K_p' and K_{pa}' were examined. The examination of gains leaded to K_p' = 600 [-] and K_{pa}' = 125 [-], as the better ones. Figs. 3.17 to 3.19 show the experimental uncontrolled and controlled time history responses of strains at the same position in the calculations, respectively. The maximum and minimum strains of uncontrolled system in positive and negative sides were 359.40×10^{-6} and -440.40×10^{-6}, as shown in Fig. 3.17. By using P-controller they became 262.40×10^{-6} and -373.40×10^{-6}, as shown in Fig. 3.18.Moreover, by using AF-controller they became 175.50×10^{-6} and -303.50×10^{-6}, as shown in Fig. 3.19.

Moreover, as shown in Chapter 2, Figs 2.17, 2.18 and 2.20 shows the uncontrolled and controlled calculated time history response of strains at Node 6 of Model C1.2. The calculated results on the controlled system were obtained using the same control strategies used in the experiments. The Experimental and calculated results for uncontrolled and controlled system show the effectiveness and validity of the proposed control scheme and strategies as well as the superiority of the proposed AF control compared to the P one to suppress the vibration of the flexible single-link manipulator.

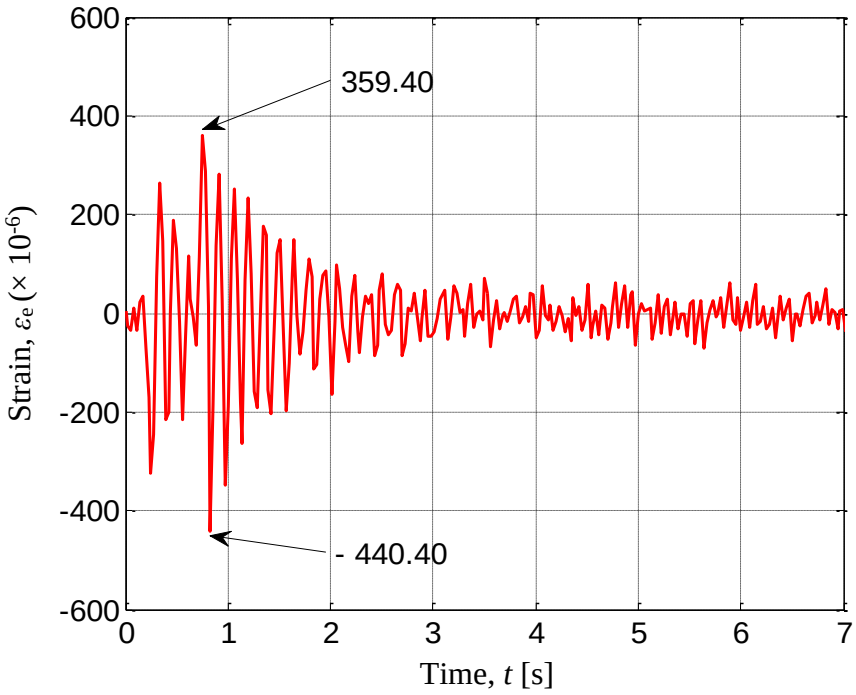

Fig. 3.17 Experimental time history response of strains at 0.11 [m] from the origin of the link for uncontrolled system due to base excitation

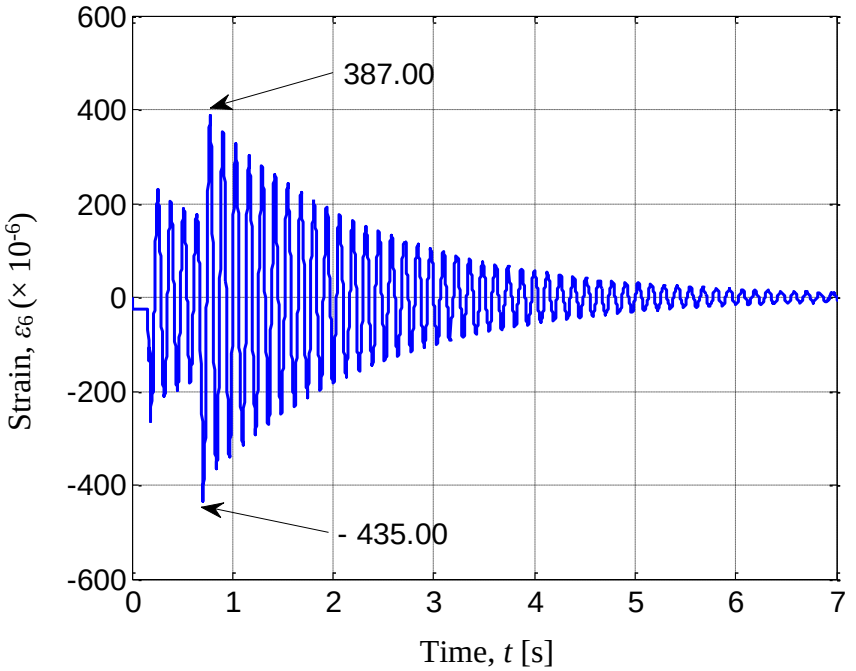

Fig. 2.17 Calculated time history response of strains at Node 6 for uncontrolled Model C1.2 due to base excitation (previously shown in Page 28)

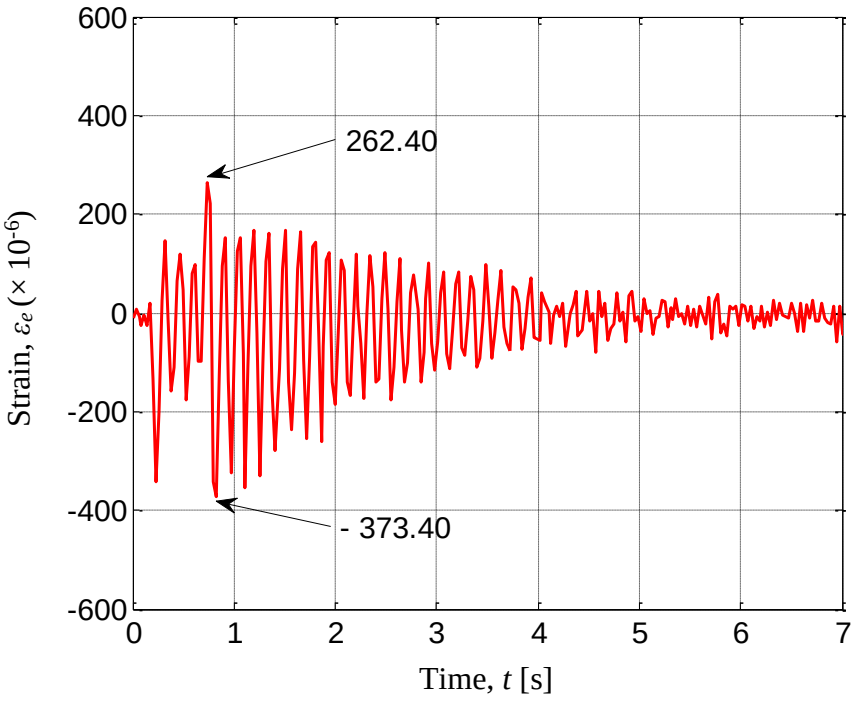

Fig. 3.18 Experimental time history response of strains for controlled system at 0.11 [m] from the origin of the link due to base excitation using P-controller (K_p' = 600 [-])

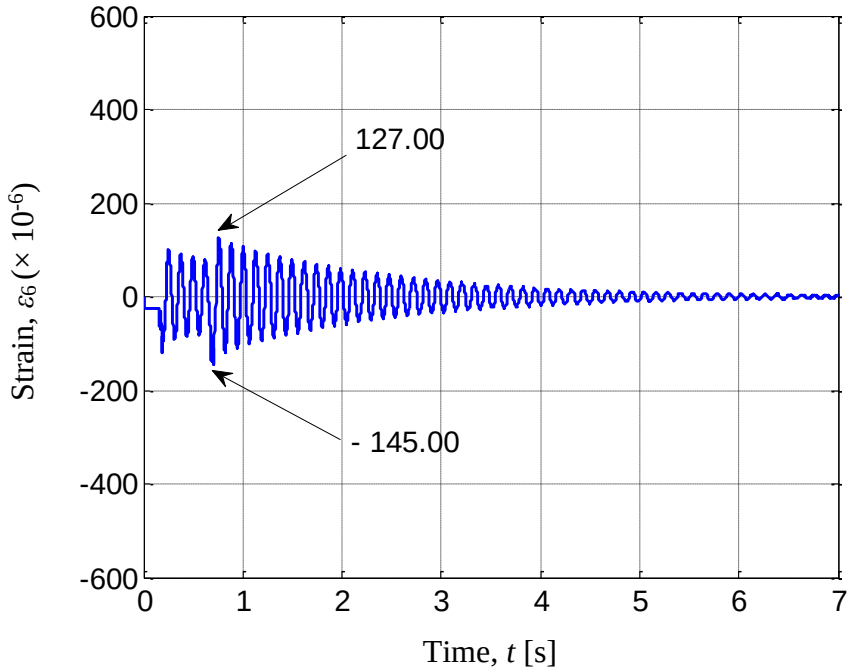

Fig. 2.18 Calculated time history response of strains at Node 6 for controlled Model C1.2 due to base excitation using P-controller (K_p = 30 [Nm])
(previously shown in Page 28)

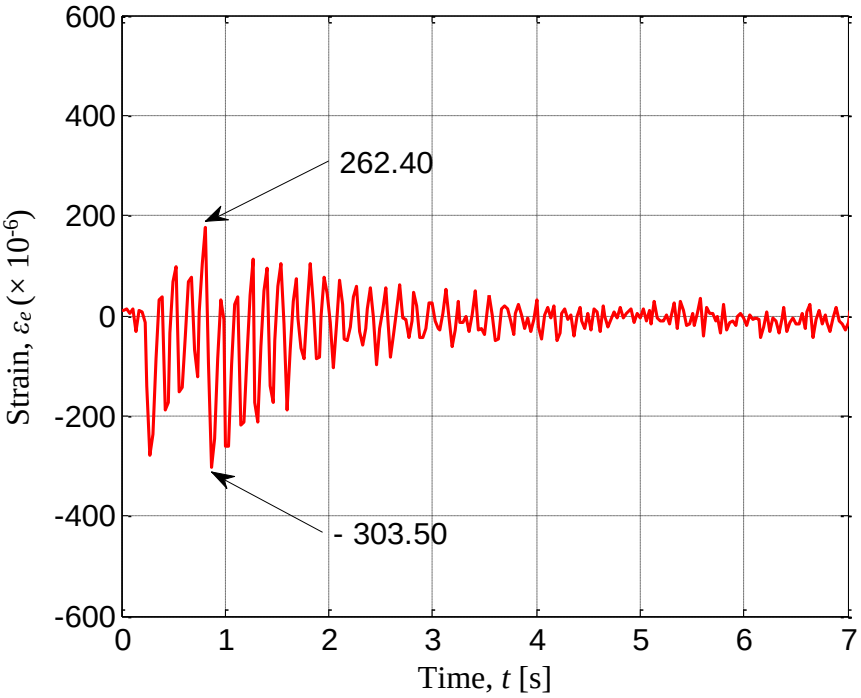

Fig. 3.19 Experimental time history response of strains for controlled system at 0.11 [m] from the origin of the link due to base excitation using AF-controller (K_{pa}' = 125 [-]) (previously shown in Page 29)

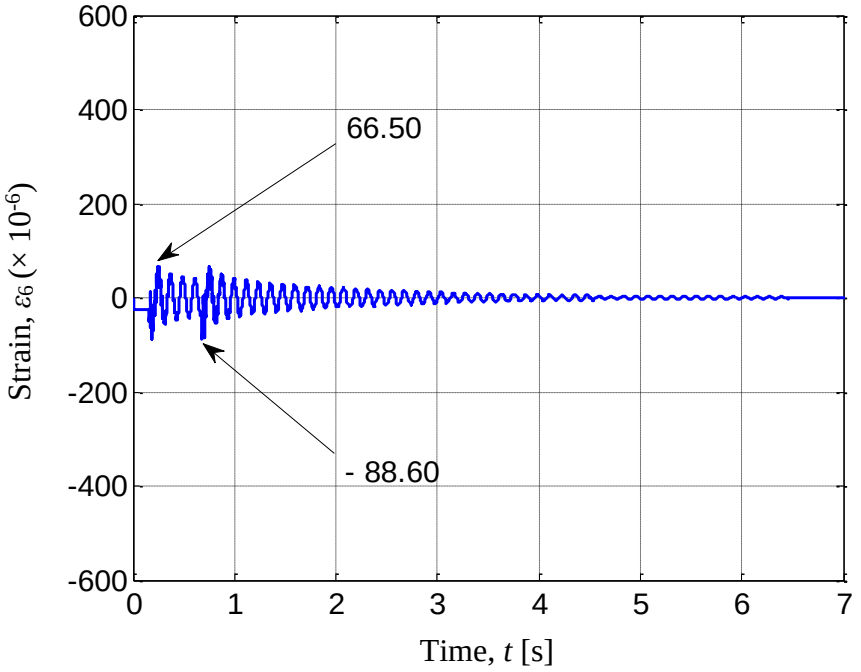

Fig. 2.20 Calculated time history response of strains at Node 6 for controlled Model C1.2 due to base excitation using AF-controller (K_{pa} = 0.4 [-]) (previously shown in Page 29)

3.7 Conclusions

Experimental models and set-up had been developed in order to carry out dynamic experiments of the flexible single-link system. Experimental results on time history responses and natural frequencies show the validity of the formulation, computational codes and modeling of the system. The proportional (P) and active-force (AF) controls were implemented to suppress the vibration of the system. Their performances were compared through the experiments. Experimental results on controlled system show the validity of the proposed control scheme and strategies as well as the superiority of the proposed AF control compared to the P one to suppress the vibration of the flexible single-link manipulator.

Chapter 4

Formulation and Computational Simulations on Vibration Control of a Flexible Two-link Manipulator Using Finite Element Method

4.1 Introduction

The purposes of study presented in this chapter are to derive the equations of motion of a flexible two-link system by a finite element method, to develop the computational codes in order to perform dynamics simulations with vibration control and to propose an effective control scheme of a flexible two-link manipulator using three control strategies, namely proportional (P), proportional-derivative (PD) and active-force (AF) controls.

The flexible two-link manipulator used in this chapter consists of two aluminum beams as flexible links, two aluminum clamp-parts, two servo motors to rotate the links, piezoelectric actuators to control vibration and a base. Computational codes on time history responses, FFT (Fast Fourier Transform) processing and eigenvalues - eigenvectors analysis were developed to calculate the dynamic behavior of the link. An end-effector that treated as a concentrated mass was introduced to demonstrate a complete flexible two-link manipulator system. Furthermore, the P, PD and AF controls strategies were designed to suppress the vibration of the system. It was done by adding

bending moments generated by the piezoelectric actuators to the two-link. Finally, their performances were compared through the calculations.

4.2 Formulation by Finite Element Method

The link has been discretized by finite elements. Every finite element (Element i-th) has two nodes namely Node i and Node (i+1). Every node (Node i) has three degrees of freedom, namely the longitudinal deformation $u_i(x,t)$, the lateral deformation $v_i(x,t)$, and the rotational angle $\psi_i(x,t)$. The longitudinal deformation $u_i(x,t)$ is very small compared to the lateral deformation $v_i(x,t)$. The length, the cross-sectional area and the area moment of inertia around z-axis of every element are denoted by l_i, S_i and I_{zi} respectively. Mechanical properties of every element are denoted as Young's modulus E_i and mass density ρ_i.

4.2.1 Kinematics

Figure 4.1 shows the position vectors $\boldsymbol{r}_{p1}$ and $\boldsymbol{r}_{p2}$ of arbitrary points P_1 and P_2 on Link 1 and Link 2 in the global and rotating coordinate frames. Let the links as flexible beams have a motion that is confined in the horizontal plane as shown in Fig. 4.1. The $O - XY$ frame is the global coordinate frame with Z-axis is fixed. Furthermore, $o_1 - x_1y_1$ and $o_2 - x_2y_2$ are the rotating coordinate frames fixed to the root of Link 1 and Link 2, respectively (z_1-axis and z_2-axis are fixed). The unit vectors in X, Y, x_1, y_1, x_2 and y_2 axes are denoted by $\boldsymbol{I}$, $\boldsymbol{J}$, $\boldsymbol{i}_1$, $\boldsymbol{j}_1$, $\boldsymbol{i}_2$ and $\boldsymbol{j}_2$, respectively. The first motor is installed on the root of the Link 1. The second motor that treated as a concentrated mass is installed in the root of the Link 2. The rotational angles of the first and second motor when the links rotate are denoted by $\theta_1(t)$ and $\theta_2(t)$. Length of Link 1 is donated by L_1. Lateral

deformation of the arbitrary points P_1 and P_2 in the first and the second links are donated by v_{p1} and v_{p2}, respectively. Lateral deformation and rotational angel of the end-point of the first link are donated by v_e and ψ_e, respectively. The position vectors $\boldsymbol{r}_{p1}$ and $\boldsymbol{r}_{p2}$ of the arbitrary points P_1 and P_2 at time $t = t$, measured in the $O - XY$ frame shown in Fig. 1 are expressed by

$$\boldsymbol{r}_{p1} = X_{p1}(x_1, \theta_1, v_{p1}, t)\boldsymbol{I} + Y_{p1}(x_1, \theta_1, v_{p1}, t)\boldsymbol{J}, \tag{4.1}$$

$$\boldsymbol{r}_{p2} = X_{p2}(x_2, \theta_1, \theta_2, v_e, \psi_e, v_{p2}, t)\boldsymbol{I} + Y_{p2}(x_2, \theta_1, \theta_2, v_e, \psi_e, v_{p2}, t)\boldsymbol{J}, \tag{4.2}$$

where

$$X_{p1} = x_1 \cos\theta_1(t) - v_{p1}(x_1, t)\sin\theta_1(t), \tag{4.3}$$

$$Y_{p1} = x_1 \sin\theta_1(t) + v_{p1}(x_1, t)\cos\theta_1(t), \tag{4.4}$$

$$X_{p2} = L_1 \cos\theta_1(t) - v_e(x_1, t)\sin\theta_1(t) + x_2 \cos\big(\theta_1(t) + \psi_e(x_1, t) + \theta_2(t)\big) - \tag{4.5}$$

$$v_{p2}(x_2, t)\sin\big(\theta_1(t) + \psi_e(x_1, t) + \theta_2(t)\big),$$

$$Y_{p2} = L_1 \sin\theta_1(t) + v_e(x_1, t)\cos\theta_1(t) + x_2 \sin\big(\theta_1(t) + \psi_e(x_1, t) + \theta_2(t)\big) + \tag{4.6}$$

$$v_{p2}(x_2, t)\cos\big(\theta_1(t) + \psi_e(x_1, t) + \theta_2(t)\big).$$

The velocity vectors of the arbitrary points P_1 and P_2 at time $t = t$, shown in Fig.1 are expressed by

$$\dot{\boldsymbol{r}}_{p1} = \dot{X}_{p1}(x_1, \theta_1, \dot{\theta}_1, v_{p1}, \dot{v}_{p1}, t)\boldsymbol{I} + \dot{Y}_{p1}(x_1, \theta_1, \dot{\theta}_1, v_{p1}, \dot{v}_{p1}, t)\boldsymbol{J}, \tag{4.7}$$

$$\dot{\boldsymbol{r}}_{p2} = \dot{X}_{p2}(x_2, \theta_1, \theta_2, \dot{\theta}_1, \dot{\theta}_2, v_e, \psi_e, v_{p2}, \dot{v}_e, \dot{\psi}_e, \dot{v}_{p2}, t)\boldsymbol{I} + \tag{4.8}$$

$$\dot{Y}_{p1}(x_2, \theta_1, \theta_2, \dot{\theta}_1, \dot{\theta}_2, v_e, \psi_e, v_{p2}, \dot{v}_e, \dot{\psi}_e, \dot{v}_{p2}, t)\boldsymbol{J}\ .$$

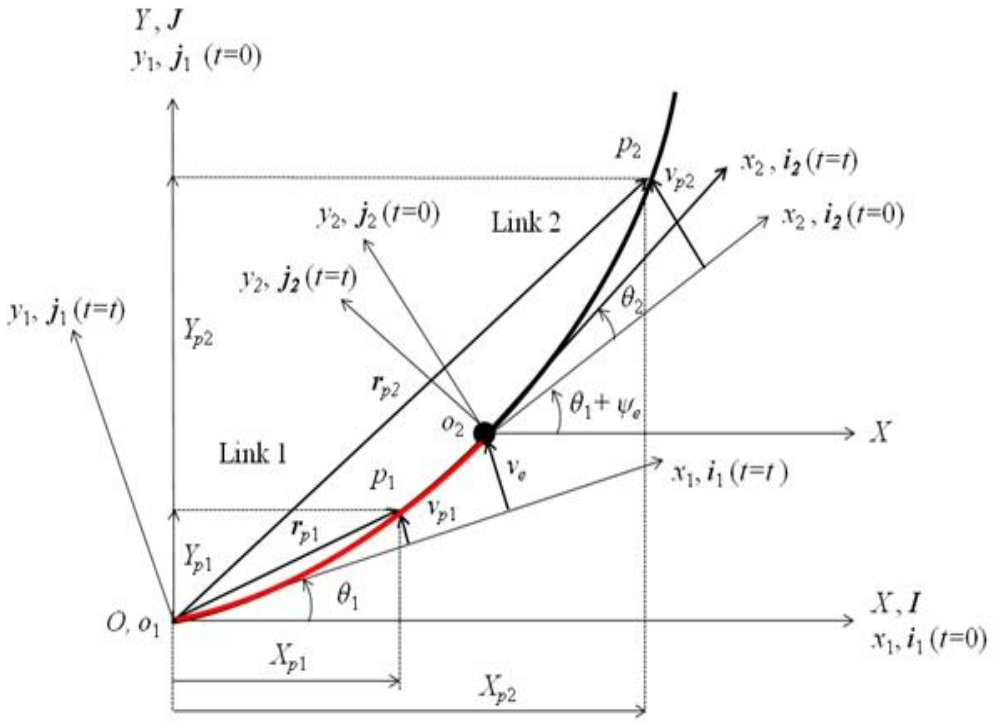

O-XY	: Global coordinate frame
o_1-x_1y_1	: Rotating coordinate frame fixed to Link 1
o_2-x_2y_2	: Rotating coordinate frame fixed to Link 2
$\mathbf{r}_{p1}$, $\mathbf{r}_{p2}$	: Position vectors of the arbitrary points p_1 and p_2 in the *X*-axis of the *O-XY*
θ_1	: Rotational angle of the first motor
θ_2	: Rotational angle of the second motor
X_{p1}, X_{p2}	: Coordinates of the arbitrary points p_1 and p_2 in the *X*-axis of the *O-XY*
Y_{p1}, Y_{p2}	: Coordinates of the arbitrary points p_1 and p_2 in the *Y*-axis of the *O-XY*
v_{p1}	: Lateral deformation of the arbitrary point p_1 on Link 1 in the o_1-x_1y_1
v_{p2}	: Lateral deformation of the arbitrary point p_2 on Link 2 in the o_2-x_2y_2
ψ_e	: Rotational angle of the end-point of Link 1
v_e	: Lateral deformation of the end-point of Link 1
L_1	: Length of Link 1

Fig. 4.1 Position vectors of arbitrary points P_1 and P_2 in the global and rotating coordinate frames

4.2.2 Finite Element Procedure

Finite element procedure used in this chapter has been completely presented in Chapter 2. Therefore, only main procedure will be presented in this chapter. Figure 4.2 shows the rotating coordinate frame and the link divided by one-dimensional and two-node elements. Then, Fig. 4.3 shows the element coordinate frame of Element *i*, and an arbitrary point *P* in Element *i*. Here, there are six boundary conditions together at nodes *i* and (*i*+1) when the one-dimensional and two-node element is used. The six boundary conditions are expressed as nodal deformation vector as follow

$$\boldsymbol{\delta}_i = \{u_i \quad v_i \quad \psi_i \quad u_{i+1} \quad v_{i+1} \quad \psi_{i+1}\}^T . \tag{4.9}$$

Furthermore, the relation between the lateral deformation v_i and the rotational angle ψ_i of the Node *i* is given by

$$\psi_i = \frac{\partial v_i}{\partial x_i} . \tag{4.10}$$

Moreover, from mechanics of materials, the strain of Node *i* can be defined by

$$\varepsilon_i = -y_i \frac{\partial^2 v_i}{\partial x_i^{\,2}} , \tag{4.11}$$

where y_i is position coordinate of the arbitrary point *P* in the y_i-axis of the element coordinate frame.

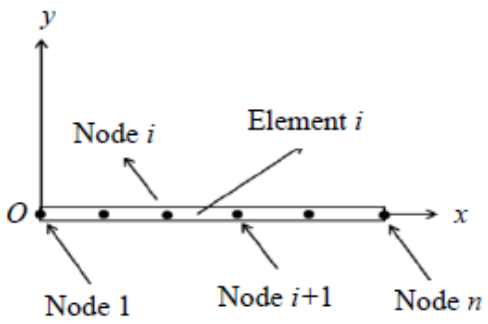

Fig.4.2 Rotating coordinate frame and the link divided by the one-dimensional and two-node elements

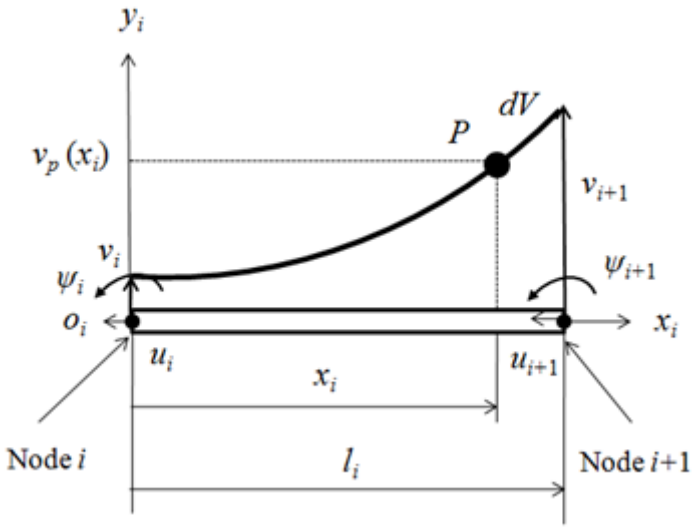

$o_i - x_i\, y_i$: Element coordinate frame of Element i

Fig.4.3 Element coordinate frame of Element i

The strains ε_i is related to the nodal deformation vector $\boldsymbol{\delta}_i$ of Element i by $\boldsymbol{B}_i$ - matrix as follows

$$\varepsilon_i = \boldsymbol{B}_i \boldsymbol{\delta}_i \,. \tag{4.12}$$

Furthermore, the stress and strain of Element i are related by

$$\sigma_i = \boldsymbol{D}_i \varepsilon_i \,, \tag{4.13}$$

where $\boldsymbol{D}_i$ is a square symmetric matrix that depends on the mechanical properties of Element i, in this case can be reduced as Young's modulus E.

4.2.3 Kinetic Energy

The kinetic energy for Element i is defined as [68]

$$\boldsymbol{T}_i = \frac{1}{2} \int_{V_i} \rho_i \dot{\boldsymbol{r}}^T \dot{\boldsymbol{r}} dV. \tag{4.14}$$

where ρ_i and V_i are the mass density and volume of Element i, respectively.

Firstly, for Link 1, based on Eqs. (4.1), (4.3) and (4.4), the velocity square of P_1 can be obtained as

$$\dot{\boldsymbol{r}}_{p1}{}^{T}\dot{\boldsymbol{r}}_{p1}(x_1,t) = x_1{}^{2}\dot{\theta}_1{}^{2} + \dot{v}_{p1}{}^{2} + v_{p1}{}^{2}\dot{\theta}_1{}^{2} + 2x_1\dot{v}_1\dot{\theta}_1 . \tag{4.15}$$

Moreover, the value of x_1 can be defined as follow

$$x_1 = l_{1-i} + x_i , \tag{4.16}$$

where l_{1-i} is length from Node 1 to Node i

$$l_{1-i} = l_1 + l_2 + ... + l_{i-1} . \tag{4.17}$$

Substituting Eq. (4.16) to Eq. (4.15) gives

$$\dot{\boldsymbol{r}}_{p1}{}^{T}\dot{\boldsymbol{r}}_{p1}(x_i,t) = (l_{1-i} + x_i)^2\dot{\theta}^2 + \dot{v}^2 + v^2\dot{\theta}^2 + 2(l_{1-i} + x_i)\dot{v}\dot{\theta}. \tag{4.18}$$

Substituting Eq. (4.18) to Eq. (4.14) gives the kinetic energy for Element i on Link 1 as follows

$$\boldsymbol{T}_i = \frac{7}{6}m_i l_{1-i}{}^{2}\dot{\theta}_1{}^{2} + \frac{1}{2}\dot{\boldsymbol{\delta}}_i{}^{T}\boldsymbol{M}_i\dot{\boldsymbol{\delta}}_i + \frac{1}{2}\boldsymbol{\delta}_i{}^{T}\dot{\theta}_1{}^{2}\boldsymbol{M}_i\boldsymbol{\delta}_i + \dot{\theta}_1\,\boldsymbol{f}_i{}^{T}\dot{\boldsymbol{\delta}}_i , \tag{4.19}$$

where

$$\boldsymbol{f}_i{}^{T} = \frac{\rho_i S_i l_i}{60}\begin{Bmatrix} 0 & 30l_{1-i} + 9l_i & 5l_{1-i}l_i + 2l_i{}^{2} & 0 & 21l_i & -5l_{1-i}l_i + 3l_i \end{Bmatrix} . \tag{4.20}$$

Furthermore, the mass matrix $\boldsymbol{M}_i$ of Element i on Link 1 can be expressed as

$$\boldsymbol{M}_i = \frac{\rho_i S_i l_i}{420}\begin{bmatrix} 156 & 0 & 22l_i & 54 & 0 & -13l_i \\ 0 & 156 & 22l_i & 0 & 54 & -13l_i \\ 0 & 22l_i & 4l_i{}^{2} & 0 & 13l_i & -3l_i{}^{2} \\ 54 & 0 & 13l_i & 156 & 0 & -22l_i \\ 0 & 54 & 13l_i & 0 & 156 & -22l_i \\ 0 & -13l_i & -3l_i{}^{2} & 0 & -22l_i & 4l_i{}^{2} \end{bmatrix}. \tag{4.21}$$

Secondly, for Link 2, based on Eqs. (4.2), (4.5) and (4.6), the velocity square of P_1 can be obtained as

$$\begin{aligned}
&\dot{\boldsymbol{r}}_{p2}{}^{T}\dot{\boldsymbol{r}}_{p2}(x_2,t) = L_1{}^2\dot{\theta}_1{}^2 + x_2{}^2\left(\dot{\theta}_1+\dot{\psi}_e+\dot{\theta}_2\right)^2 + v_e{}^2\dot{\theta}_1{}^2 + v_{p2}{}^2\left(\dot{\theta}_1+\dot{\psi}_e+\dot{\theta}_2\right)^2 + \dot{v}_e{}^2 \\
&+ \dot{v}_{p2}{}^2 + 2L_1\dot{\theta}_2{}^2\dot{v}_e + 2x_2\left(\dot{\theta}_1+\dot{\psi}_e+\dot{\theta}_2\right)\dot{v}_{p2} + 2L_1x_2\dot{\theta}_1\left(\dot{\theta}_1+\dot{\psi}_e+\dot{\theta}_2\right)\cos\left(\psi_e+\theta_2\right) \\
&+ 2L_1\dot{\theta}_1\dot{v}_{p2}\cos\left(\psi_e+\theta_2\right) - 2L_1v_{p2}\dot{\theta}_1\left(\dot{\theta}_1+\dot{\psi}_e+\dot{\theta}_2\right)\sin\left(\psi_e+\theta_2\right) \\
&+ 2x_2\left(\dot{\theta}_1+\dot{\psi}_e+\dot{\theta}_2\right)\dot{v}_e\cos\left(\psi_e+\theta_2\right) + 2\dot{v}_e\dot{v}_{p2}\cos\left(\psi_e+\theta_2\right) \\
&- 2v_{p2}\left(\dot{\theta}_1+\dot{\psi}_e+\dot{\theta}_2\right)\dot{v}_e\sin\left(\psi_e+\theta_2\right) + 2x_2v_e\dot{\theta}_1\left(\dot{\theta}_1+\dot{\psi}_e+\dot{\theta}_2\right)\sin\left(\psi_e+\theta_2\right) \\
&+ 2v_e\dot{\theta}_1\dot{v}_{p2}\sin\left(\psi_e+\theta_2\right) + 2v_ev_{p2}\dot{\theta}_1\left(\dot{\theta}_1+\dot{\psi}_e+\dot{\theta}_2\right)\cos\left(\psi_e+\theta_2\right)
\end{aligned} \quad . (4.22)$$

Moreover, the value of x_1 can be defined as follow

$$x_2 = l_{1-i} + x_i\,, \tag{4.23}$$

where l_{1-i} is length from Node 1 to Node i

$$l_{1-i} = l_1 + l_2 + ... + l_{i-1}\,. \tag{4.24}$$

Substituting Eq. (4.23) to Eq. (4.22) then to Eq. (4.14) gives the kinetic energy for Element i on Link 2 as follows

$$\begin{aligned}
&\boldsymbol{T}_i = \frac{1}{2}m_iL_1{}^2\dot{\theta}_1{}^2 + \frac{7}{6}m_il_{1-i}{}^2\left(\dot{\theta}_1+\dot{\psi}_e+\dot{\theta}_2\right)^2 + \frac{1}{2}m_iv_e{}^2\dot{\theta}_1{}^2 + \frac{1}{2}\dot{\boldsymbol{\delta}}_i{}^T\boldsymbol{M}_i\dot{\boldsymbol{\delta}}_i \\
&+ \frac{1}{2}\boldsymbol{\delta}_i{}^T\left(\dot{\theta}_1+\dot{\psi}_e+\dot{\theta}_2\right)^2\boldsymbol{M}_i\boldsymbol{\delta}_i + \frac{1}{2}m_i\dot{v}_e{}^2 + m_iL_1\dot{\theta}_2\dot{v}_e + \left(\dot{\theta}_1+\dot{\psi}_e+\dot{\theta}_2\right)\boldsymbol{f}_i{}^T\dot{\boldsymbol{\delta}}_i \\
&+ \frac{3}{2}m_il_{1-i}L_1\dot{\theta}_1\left(\dot{\theta}_1+\dot{\psi}_e+\dot{\theta}_2\right)\cos\left(\psi_e+\theta_2\right) - L_1\dot{\theta}_1\cos\left(\psi_e+\theta_2\right)\boldsymbol{g}_i{}^T\dot{\boldsymbol{\delta}}_i \\
&+ L_1\dot{\theta}_1\left(\dot{\theta}_1+\dot{\psi}_e+\dot{\theta}_2\right)\sin\left(\psi_e+\theta_2\right)\boldsymbol{g}_i{}^T\boldsymbol{\delta}_i + \frac{3}{2}m_il_{1-i}\dot{v}_e\left(\dot{\theta}_1+\dot{\psi}_e+\dot{\theta}_2\right)\cos\left(\psi_e+\theta_2\right). \\
&- \dot{v}_e\cos\left(\psi_e+\theta_2\right)\boldsymbol{g}_i{}^T\dot{\boldsymbol{\delta}}_i + \frac{1}{2}\dot{v}_e\left(\dot{\theta}_1+\dot{\psi}_e+\dot{\theta}_2\right)\sin\left(\psi_e+\theta_2\right)\boldsymbol{g}_i{}^T\boldsymbol{\delta}_i \\
&+ \frac{3}{2}m_il_{1-i}v_e\dot{\theta}_1\left(\dot{\theta}_1+\dot{\psi}_e+\dot{\theta}_2\right)\sin\left(\psi_e+\theta_2\right) - v_e\dot{\theta}_1\sin\left(\psi_e+\theta_2\right)\boldsymbol{g}_i{}^T\dot{\boldsymbol{\delta}}_i \\
&- v_e\dot{\theta}_1\left(\dot{\theta}_1+\dot{\psi}_e+\dot{\theta}_2\right)\cos\left(\psi_e+\theta_2\right)\boldsymbol{g}_i{}^T\boldsymbol{\delta}_i
\end{aligned} \tag{4.25}$$

where

$$\boldsymbol{f}_i^{\,T} = \frac{\rho_i S_i l_i}{60}\left\{0 \quad 30l_{1-i} + 9l_i \quad 5l_{1-i}l_i + 2l_i^{\,2} \quad 0 \quad 21l_i \quad -5l_{1-i}l_i + 3l_i\right\}, \tag{4.26}$$

$$\boldsymbol{g}_i^{\,T} = \frac{\rho_i S_i l_i}{12}\left\{0 \quad -6 \quad 15l_i \quad 0 \quad 6 \quad l_i\right\}. \tag{4.27}$$

Furthermore, the mass matrix $\boldsymbol{M}_i$ of Element *i* on Link 2 can be expressed as

$$\boldsymbol{M}_i = \frac{\rho_i S_i l_i}{420}\begin{bmatrix} 156 & 0 & 22l_i & 54 & 0 & -13l_i \\ 0 & 156 & 22l_i & 0 & 54 & -13l_i \\ 0 & 22l_i & 4l_i^{\,2} & 0 & 13l_i & -3l_i^{\,2} \\ 54 & 0 & 13l_i & 156 & 0 & -22l_i \\ 0 & 54 & 13l_i & 0 & 156 & -22l_i \\ 0 & -13l_i & -3l_i^{\,2} & 0 & -22l_i & 4l_i^{\,2} \end{bmatrix}. \tag{4.28}$$

4.2.4 Strain Energy

The strain energy for Element *i* is defined as [68]

$$\boldsymbol{U}_i = \frac{1}{2}\int_{V_i} \varepsilon_i^{\,T}\sigma_i dV_i. \tag{4.29}$$

Substituting Eqs. (4.12) and (4.13) to Eq. (4.29) gives

$$\boldsymbol{U}_i = \frac{1}{2}\boldsymbol{\delta}_i^{\,T}\left[\int_{\tau} \boldsymbol{B}_i^{\,T}\boldsymbol{D}_i\boldsymbol{B}_i d\tau\right]\boldsymbol{\delta}_i. \tag{4.30}$$

Equation (4.30) can be rewritten as

$$\boldsymbol{U}_i = \frac{1}{2}\boldsymbol{\delta}_i^{\,T}\boldsymbol{K}_i\boldsymbol{\delta}_i. \tag{4.31}$$

Substituting Eq. (4.12) and *E* to Eq. (4.30) within integral limit of *0* to l_i then the stiffness matrix $\boldsymbol{K}_i$ for Links 1 and 2 can be expressed as follows

$$\boldsymbol{K}_i = \frac{E_i I_{zi}}{l_i^{\,3}} \begin{bmatrix} \frac{S_i l_i^{\,2}}{I_{zi}} & 0 & 0 & -\frac{S_i l_i^{\,2}}{I_{zi}} & 0 & 0 \\ 0 & 12 & 6l_i & 0 & -12 & -6l_i \\ 0 & 6l_i & 4l_i^{\,2} & 0 & -6l & 2l_i^{\,2} \\ -\frac{S_i l_i^{\,2}}{I_{zi}} & 0 & 0 & \frac{S_i l_i^{\,2}}{I_{zi}} & 0 & 0 \\ 0 & -12 & -6l_i & 0 & 12 & -6l_i \\ 0 & 6l_i & 2l_i^{\,2} & 0 & -6l_i & 4l_i^{\,2} \end{bmatrix}. \tag{4.32}$$

4.2.5 Equations of Motion

Firstly, for Link 1, substituting Eqs. (4.19) and (4.31) into Lagrange's equation, the equation of motion for Element *i* on Link 1 can be obtained as follows

$$\boldsymbol{M}_i \ddot{\boldsymbol{\delta}}_i + \boldsymbol{C}_i \dot{\boldsymbol{\delta}}_i + \left[\boldsymbol{K}_i - \dot{\theta}_1^{\,2} \boldsymbol{M}_i \right] \boldsymbol{\delta}_i = \ddot{\theta}_1 \boldsymbol{f}_i . \tag{4.33}$$

Secondly, for Link 2, substituting Eqs. (4.25) and (4.31) into Lagrange's equation, the equation of motion for Element *i* on Link 2 can be obtained as follows

$$\begin{aligned} &\boldsymbol{M}_i \ddot{\boldsymbol{\delta}}_i + \boldsymbol{C}_i \dot{\boldsymbol{\delta}}_i + \left[\boldsymbol{K}_i - \left(\dot{\theta}_1 + \dot{\psi}_e + \dot{\theta}_2 \right)^2 \boldsymbol{M}_i \right] \boldsymbol{\delta}_i = \left(\ddot{\theta}_1 + \ddot{\psi}_e + \ddot{\theta}_2 \right) \boldsymbol{f}_i \\ &+ \left(L_1 \ddot{\theta}_1 + \ddot{v}_e - v_e \dot{\theta}_1^{\,2} \right) \cos\left(\psi_e + \theta_2 \right) \boldsymbol{g}_i \\ &+ \left(v_e \ddot{\theta}_1 + L_1 \dot{\theta}_1^{\,2} + \frac{1}{2} \dot{v}_e \left(3\dot{\theta}_1 - \dot{\psi}_e - \dot{\theta}_2 \right) \right) \sin\left(\psi_e + \theta_2 \right) \boldsymbol{g}_i \end{aligned} . \tag{4.34}$$

The damping matrix $\boldsymbol{C_i}$ for Element *i* can be calculated by using the Rayleigh damping factor α as follows

$$\boldsymbol{C}_i = \alpha \boldsymbol{K}_i . \tag{4.35}$$

Finally, for the whole link which is discretized as *n*-element, the sum of kinetic and strain energies from element 1 to *n* are respectively given by

$$\boldsymbol{T}_n = \sum_{i=1}^{n} \boldsymbol{T}_i \,, \tag{4.36}$$

$$\boldsymbol{U}_n = \sum_{i=1}^{n} \boldsymbol{U}_i \,. \tag{4.37}$$

Therefore, the equations of motion for Link 1 and 2 as *n*-element are respectively given by adapting Eqs (4.36) and (4.37) and considering the boundary conditions as follows

$$\boldsymbol{M}_n \ddot{\boldsymbol{\delta}}_n + C_n \dot{\boldsymbol{\delta}}_n + \left[\boldsymbol{K}_n - \dot{\theta}_1^{\,2} \boldsymbol{M}_n\right] \boldsymbol{\delta}_n = \ddot{\theta}_1 \, \boldsymbol{f}_n \,, \tag{4.38}$$

$$\begin{aligned} &\boldsymbol{M}_n \ddot{\boldsymbol{\delta}}_n + \boldsymbol{C}_n \dot{\boldsymbol{\delta}}_n + \left[\boldsymbol{K}_n - \left(\dot{\theta}_1 + \dot{\psi}_e + \dot{\theta}_2\right)^2 \boldsymbol{M}_n\right] \boldsymbol{\delta}_n = \left(\ddot{\theta}_1 + \ddot{\psi}_e + \ddot{\theta}_2\right) \boldsymbol{f}_n \\ &+ \left(L_1 \ddot{\theta}_1 + \ddot{v}_e - v_e \dot{\theta}_1^{\,2}\right) \cos\left(\psi_e + \theta_2\right) \boldsymbol{g}_n \\ &+ \left(v_e \ddot{\theta}_1 + L_1 \dot{\theta}_1^{\,2} + \frac{1}{2} \dot{v}_e \left(3\dot{\theta}_1 - \dot{\psi}_e - \dot{\theta}_2\right)\right) \sin\left(\psi_e + \theta_2\right) \boldsymbol{g}_n \end{aligned} \,. \tag{4.39}$$

4.3 Computational Models

In this chapter, we defined and used four types of computational models of the flexible two-link manipulator.

4.3.1 Model C2.1

A model of a flexible single-link with a clamp-part was used as Model C2.1. Figure 4.4 shows Model C2.1. The links and the clamp-parts were discretized by 35 elements. Two strain gages are bonded to the position of Node 6 and Node 22 of the two-link (0.11 [m] and 0.38 [m] from the origin), respectively.

4.3.2 Model C2.2

A model of the flexible two-link manipulator including one piezoelectric actuator was defined as Model C2.2. Figure 4.5 shows Model C2.2. The piezoelectric actuator

was bonded to the one surface of Elements 4. The links including the clamp-parts and the piezoelectric actuator were discretized by 36 elements. A schematic representation on modeling of the piezoelectric actuator is shown in Fig. 4.8. Furthermore, Two strain gages are bonded to the position of Node 6 and Node 22 of the two-link (0.11 [m] and 0.38 [m] from the origin), respectively. Physical parameters of the single-link model and the piezoelectric actuator are shown in Table 4.1.

The piezoelectric actuator suppressed the vibration of the flexible two-link manipulator by adding bending moments at Nodes 3 and 6, M_3 and M_6 to the flexible link. The bending moments are generated by applying voltages $+E$ to the piezoelectric actuator as shown in Fig. 4.8. The relation between the bending moments and the voltages are related by

$$M_3 = -M_6 = d_{11}E_1 . \tag{4.40}$$

Here d_{11} is a constant quantity.

Furthermore, the voltage to generate the bending moments is proportional to the strain ε of the two-link due to the vibration. The relation can be expressed as follows

$$E_1 = \pm\frac{1}{d_{21}}\varepsilon_1 . \tag{4.41}$$

Here d_{21} is a constant quantity.

4.3.3 Model C2.3

A model of the flexible two-link manipulator including two piezoelectric actuators was defined as Model C2.3. Figure 4.6 shows Model C2.3. The piezoelectric actuators were bonded to the one surface of elements 4 and 20. The links including the clamp-parts and the piezoelectric actuators were discretized by 36 elements. Schematic

representations on modeling of the piezoelectric actuators are shown in Figs. 4.8 and 4.9. Physical parameters of the flexible two-link manipulator model and the piezoelectric actuators are shown in Table 4.1.

The first piezoelectric actuator suppresses the vibration of the two-link flexible manipulator by adding bending moments at nodes 3 and 6 of the two-link manipulator, M_3 and M_6. The second piezoelectric actuator suppresses the vibration of the two-link flexible manipulator by adding bending moments at nodes 19 and 22 of the two-link manipulator, M_{19} and M_{22}. The bending moments are generated by applying voltages E_1 and E_2 to the actuators. The bending moments proportional to the voltages which are expressed by Eq. (4.41) and

$$M_{19} = -M_{22} = d_{12} E_2 . \tag{4.42}$$

Here d_{12} is a constant quantity and M_{19} opposites to M_{22}.

Furthermore, the voltages to generate the bending moments are proportional to the strains ε_1 and ε_2 of the two-link due to the vibration. The relations can be expressed by Eq. (4.41) and

$$E_2 = \pm \frac{1}{d_{22}} \varepsilon_2 . \tag{4.43}$$

Here d_{22} is a constant quantity. Then, d_{11}, d_{12}, d_{21} and d_{22} will be determined by comparing the calculated results and experimental ones.

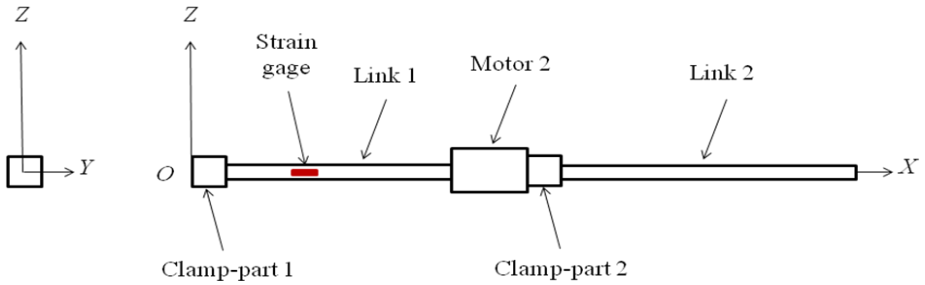

Fig.4.4 Model C2.1: Only flexible two-link

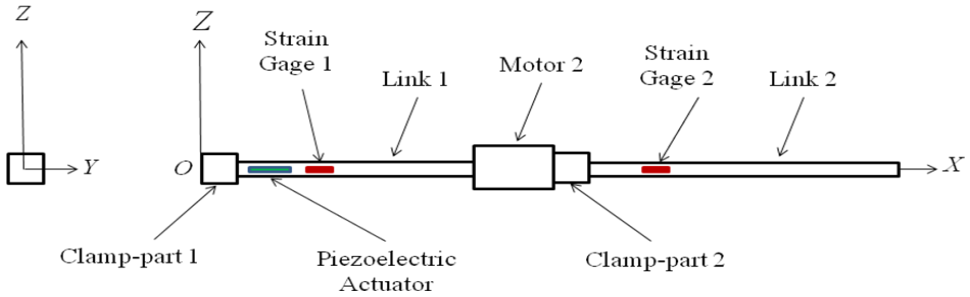

Fig.4.5 Model C2.2: Flexible two-link with a piezoelectric actuator

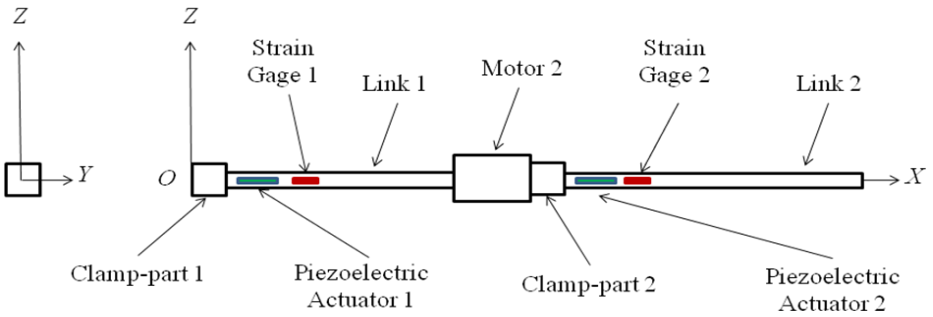

Fig.4.6 Model C2.3: Flexible two-link with piezoelectric actuators

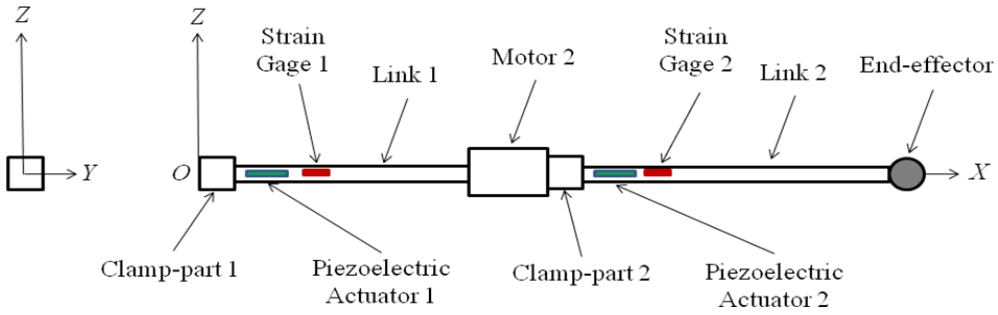

Fig.4.7 Model C2.4: Flexible two-link with a piezoelectric actuator and an end-effector

4.3.4 Model C2.4

Figure 4.7 shows Model C2.4 that an end-effector of the two-link manipulator is considered. Model C2.4 is used to show that the proposed control strategies are also suitable for such system. The end-effector is presented by adding a concentrated mass to Model C2.2. Therefore, the kinetic energy of the tip element was increased due to the concentrated mass.

Table 4.1: Physical parameters of the flexible two-link and the piezoelectric actuators

l : Total length	m	4.05×10^{-1}
l_1 : Length of Link 1	m	1.90×10^{-1}
l_2 : Length of Link 2	m	2.15×10^{-1}
l_{c1}, l_{c2} : Length of clamp-parts 1 and 2	m	1.50×10^{-2}
l_{a1}, l_{a2} : Length of Actuators 1 and 2	m	2.00×10^{-2}
S_{l1}, S_{l2} : Cross section area of links 1 and 2	m^2	1.95×10^{-5}
S_{c1}, S_{c2} : Cross section area of clamp-parts 1 and 2	m^2	8.09×10^{-4}
S_{a1}, S_{a2} : Cross section area of actuators 1 and 2	m^2	1.58×10^{-5}
I_{zl1}, I_{zl2} : Cross section area moment of inertia around z-axis of links 1 and 2	m^4	2.75×10^{-12}
I_{zc1}, I_{zc2} : Cross section area moment of inertia around z-axis of clamp-parts 1 and 2	m^4	3.06×10^{-8}
I_{za1}, I_{za2} : Cross section area moment of inertia around z-axis of actuators 1 and 2	m^4	1.61×10^{-11}
E_{l1}, E_{l2} : Young's Modulus of links 1 and 2	GPa	7.03×10^{1}
E_{c1}, E_{c2} : Young's Modulus of clamp-parts 1 and 2	GPa	7.03×10^{1}
E_{a1}, E_{a2} : Young's Modulus of actuators 1 and 2	GPa	4.40×10^{1}
ρ_{l1}, ρ_{l2} : Density of links 1 and 2	kg/m^3	2.68×10^{3}
ρ_{c1}, ρ_{c2} : Density of clamp-parts 1 and 2	kg/m^3	2.68×10^{3}
ρ_{a1}, ρ_{a2} : Density of actuators 1 and 2	kg/m^3	3.33×10^{3}
α_1, α_2 : Damping factor of links 1 and 2	s	2.50×10^{-4}
E_1, E_2 : Maximum input voltages of actuators 1 and 2	V	150.00
F_1, F_2 : Maximum output forces of actuators 1 and 2	N	200.00
m_2 : Mass of the second motor and it's clamping system	g	113.53

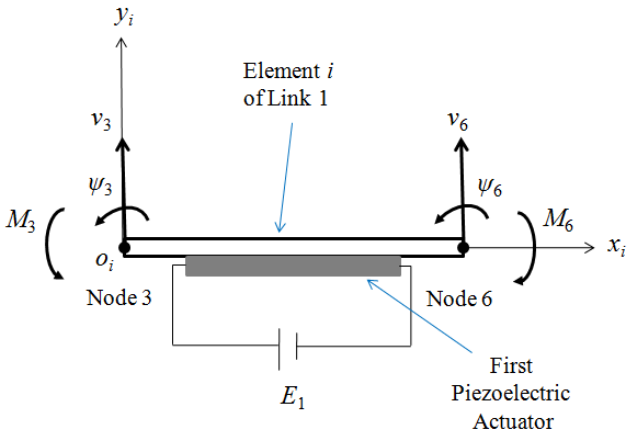

Fig.4.8 Modeling of first piezoelectric actuator (top view)

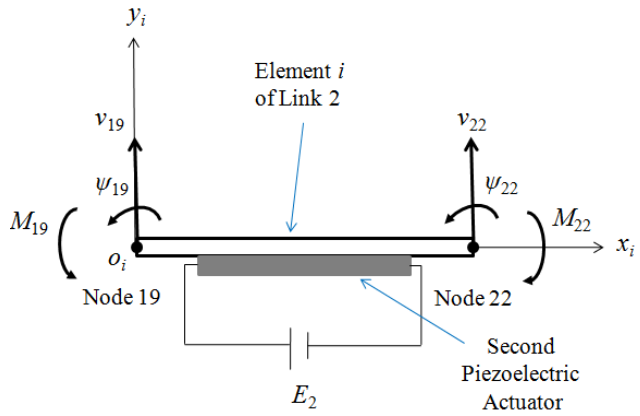

Fig.4.9 Modeling of second piezoelectric actuator (top view)

Applying the kinetic energy and the strain energy to Lagrange's equation, so the equation of motion of the tip element containing the concentrated mass is given by

$$\begin{aligned}&\left[\boldsymbol{M}_i+\boldsymbol{M}_{icm}\right]\ddot{\boldsymbol{\delta}}_i+\boldsymbol{C}_i\dot{\boldsymbol{\delta}}_i+\left[\boldsymbol{K}_i-\left(\dot{\theta}_1+\dot{\psi}_e+\dot{\theta}_2\right)^2\left[\boldsymbol{M}_i+\boldsymbol{M}_{icm}\right]\right]\boldsymbol{\delta}_i=\\&\left(\ddot{\theta}_1+\ddot{\psi}_e+\ddot{\theta}_2\right)\left\{\boldsymbol{f}_i+\boldsymbol{f}_{icm}\right\}+\\&\left(L_1\ddot{\theta}_1+\ddot{v}_e-v_e\dot{\theta}_1^{\,2}\right)\cos\left(\psi_e+\theta_2\right)\left\{\boldsymbol{g}_i+\boldsymbol{g}_{icm}\right\}+\\&\left(v_e\ddot{\theta}_1+L_1\dot{\theta}_1^{\,2}+\frac{1}{2}\dot{v}_e\left(3\dot{\theta}_1-\dot{\psi}_e-\dot{\theta}_2\right)\right)\sin\left(\psi_e+\theta_2\right)\left\{\boldsymbol{g}_i+\boldsymbol{g}_{icm}\right\}\end{aligned}\quad . \tag{4.44}$$

where the vector of $\boldsymbol{f}_{icm}$ and $\boldsymbol{g}_{icm}$ are given by

$$\boldsymbol{f}_{icm}=m_c\left\{0\quad 0\quad 0\quad 0\quad -\left(l_{1-i}+l_i\right)\quad 0\right\}^T, \tag{4.45}$$

$$\boldsymbol{g}_{icm} = m_c \begin{Bmatrix} 0 & 0 & 0 & 0 & -1 & 0 \end{Bmatrix}^T . \tag{4.46}$$

The concentrated mass matrix M_{icm} can be expressed as

$$\boldsymbol{M}_{icm} = \begin{bmatrix} 0 & 0 & 0 & 0 & 0 & 0 \\ 0 & 0 & 0 & 0 & 0 & 0 \\ 0 & 0 & 0 & 0 & 0 & 0 \\ 0 & 0 & 0 & 0 & 0 & 0 \\ 0 & 0 & 0 & 0 & m_c & 0 \\ 0 & 0 & 0 & 0 & 0 & 0 \end{bmatrix}. \tag{4.47}$$

where m_c is the mass of the concentrated mass.

4.4 Control Scheme and Strategies

A control scheme to suppress the vibration of the two-link system was designed using one and two piezoelectric actuators. It was done by adding bending moments generated by the piezoelectric actuators to the two-link system. To drive the actuator, three different control strategies namely P, PD and AF controls have been designed and examined. Their performances were compared through calculations.

4.4.1 Using a Piezoelectric Actuator

The piezoelectric actuator suppresses the vibration of the two-link flexible manipulator by adding bending moments at Nodes 3 and 6 of the two-link manipulator, M_3 and M_6. Therefore, the equation of motion of Link 1 become

$$\boldsymbol{M}_n \ddot{\boldsymbol{\delta}}_n + C_n \dot{\boldsymbol{\delta}}_n + \left[\boldsymbol{K}_n - \dot{\theta}_1^{\,2} \boldsymbol{M}_n\right] \boldsymbol{\delta}_n = \ddot{\theta}_1 \, \boldsymbol{f}_n + \boldsymbol{u}_{1n} . \tag{4.48}$$

where the vector of $\boldsymbol{u}_{1n}$ containing M_3 and M_6 is the control force generated by the actuator to the two-link system. The control strategies used for the two-link system with one piezoelectric actuator are similar to the control strategies used in Chapter 2.

4.4.1.1 Proportional Control

Based on Eq. (4.40) and Eq. (4.41) the bending moments can be defined in term of the P-controller as follows

$$M_3 = -M_6 = K_p\left(\varepsilon_d(s) - \varepsilon_6(s)\right), \tag{4.49}$$

where ε_d and ε_6 denote the desired and measured strains at Node 6, respectively.

A block diagram of the P-controller for the two-link system using one actuator is shown in Fig. 4.10.

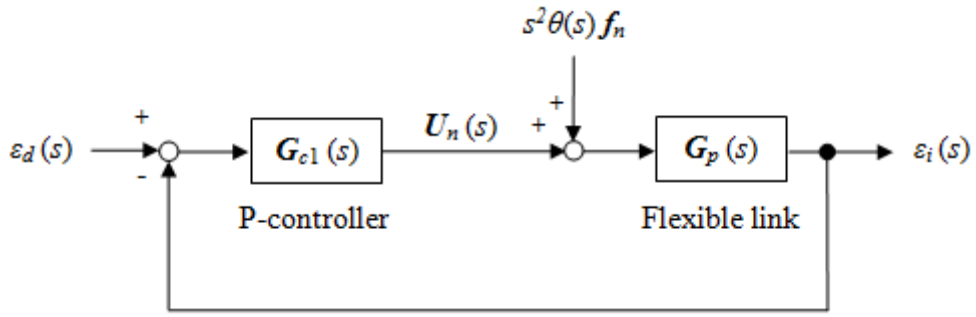

ε_d : Desired strain
ε_i : Measured strains at Node *i*
$\boldsymbol{F}$: Base excitations
$\boldsymbol{U}_n$: Applied bending moments

Fig. 4.10 Block diagram of proportional control of the flexible two-link manipulator

4.4.1.2 Proportional-Derivative Control

Based on Eq. (4.40) and Eq. (4.41) the bending moments can be defined in term of the P-controller as follows

$$M_3 = -M_6 = \left(K_p + K_d\, s\right)\left(\varepsilon_d(s) - \varepsilon_6(s)\right), \tag{4.50}$$

where ε_d and ε_6 denote the desired and measured strains at Node 6, respectively.

A block diagram of the PD-controller for the two-link system using one actuator is shown in Fig. 4.11.

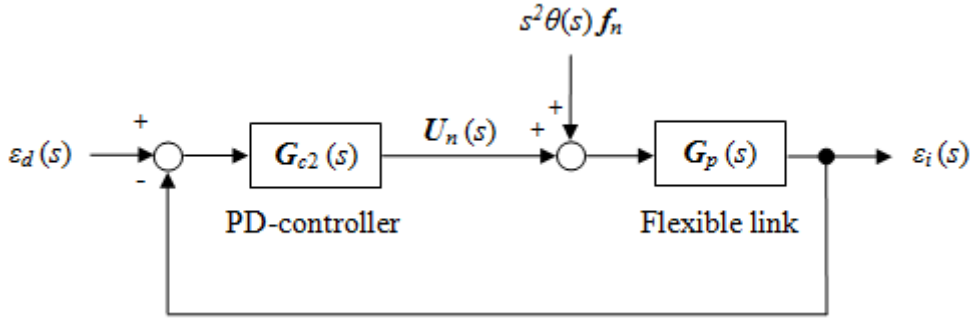

ε_d : Desired strain
ε_i : Measured strains at Node i
$\boldsymbol{F}$: Base excitations
$\boldsymbol{U}_n$: Applied bending moments

Fig. 4.11 Block diagram of proportional-derivative control of the flexible two-link manipulator

4.4.1.3 Active-force Control

Figure 4.12 shows a block diagram of the AF control that is proposed in this study. In this strategy, vibration of the system is controlled by canceling bending moments acting at Nodes 3 and 6 due to the base excitation (excitation bending moments). The following steps are the way to estimate and cancel the excitation bending moments.

Firstly, the strain, ε_6 at Node 6 is measured to estimate the lateral deformation, v_6 at Node 6. As explained in Chapter 2, the relation between the strain and the lateral deformation can be defined as follows

$$\frac{v_6}{\varepsilon_6} = -\frac{x^2(x-3l)}{6y(x-l)} = A, \tag{4.51}$$

where l, x and y are the length of the link, the position of Node 6 in x and y directions, respectively.

Secondly, the actual force in the s-domain acting at Node 6 can be defined in the form of the Newton's equation of motion as follows

$$F_6(s) = M_{ii(i=11)}\, s^2\, v_6, \tag{4.52}$$

where $M_{ii(i=11)}$ is the component of the mass matrix corresponding to v_6.

Thirdly, the bending moments acting at Nodes 3 and 6 are estimated using the following equation

$$\boldsymbol{U}_{nt}(s) = \pm F_6(s)\boldsymbol{d} \,. \tag{4.53}$$

The vector $\boldsymbol{d}$ that represents the position vector from the reference point to the position where the excitation force acting can be written as follows

$$\boldsymbol{d} = \{0 \quad 0 \quad 0 \quad 0 \quad 0 \quad l_2 \quad 0 \quad 0 \quad 0 \quad 0 \quad 0 \quad l_2 \quad \ldots \quad 0\}^T, \tag{4.54}$$

where l_2 is distance from the reference point to the position where the excitation force acting.

Fourthly, based on Fig. 4.12, the excitation bending moments can be calculated as

$$\boldsymbol{U}_{ne}(s) = K_{pa}\{\boldsymbol{U}_{nt}(s) - \boldsymbol{U}_n(s)\}, \tag{4.55}$$

where K_{pa} is the non-dimensional proportional gain of the proposed AF control.

Finally, the bending moments applying as a control force to control the vibration of the system can be calculated as follows

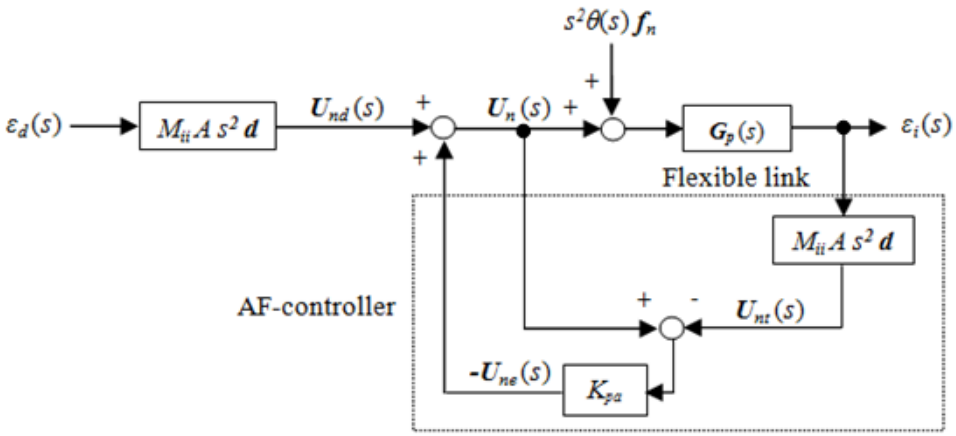

ε_d : Desired strain
$\boldsymbol{F}$: Base excitations
A : Conversion from ε_i to v_i
$\boldsymbol{U}_{nd}$: Desired bending moments
$\boldsymbol{U}_{ne}$: Excitation bending moments
ε_i : Measured strains at Node i
M_{ii} : Component of mass matrix
$\boldsymbol{d}$: Position vector
$\boldsymbol{U}_n$: Applied bending moments
$\boldsymbol{U}_{nt}$: Bending moments

Fig. 4.12 Block diagram of active-force control of the flexible two-link manipulator

$$\boldsymbol{U}_n(s) = -\boldsymbol{U}_{ne}(s) + \boldsymbol{U}_{nd}(s), \tag{4.56}$$

where $\boldsymbol{U}_{nd}(s)$ is the desired bending moments which is zero. The negative of $\boldsymbol{U}_{ne}(s)$ indicates that the bending moments were used to cancel the vibration of the system.

4.4.2 Using Two Piezoelectric Actuator

The first piezoelectric actuator suppresses the vibration of the two-link flexible manipulator by adding bending moments at nodes 3 and 6 of the two-link manipulator, M_3 and M_6, as explained in Sub-Chapter 4.4.1. The second piezoelectric actuator suppresses the vibration of the two-link flexible manipulator by adding bending moments at Nodes 19 and 22 of the two-link manipulator, M_{19} and M_{22}. Therefore, the equation of motion of Link 1 is shown in Eq. (4.49) and the equation of motion of Link 2 in given by

$$\begin{aligned}
&\boldsymbol{M}_n\ddot{\boldsymbol{\delta}}_n + \boldsymbol{C}_n\dot{\boldsymbol{\delta}}_n + \left[\boldsymbol{K}_n - \left(\dot{\theta}_1 + \dot{\psi}_e + \dot{\theta}_2\right)^2 \boldsymbol{M}_n\right]\boldsymbol{\delta}_n = \left(\ddot{\theta}_1 + \ddot{\psi}_e + \ddot{\theta}_2\right)\boldsymbol{f}_n \\
&+ \left(L_1\ddot{\theta}_1 + \ddot{v}_e - v_e\dot{\theta}_1^{\,2}\right)\cos\left(\psi_e + \theta_2\right)\boldsymbol{g}_n \\
&+ \left(v_e\ddot{\theta}_1 + L_1\dot{\theta}_1^{\,2} + \frac{1}{2}\dot{v}_e\left(3\dot{\theta}_1 - \dot{\psi}_e - \dot{\theta}_2\right)\right)\sin\left(\psi_e + \theta_2\right)\boldsymbol{g}_n + u_{2n}
\end{aligned}, \tag{4.57}$$

where the vector of $\boldsymbol{u}_{2n}$ containing M_{19} and M_{22} is the second control force generated by the second piezoelectric actuator to the two-link system.

4.4.2.1 Proportional Controls

Based on Eqs. (4.40), (4.41), (4.42) and (4.43) the bending moments can be respectively defined in term of the first and second P-controllers as follows

$$M_3 = -M_6 = K_{p1}\left(\varepsilon_d(s) - \varepsilon_6(s)\right), \tag{4.58}$$

$$M_{19} = -M_{22} = K_{p2}\left(\varepsilon_d(s) - \varepsilon_{22}(s)\right), \tag{4.59}$$

where ε_d, ε_6 and ε_{22} denote the desired and measured strains at Node 6 and Node 22, respectively.

A block diagram of the P-controller for the two-link system using two actuators is shown in Fig. 4.13.

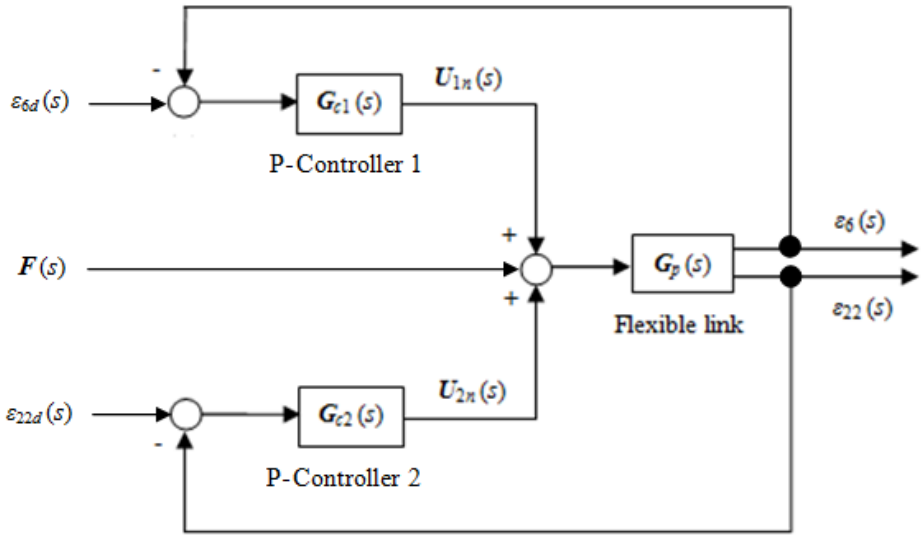

ε_d : Desired strain — ε_6 and ε_{22} : Measured strains at Nodes 6 and 22
$\boldsymbol{F}$: Base excitations — $\boldsymbol{U}_{1n}$ and $\boldsymbol{U}_{2n}$: Bending moments generated by actuator 1 and 2

Fig. 4.13 Block diagram of proportional controls of the flexible two-link manipulator using two piezoelectric actuators

4.4.2.2 Proportional-Derivative Controls

Based on Eqs. (4.40), (4.41), (4.42) and (4.43) the bending moments can be respectively defined in term of the first and second PD-controllers as follows

$$M_3 = -M_6 = \left(K_{p1} + K_{d1}\, s\right)\left(\varepsilon_d(s) - \varepsilon_6(s)\right), \tag{4.60}$$

$$M_{19} = -M_{22} = \left(K_{p2} + K_{d2}\, s\right)\left(\varepsilon_d(s) - \varepsilon_{22}(s)\right), \tag{4.61}$$

where ε_d, ε_6 and ε_{22} denote the desired and measured strains at Node 6 and Node 22, respectively.

A block diagram of the PD-controllers for the two-link system using two actuators is shown in Fig. 4.14.

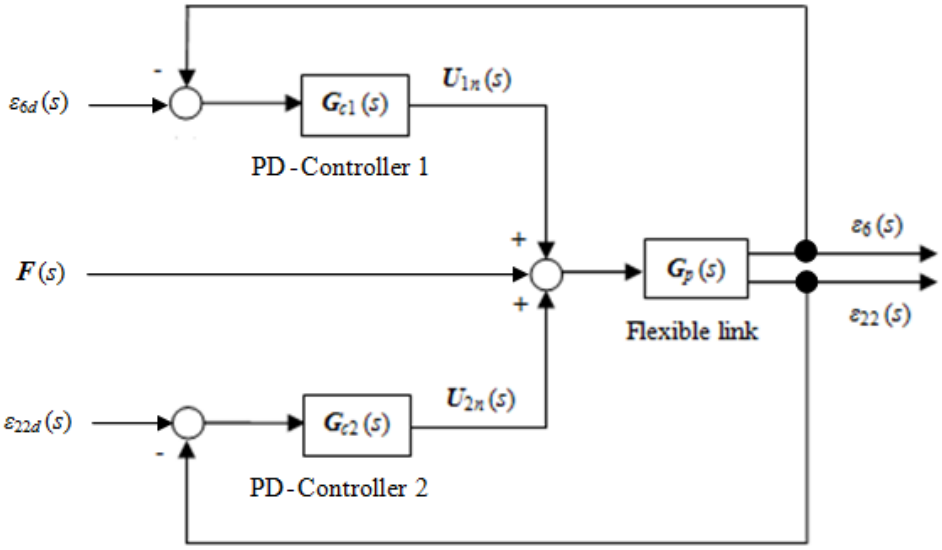

ε_d : Desired strain — ε_6 and ε_{22} : Measured strains at Nodes 6 and 22
$\boldsymbol{F}$: Base excitations — $\boldsymbol{U}_{1n}$ and $\boldsymbol{U}_{2n}$: Bending moments generated by actuator 1 and 2

Fig. 4.14 Block diagram of proportional-derivative controls of the flexible two-link manipulator using two piezoelectric actuators

4.4.2.3 Active-force Controls

Figure 4.15 shows a block diagram of the AF-controls that are proposed in this study. In this strategy, vibration of the system is controlled by canceling bending moments due to the base excitation (excitation bending moments) acting at Nodes 3 and 6 using the first piezoelectric actuator and Nodes 19 and 22 using the second piezoelectric actuator. The following steps are the way to estimate and cancel the excitation bending moments.

Firstly, the strains at Nodes 6 and 22, ε_6 and ε_{22} are measured to estimate the lateral deformation at Nodes 6 and 22, v_6 and v_{22}. As explained in Chapter 2, the relations between the strains and the lateral deformations at Nodes 6 and 22 can be respectively defined as follows

$$\frac{v_6}{\varepsilon_6} = -\frac{x_6^{\,2}(x_6 - 3l)}{6y_6(x_6 - l)} = A_6\,, \tag{4.62}$$

$$\frac{v_{22}}{\varepsilon_{22}} = -\frac{x_{22}{}^2\left(x_{22}-3l\right)}{6y_{22}\left(x_{22}-l\right)} = A_{22}, \tag{4.63}$$

where l, x_6, x_{22}, y_6, and y_{22} are the length of the link, the positions of Nodes 6 and 22 in x and y directions, respectively.

Secondly, the actual force in the s-domain acting at Nodes 6 and 22 can be respectively defined in the form of the Newton's equation of motion as follows

$$F_6(s) = M_{ii(i=14)}\, s^2\, v_6, \tag{4.64}$$

$$F_{22}(s) = M_{ii(i=62)}\, s^2\, v_{22}, \tag{4.65}$$

where $M_{ii(i=14)}$ and $M_{ii(i=62)}$ are the components of the mass matrix corresponding to v_6 and v_{22}.

Thirdly, the bending moments acting at Nodes 3 and 6 and the bending moments acting at Nodes 19 and 22 are estimated using the following equations

$$\boldsymbol{U}_{nt6}(s) = \pm F_6(s)\boldsymbol{d}_6, \tag{4.66}$$

$$\boldsymbol{U}_{nt22}(s) = \pm F_{22}(s)\boldsymbol{d}_{22}. \tag{4.67}$$

The vector $\boldsymbol{d}_6$ and $\boldsymbol{d}_{22}$ represent the position vectors from the reference points to the position where the excitation forces acting.

Fourthly, based on Fig. 4.15, the excitation bending moments can be calculated as

$$\boldsymbol{U}_{ne6}(s) = K_{pa1}\left\{\boldsymbol{U}_{nt6}(s) - \boldsymbol{U}_{n6}(s)\right\} \tag{4.68}$$

$$\boldsymbol{U}_{ne22}(s) = K_{pa2}\left\{\boldsymbol{U}_{nt22}(s) - \boldsymbol{U}_{n22}(s)\right\} \tag{4.69}$$

where K_{pa1} and K_{pa2} are the non-dimensional proportional gains of the proposed AF control.

Finally, the bending moments applying as control forces to control the vibration of the system can be calculated as follows

$$\boldsymbol{U}_{n6}(s) = -\boldsymbol{U}_{ne6}(s) + \boldsymbol{U}_{nd6}(s), \tag{4.70}$$

$$\boldsymbol{U}_{n22}(s) = -\boldsymbol{U}_{ne22}(s) + \boldsymbol{U}_{nd22}(s), \tag{4.71}$$

where $\boldsymbol{U}_{nd6}(s)$ and $\boldsymbol{U}_{nd22}(s)$ are the desired bending moments at Nodes 6 and 22 which are zero. The negative of $\boldsymbol{U}_{ne6}(s)$ and $\boldsymbol{U}_{ne22}(s)$ indicate that the bending moments were used to cancel the vibration of the system.

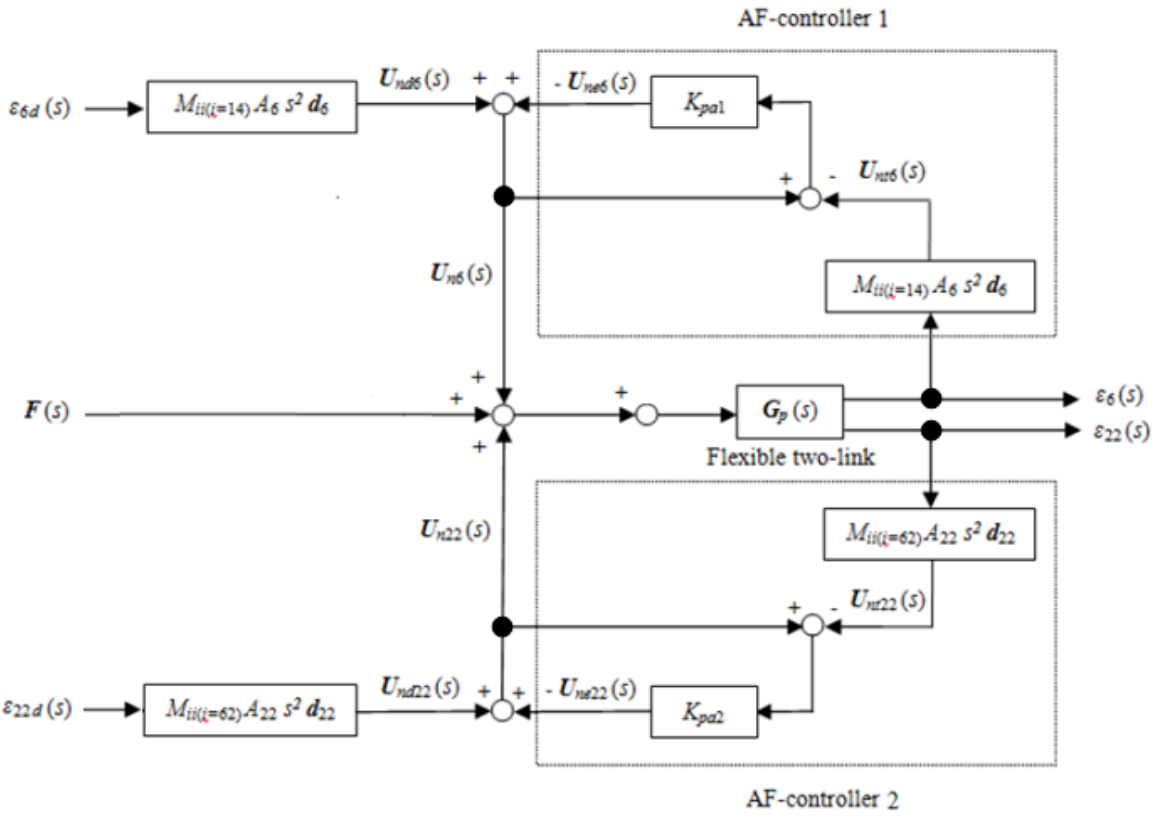

ε_d : Desired strain
$\boldsymbol{F}$: Base excitations
A_6 : Conversion from ε_6 to v_6
A_6 : Conversion from ε_6 to v_6
$\boldsymbol{U}_{nd6}$: Desired bending moments at Node 6
$\boldsymbol{U}_{nd22}$: Desired bending moments at Node 22
$\boldsymbol{U}_{ne6}$: Excitation bending moments at Node 6
$\boldsymbol{U}_{ne22}$: Excitation bending moments at Node 22
$M_{ii(i=14)}$: Component of mass matrix corresponding to v_6
$M_{ii(i=14)}$: Component of mass matrix corresponding to v_6
ε_6 : Measured strains at Node 6
ε_{22} : Measured strains at Node 22
$\boldsymbol{d}_6$: Position vector of Node 6
$\boldsymbol{d}_{22}$: Position vector of Node 22
$\boldsymbol{U}_{n6}$: Applied bending moments at Node 6
$\boldsymbol{U}_{n22}$: Applied bending moments at Node 22
$\boldsymbol{U}_{nt6}$: Bending moments at Node 6
$\boldsymbol{U}_{nt22}$: Bending moments at Node 22

Fig. 4.15 Block diagram of active-force controls of the flexible two-link manipulator

4.5 Calculated Results

4.5.1 Time History Response on Free Vibration

Model C2.1 was used to calculate time history response of strains for the flexible two-link manipulator using an impulse force as an external one. Computational codes on time history response of strains for Model C2.1 were developed based on formulation explained in Sub-Chapter 4.2. Figure 2.11 shows the calculated time history response of strains at Node 3 of Model C1.1 under the impulse force.

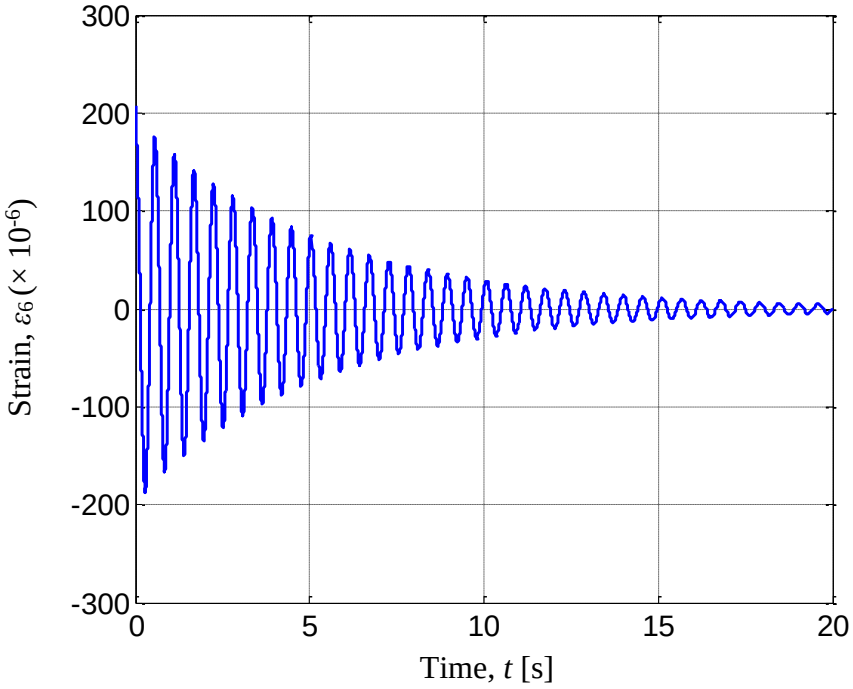

Fig. 4.16 Calculated time history response of strains on free vibration at Node 6 of Model C2.1

4.5.2 Fast Fourier Transform Processing

The calculated time history response of strains on free vibration of Model C2.1 was transferred by FFT processing to find its frequencies. Figure 4.17 show the calculated natural frequencies of the flexible link manipulator. The first and second calculated natural frequencies are 1.80 [Hz] and 8.95 [Hz], respectively.

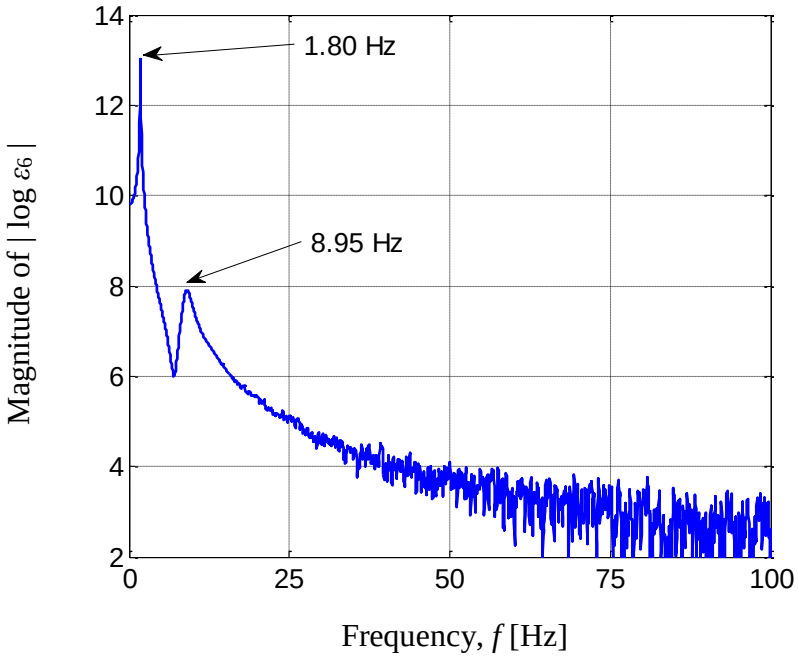

Fig. 4.17 Calculated time history response of strains on free vibration at Node 6 of Model C2.1

4.5.3 Eigenvalues and Eigenvectors Analysis

Eigenvalues - eigenvectors analysis for the flexible two-link manipulator were done using Model C2.1. Computational codes on eigenvalues - eigenvectors analysis were developed to find natural frequencies and vibration modes. Eigenvalues – eigenvectors analysis for two conditions namely straight and elbow.

Firstly, the analysis for straight condition was done with $\theta_1 = \theta_2 = 0$ radian. The calculated results of the first and second natural frequencies for straight condition were 1.79 [Hz] and 8.92 [Hz], respectively. Vibration modes of the natural frequencies are shown in Figs. 4.18 and 4.19.

Secondly, the analysis for elbow condition was done with $\theta_1 = 0$ radian, $\theta_2 = \pi/2$ radians (90 degrees). Link 2 was rotated using a rotation matrix show in Eq. (4.73). The calculated results of the first and second natural frequencies for straight condition were

2.00 [Hz] and 9.97 [Hz], respectively. Vibration modes of the natural frequencies are shown in Figs. 4.20 and 4.21.

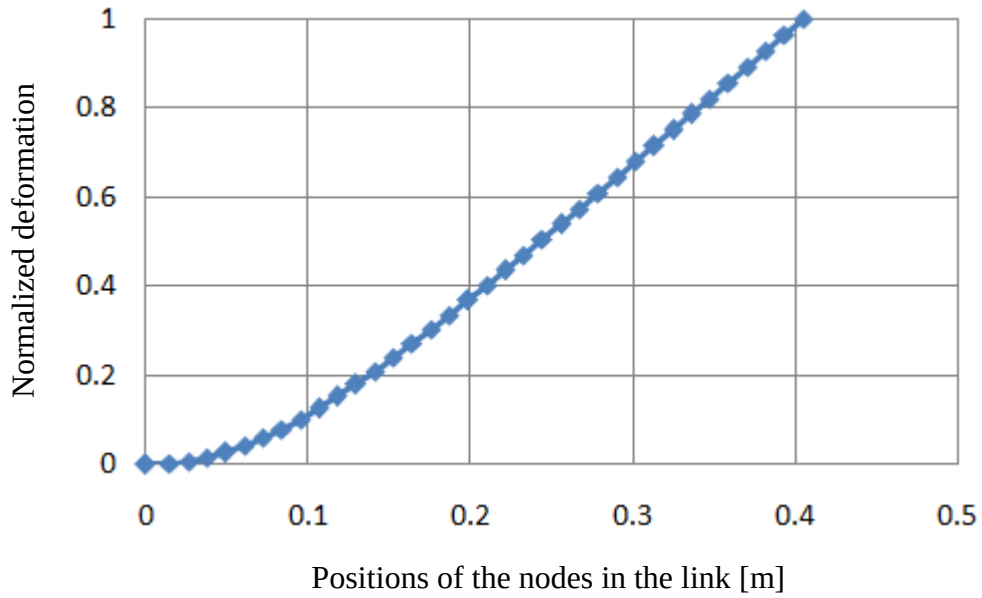

Fig. 4.18 First vibration mode and natural frequency (f_1 = 1.79 Hz) of straight Model C2.1

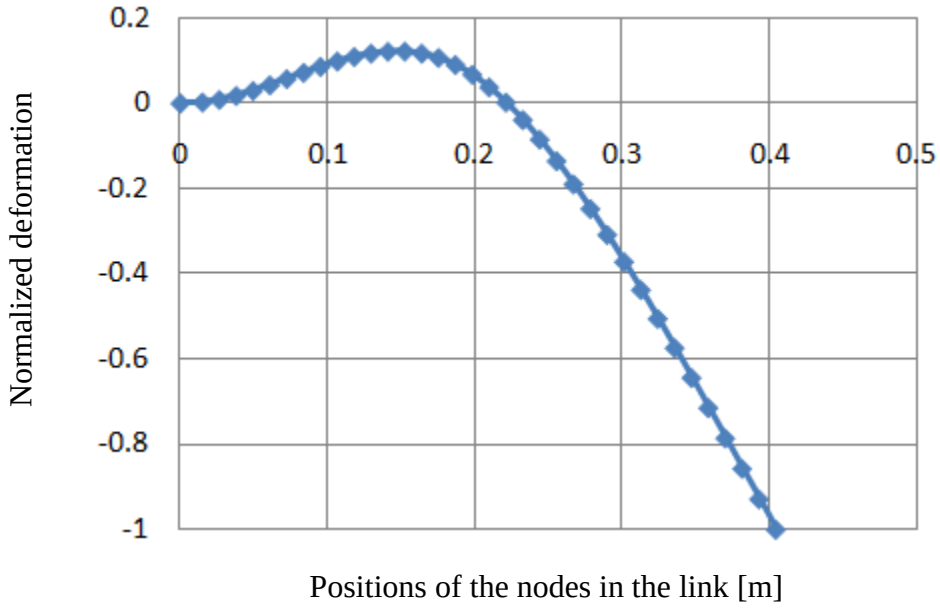

Fig. 4.19 Second vibration mode and natural frequency (f_2 = 8.92 Hz) of straight Model C2.1

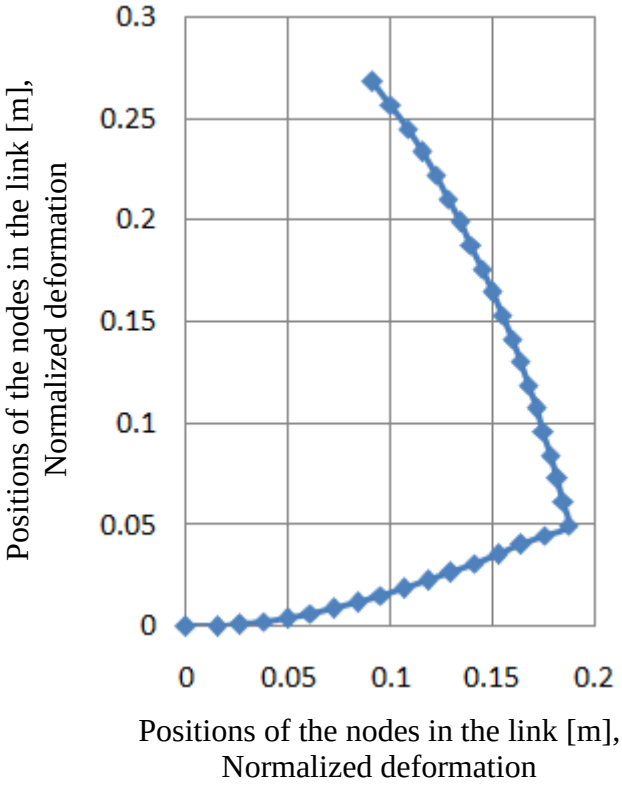

Fig. 4.20 First vibration mode and natural frequency (f_1 = 2.00 Hz) of elbow Model C2.1

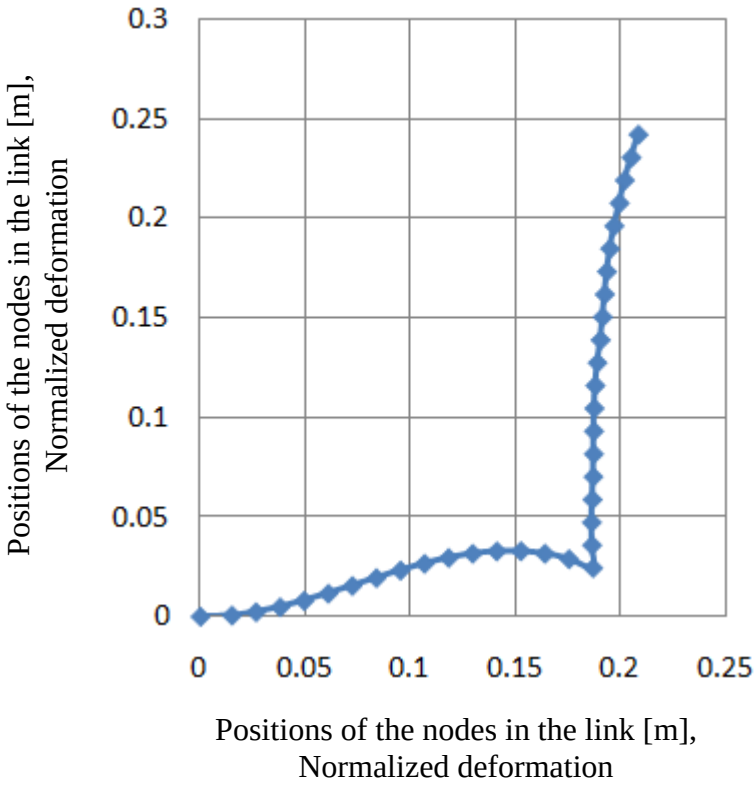

Fig. 4.21 Second vibration mode and natural frequency (f_2 = 9.97 Hz) of elbow Model C2.1

The rotation matrix of Element *i* used in the analysis for the elbow condition can be defined as follows

$$\boldsymbol{R}_i = \begin{bmatrix} \cos\theta & \sin\theta & 0 & 0 & 0 & 0 \\ -\sin\theta & \cos\theta & 0 & 0 & 0 & 0 \\ 0 & 0 & 1 & 0 & 0 & 0 \\ 0 & 0 & 0 & \cos\theta & \sin\theta & 0 \\ 0 & 0 & 0 & -\sin & \cos\theta & 0 \\ 0 & 0 & 0 & 0 & 0 & 1 \end{bmatrix}. \tag{4.72}$$

4.5.4 Time History Responses due to Base Excitation

Another calculation was done to find time history responses of strains for the flexible two-link manipulator due to the base excitation generated by rotation of the first motor. Computational codes on time history response of strains using Model C2.1 were developed based on the formulation explained in Sub-Chapter 4.2. In the calculation, the first motor was rotated by the angle of $\pi/2$ radians (90 degrees) within 0.5 second.

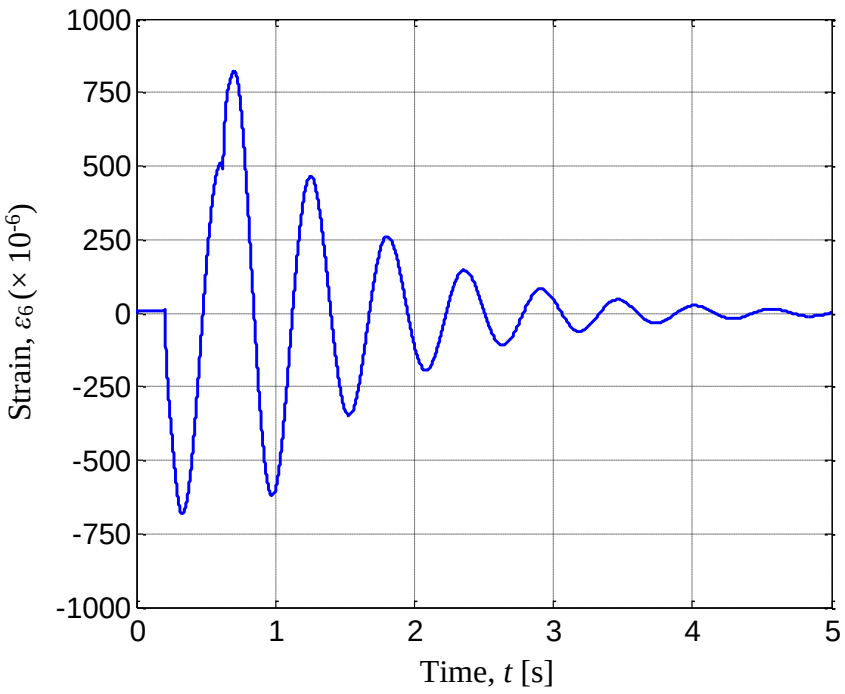

Fig. 4.22 Calculated time history response of strains due to base excitation at Node 6 of Model C2.1

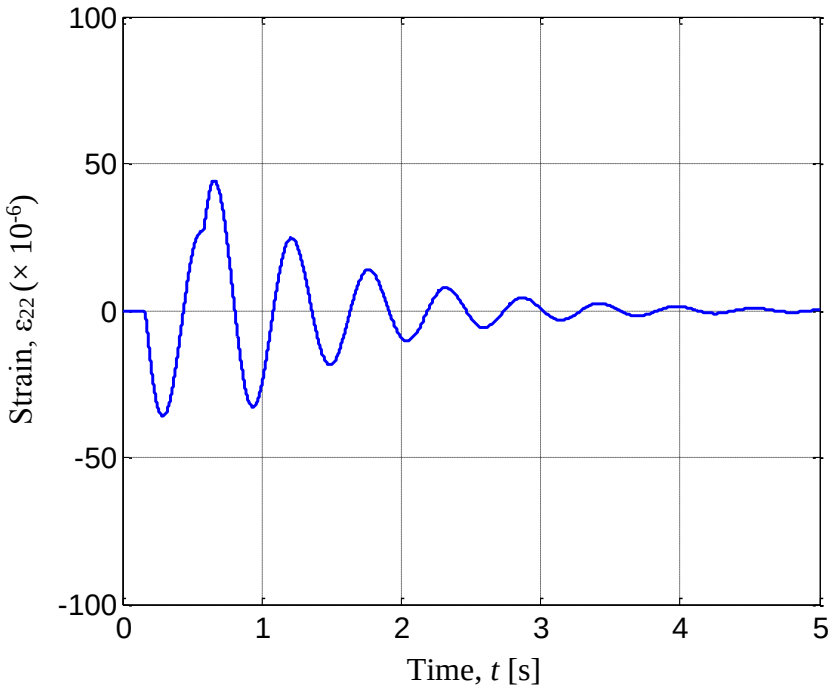

Fig. 4.23 Calculated time history response of strains due to base excitation at Node 22 of Model C2.1

Figures 4.22 and 4.23 show the calculated time history responses of strains at Node 6 and Node 22 of Model C2.1 under the base excitation due to rotation of the first motor.

4.5.5 Time History Responses on Uncontrolled and Controlled System for Model C2.2

Time history responses of strains on the uncontrolled and controlled Model C2.2 were calculated when the first and second motors rotated by the angle of $\pi/4$ radian (45 degrees) and $\pi/2$ radians (90 degrees) within 0.50 [s], respectively. Time history responses of strains on the controlled system were calculated for Model C2.2 under three control strategies shown in Figs. 4.10, 4.11 and 4.12.

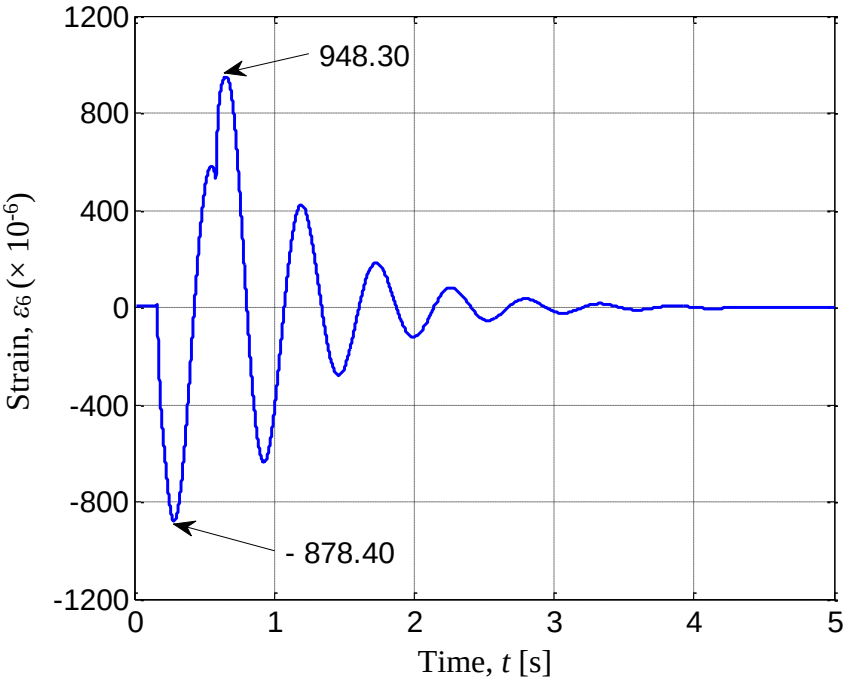

Fig. 4.24 Calculated time history response of strains at Node 6 for uncontrolled Model C2.2 due to base excitation

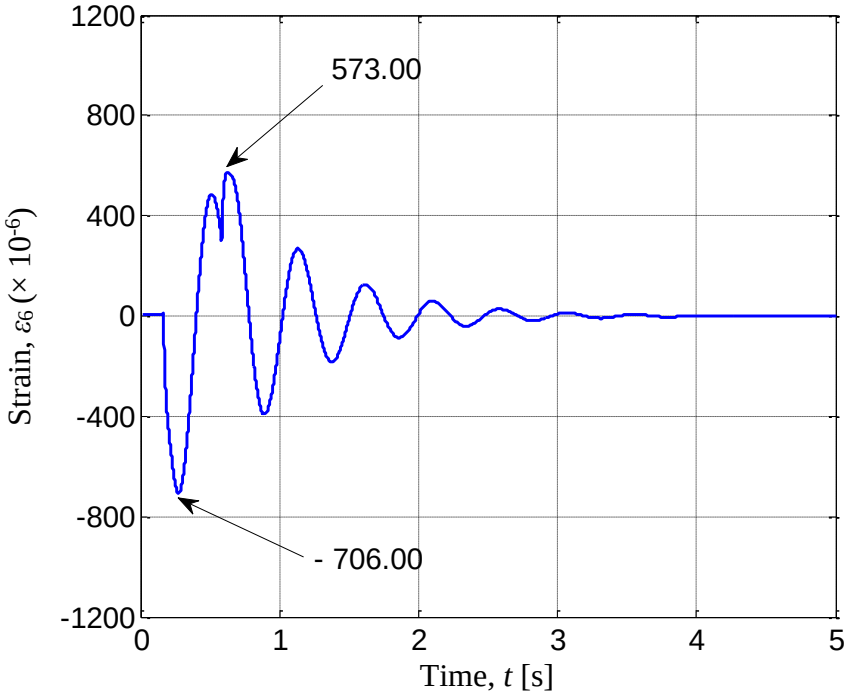

Fig. 4.25 Calculated time history response of strains at Node 6 for controlled Model C2.2 due to base excitation using P-controller (K_p = 2 [Nm])

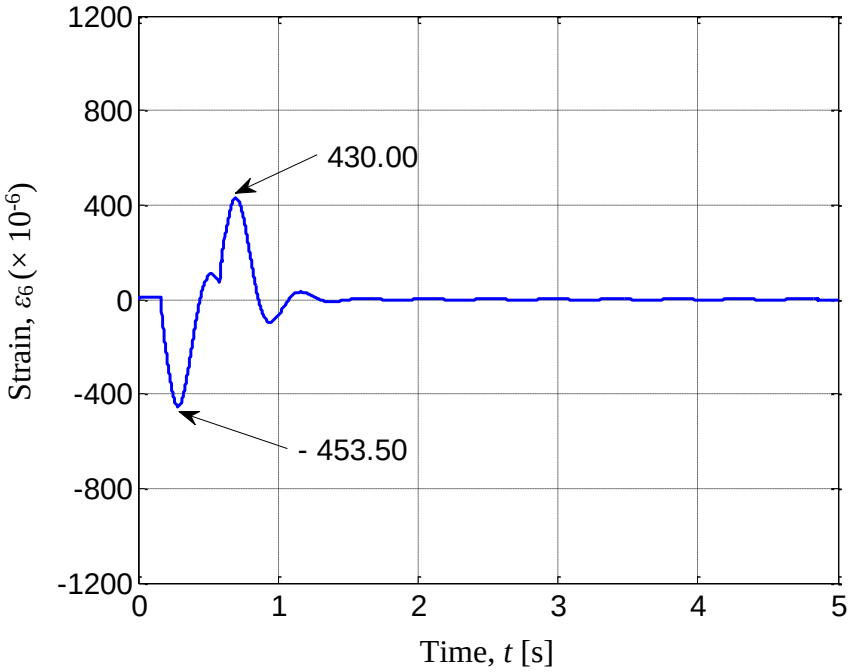

Fig. 4.26 Calculated time history response of strains at Node 6 for controlled Model C2.2 due to base excitation using PD-controller (K_p = 2 [Nm], K_d = 0.6 [Nm])

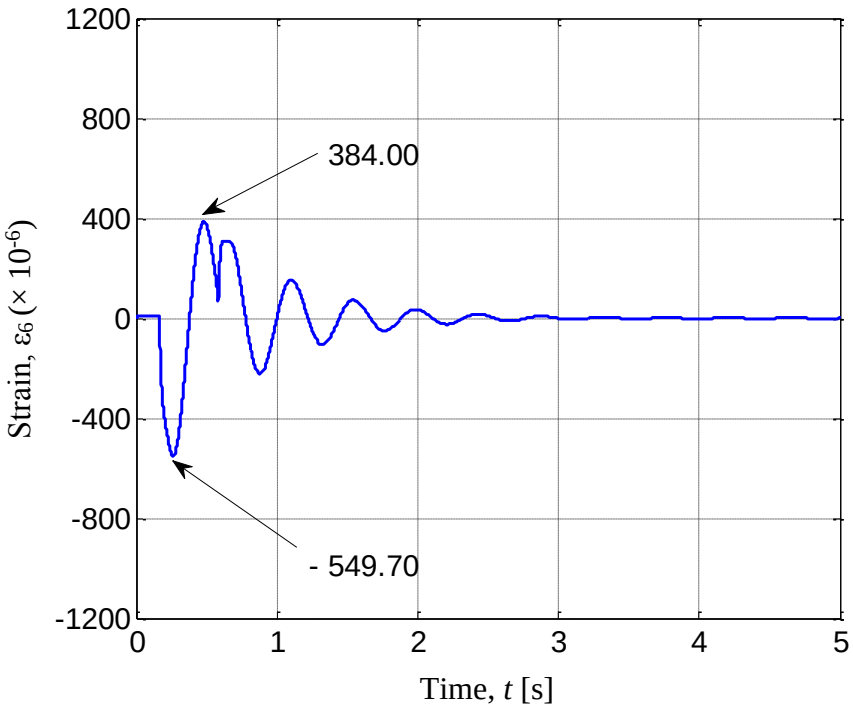

Fig. 4.27 Calculated time history response of strains at Node 6 for controlled Model C2.2 due to base excitation using AF-controller (K_{pa} = 0.02 [-])

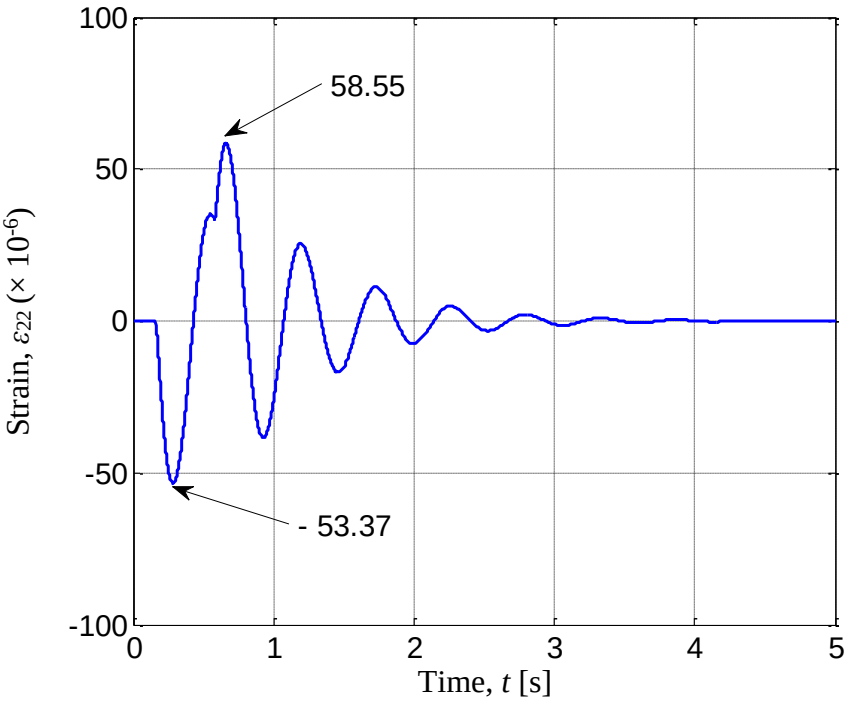

Fig. 4.28 Calculated time history response of strains at Node 22 for uncontrolled Model C2.2 due to base excitation

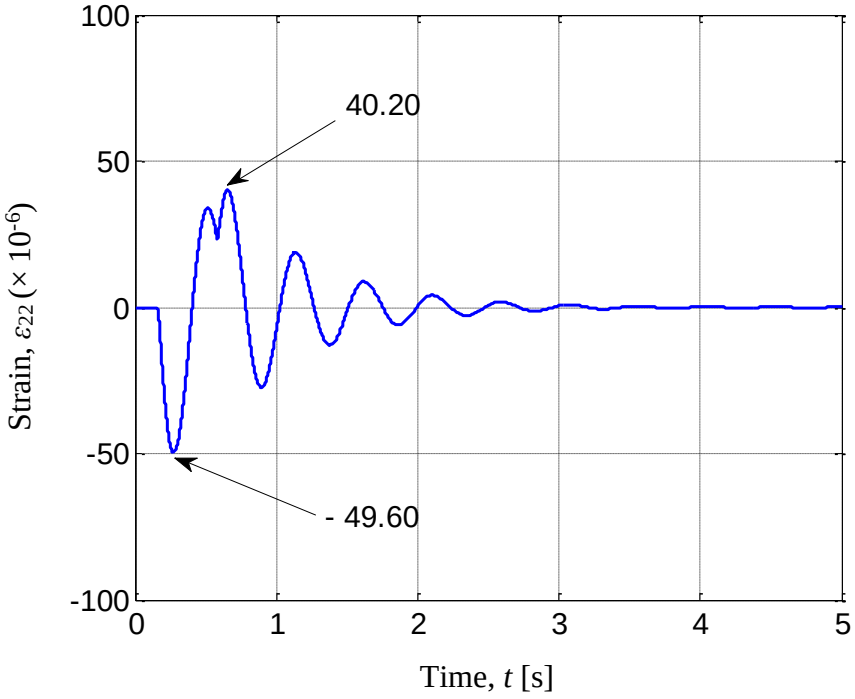

Fig. 4.29 Calculated time history response of strains at Node 22 for controlled Model C2.2 due to base excitation using P-controller (K_p = 2 [Nm])

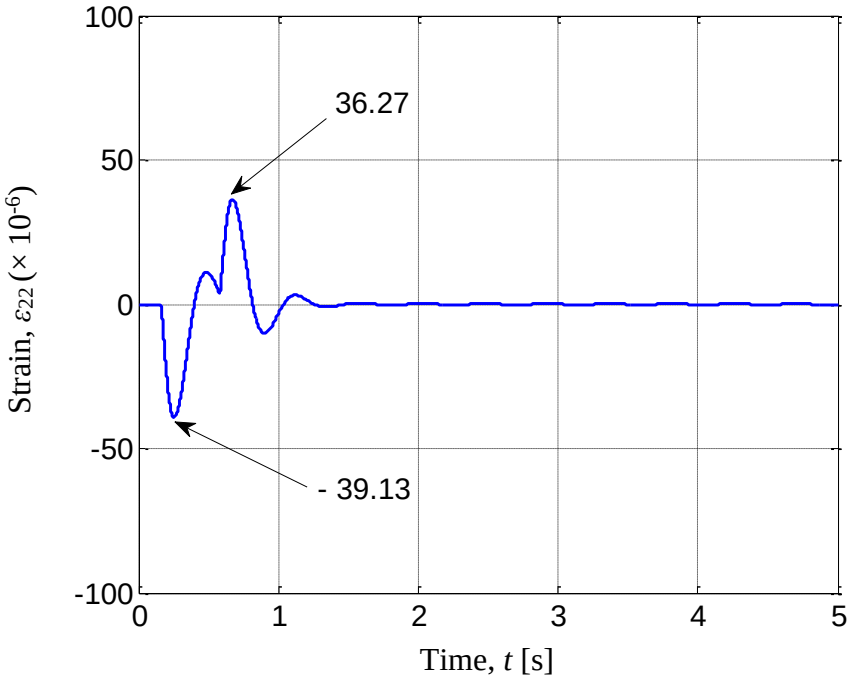

Fig. 4.30 Calculated time history response of strains at Node 22 for controlled Model C2.2 due to base excitation using PD-controller (K_p = 2 [Nm], K_d = 0.6 [Nm])

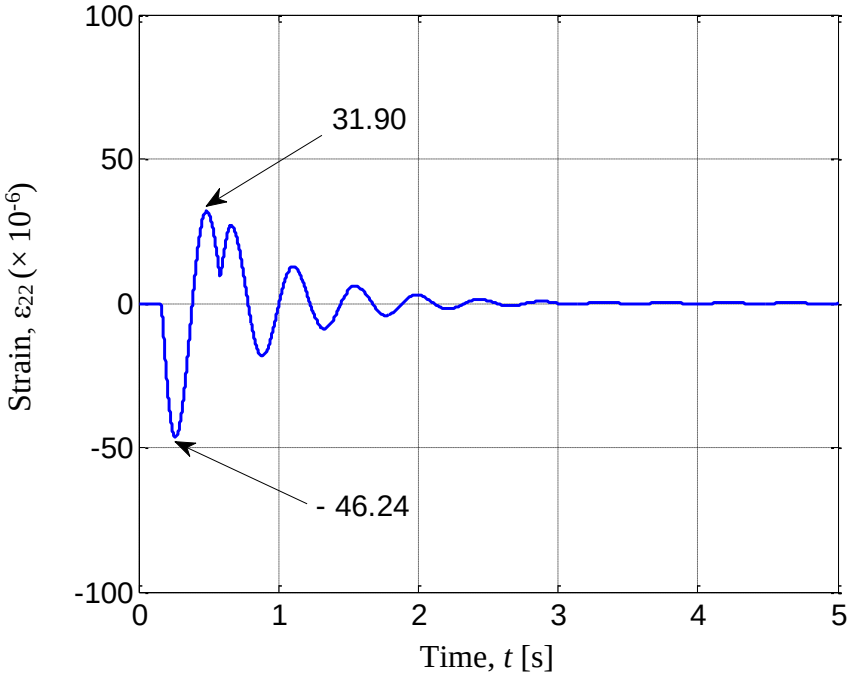

Fig. 4.31 Calculated time history response of strains at Node 22 for controlled Model C2.2 due to base excitation using AF-controller (K_{pa} = 0.02 [-])

Examining several gains of the P, PD and AF controllers leaded to K_p = 2 [Nm], K_d = 0.6 [Nms] and K_{pa} = 0.02 [-] as the better ones. Figures 4.24 to 4.27 show the calculated time history responses of strains at Node 6 for uncontrolled and controlled Model C2.2. The maximum and minimum strains of uncontrolled system at Node 6 in positive and negative sides were 948.30×10^{-6} and -878.40×10^{-6}, as shown in Fig. 4.24. By using P-controller they became 573.00×10^{-6} and -706.00×10^{-6}, as shown in Fig. 4.25. By adding D-gain they became 430.00×10^{-6} and -453.50×10^{-6}, as shown in Fig. 4.26. Moreover, by using AF-controller they became 384.00×10^{-6} and -549.70×10^{-6}, as shown in Fig. 4.27.

Then, Figs 4.28 to 4.31 show the calculated time history responses of strains at Node 22 for uncontrolled and controlled Model C2.2. The maximum and minimum strains of uncontrolled system at Node 22 in positive side and negative side were 58.55×10^{-6} and -53.37×10^{-6}, as shown in Fig. 4.28. By using P-controller they became 40.20×10^{-6} and -49.60×10^{-6}, as shown in Fig. 4.29. By adding D-gain they became 36.27×10^{-6} and -39.13×10^{-6}, as shown in Fig. 4.30. Moreover, by using AF-controller they became 31.90×10^{-6} and -46.24×10^{-6}, as shown in Fig. 4.31.

4.5.6 Time History Responses on Uncontrolled and Controlled System for Model C2.3

Time history responses of strains on the uncontrolled and controlled Model C2.3 were calculated when the first and second motors rotated by the angle of $\pi/4$ radian (45 degrees) and $\pi/2$ radians (90 degrees) within 0.50 [s], respectively. Time history responses of strains on the controlled system were calculated for Model C2.3 under three control strategies shown in Figs. 4.13, 4.14 and 4.15.

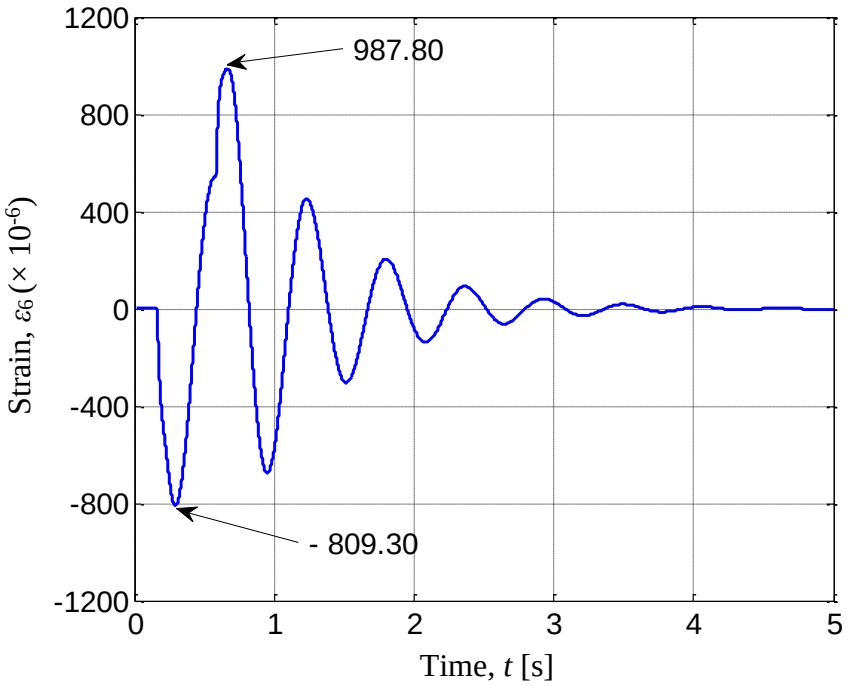

Fig. 4.32 Calculated time history response of strains at Node 6 for uncontrolled Model C2.3 due to base excitation

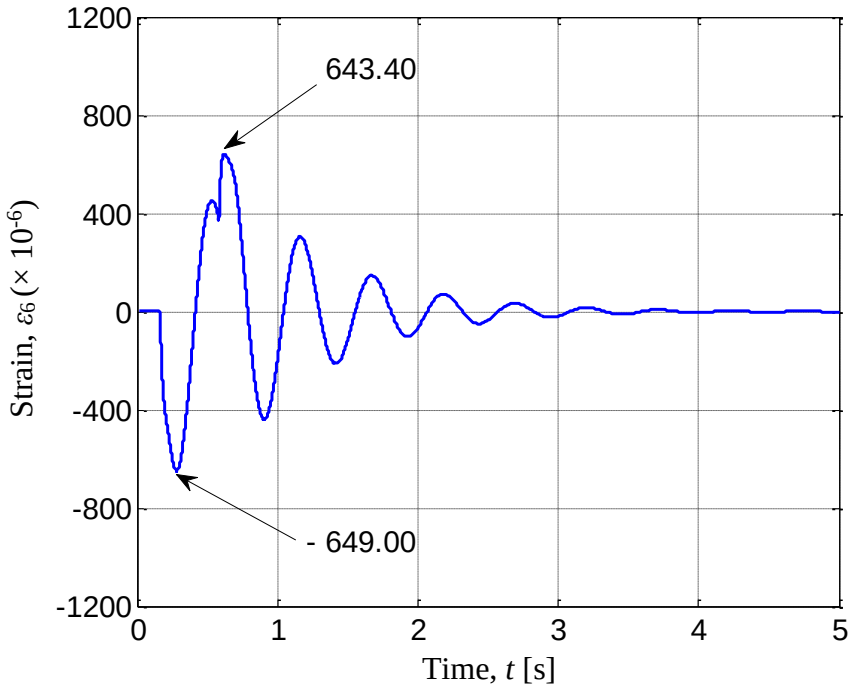

Fig. 4.33 Calculated time history response of strains at Node 6 for controlled Model C2.3 due to base excitation using P-controllers (K_{p1} = 2 [Nm], K_{p2} = 40 [Nm])

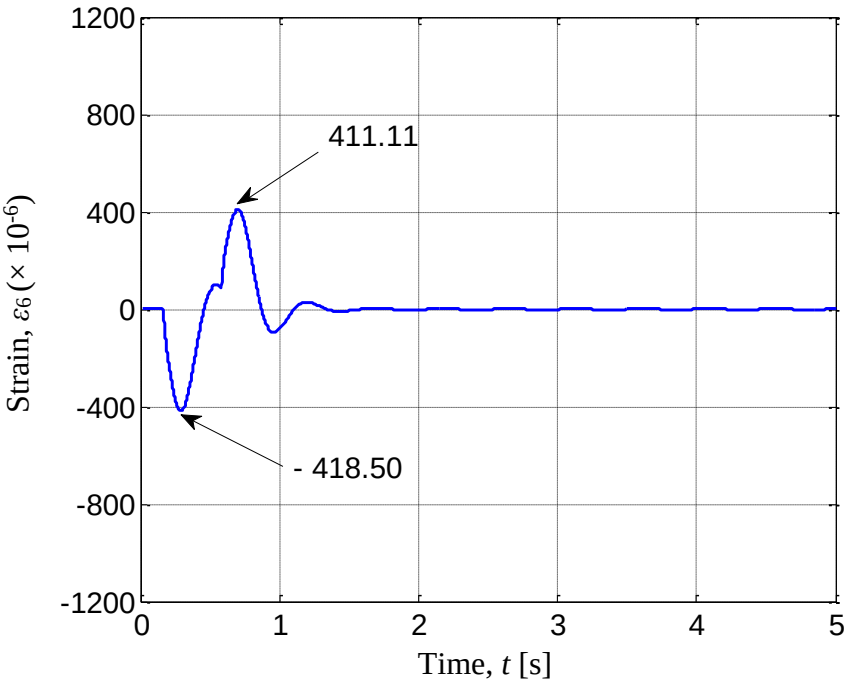

Fig. 4.34 Calculated time history response of strains at Node 6 for controlled Model C2.3 due to base excitation using PD-controllers (K_{p1} = 2 [Nm], K_{d1} = 0.6 [Nm], K_{p2} = 40 [Nm], K_{d2} = 10 [Nm])

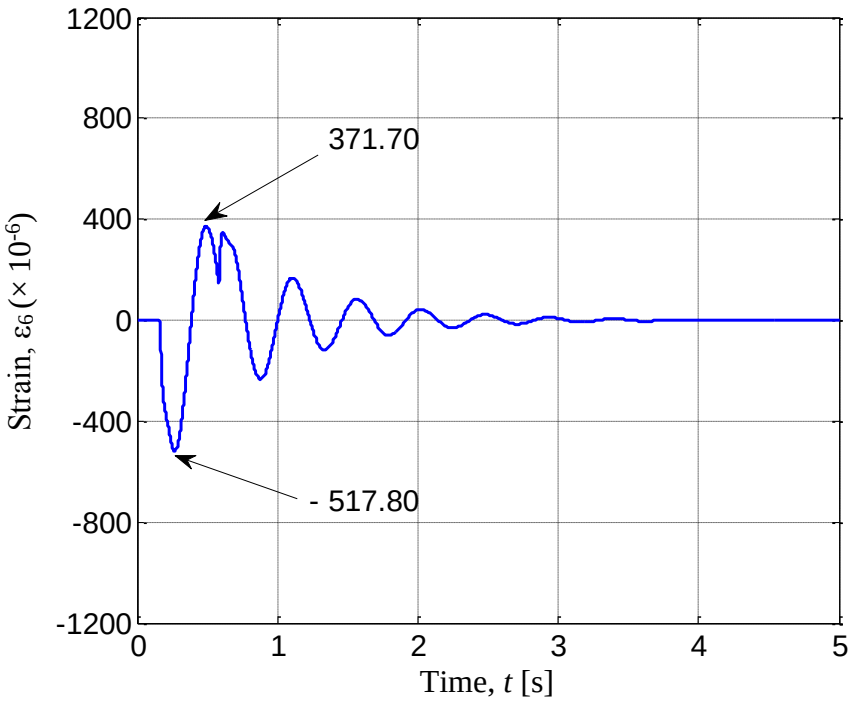

Fig. 4.35 Calculated time history response of strains at Node 6 for controlled Model C2.3 due to base excitation using AF-controllers (K_{pa1} = 0.02 [-], K_{pa2} = 0.5 [-])

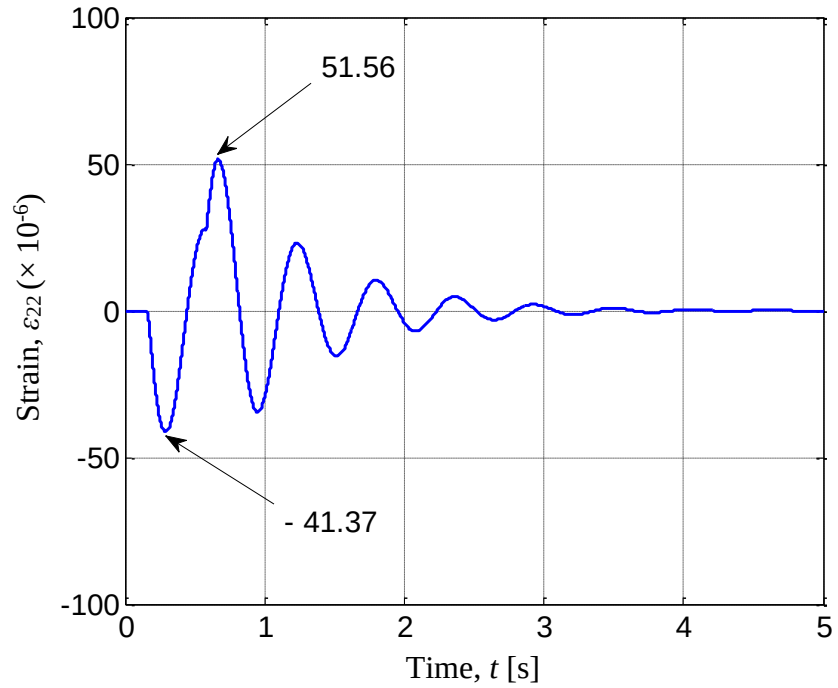

Fig. 4.36 Calculated time history response of strains at Node 22 for uncontrolled Model C2.3 due to base excitation

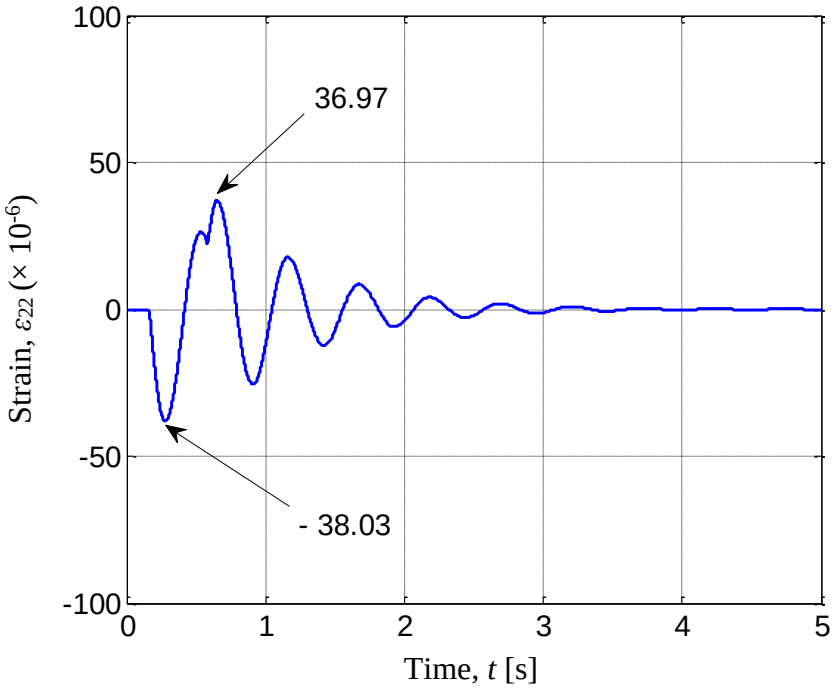

Fig. 4.37 Calculated time history response of strains at Node 22 for controlled Model C2.3 due to base excitation using P-controllers (K_{p1} = 2 [Nm], K_{p2} = 40 [Nm])

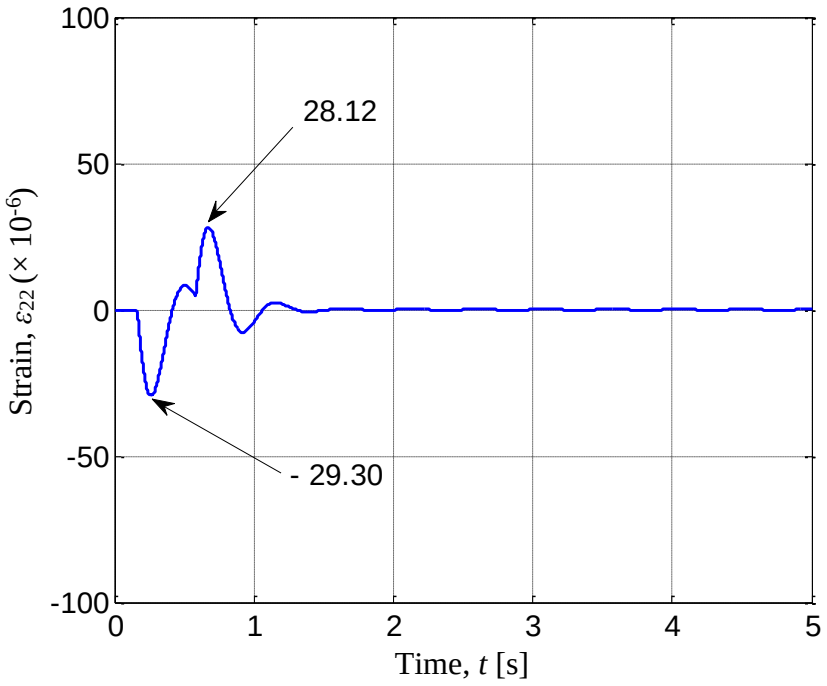

Fig. 4.38 Calculated time history response of strains at Node 22 for controlled Model C2.3 due to base excitation using PD-controllers (K_{p1} = 2 [Nm], K_{d1} = 0.6 [Nm], K_{p2} = 40 [Nm], K_{d2} = 10 [Nm])

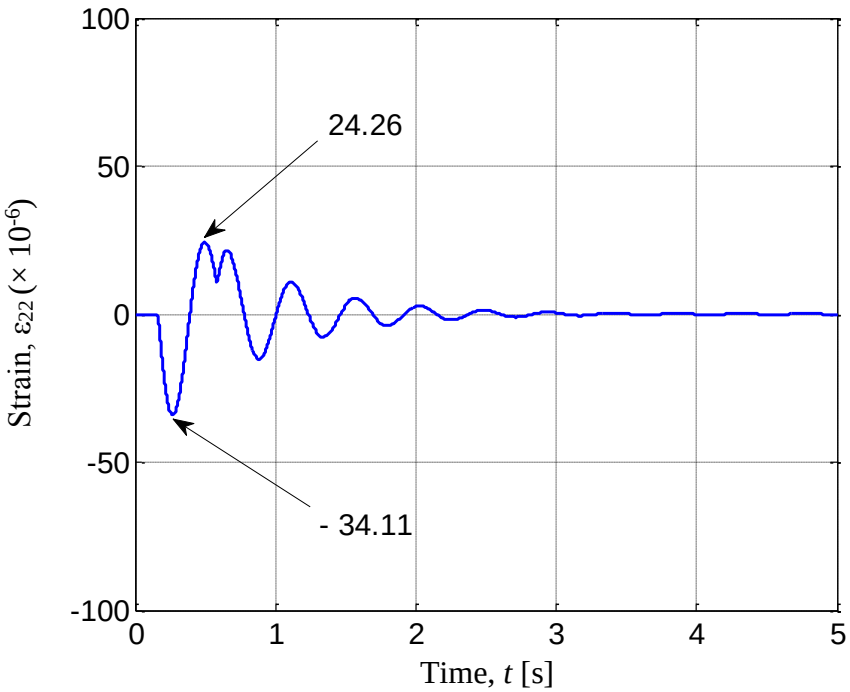

Fig. 4.39 Calculated time history response of strains at Node 22 for controlled Model C2.3 due to base excitation using AF-controllers (K_{pa1} = 0.02 [-], K_{pa2} = 0.5 [-])

Examining several gains of the P, PD and AF controllers leaded to K_{p1} = 2 [Nm], K_{d1} = 0.6 [Nms], K_{p2} = 40 [Nm], K_{d2} = 10 [Nms], K_{pa1} = 0.02 [-] and K_{pa2} = 0.5 [-] as the better ones. Figures 4.32 to 4.35 show the calculated time history responses of strains at Node 6 for uncontrolled and controlled Model C3.2. The maximum and minimum strains of uncontrolled system at Node 6 in positive side and negative side were 987.80×10^{-6} and -809.30×10^{-6}, as shown in Fig. 4.32. By using P-controllers they became 643.40×10^{-6} and -649.00×10^{-6}, as shown in Fig. 4.33. By adding D-gains they became 411.11×10^{-6} and -418.50×10^{-6}, as shown in Fig. 4.34. Moreover, by using AF-controllers they became 371.70×10^{-6} and -517.80×10^{-6}, as shown in Fig. 4.35.

Then, Figs. 4.36 to 4.39 show the calculated time history responses of strains at Node 22 for uncontrolled and controlled Model C2.3. The maximum and minimum strains of uncontrolled system at Node 22 in positive side and negative side were 51.56×10^{-6} and -41.37×10^{-6}, as shown in Fig. 4.36. By using P-controllers they became 36.97×10^{-6} and -38.03×10^{-6}, as shown in Fig. 4.37. By adding D-gains they became 28.12×10^{-6} and -29.30×10^{-6}, as shown in Fig. 4.38. Moreover, by using AF-controllers they became 24.26×10^{-6} and -34.11×10^{-6}, as shown in Fig. 4.39.

4.5.7 Time History Responses on Uncontrolled and Controlled System for Model C2.4

Time history responses of strains on the uncontrolled and controlled Model C2.4 were calculated when the first and second motors rotated by the angle of $\pi/4$ radian (45 degrees) and $\pi/2$ radians (90 degrees) within 0.50 [s], respectively. Time history responses of strains on the controlled system were calculated for Model C2.4 under three control strategies shown in Figs. 4.10, 4.11 and 4.12.

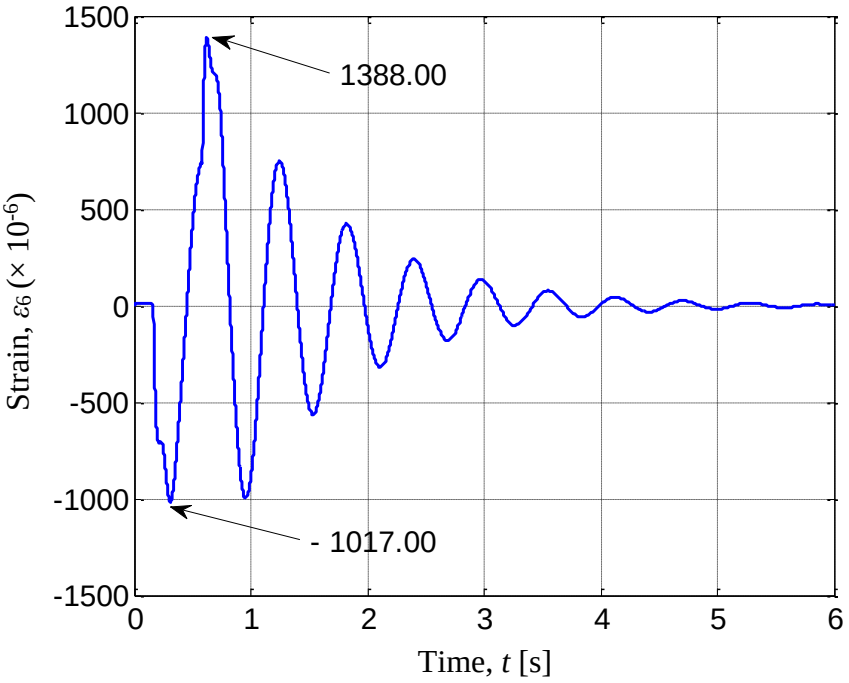

Fig. 4.40 Calculated time history response of strains at Node 6 for uncontrolled Model C2.4 due to base excitation

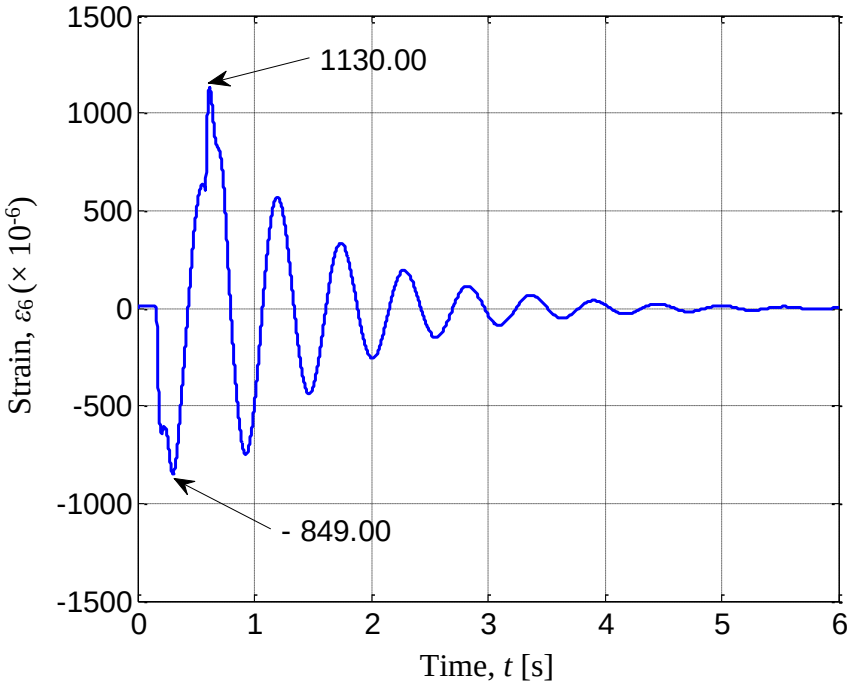

Fig. 4.41 Calculated time history response of strains at Node 6 for Controlled Model C2.4 due to base excitation using P-controller (K_p = 2 [Nm])

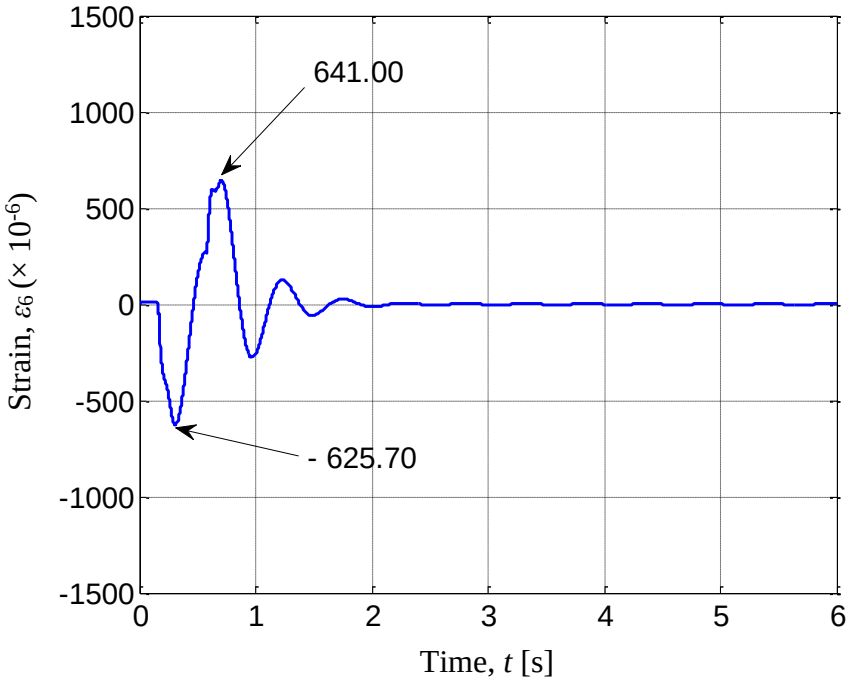

Fig. 4.42 Calculated time history response of strains at Node 6 for Controlled Model C2.4 due to base excitation using PD-controller (K_p = 2 [Nm], K_d = 0.6 [Nm])

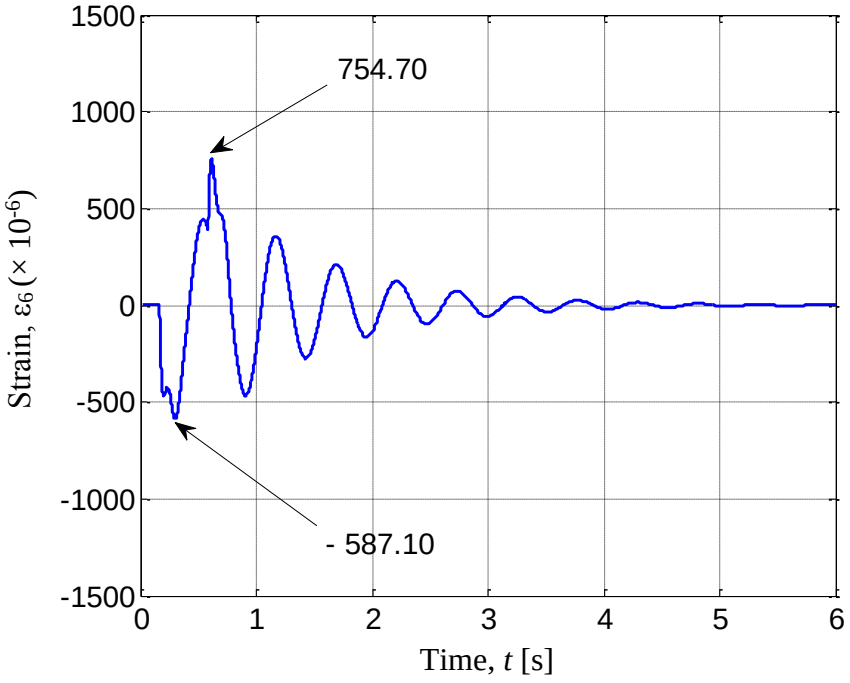

Fig. 4.43 Calculated time history response of strains at Node 6 for Controlled Model C2.4 due to base excitation using AF-controller (K_{pa} = 0.02 [-])

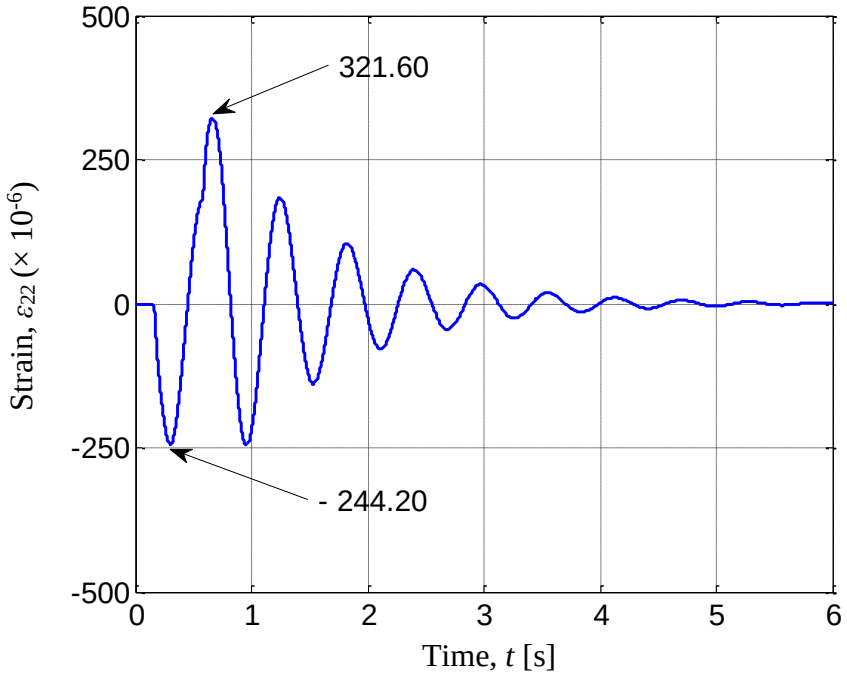

Fig. 4.44 Calculated time history response of strains at Node 22 for uncontrolled Model C2.4 due to base excitation

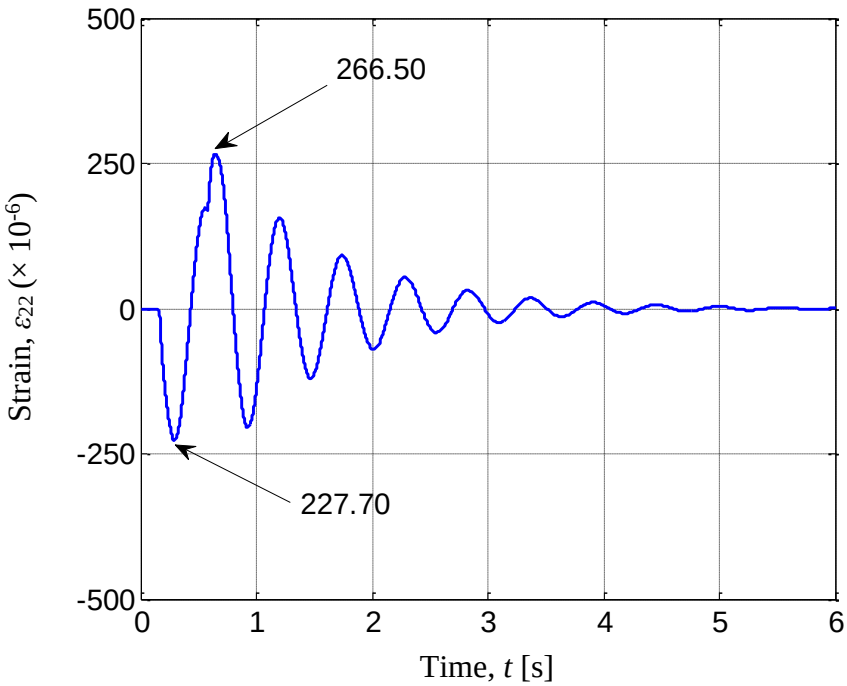

Fig. 4.45 Calculated time history response of strains at Node 22 for Controlled Model C2.4 due to base excitation using P-controller (K_p = 2 [Nm])

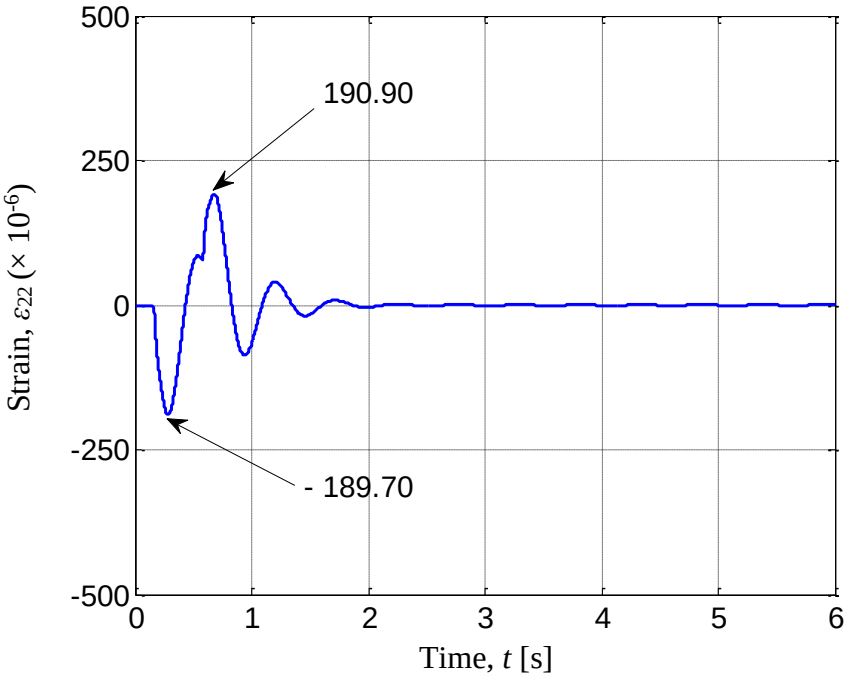

Fig. 4.46 Calculated time history response of strains at Node 22 for Controlled Model C2.4 due to base excitation using PD-controller (K_p = 2 [Nm], K_d = 0.6 [Nm])

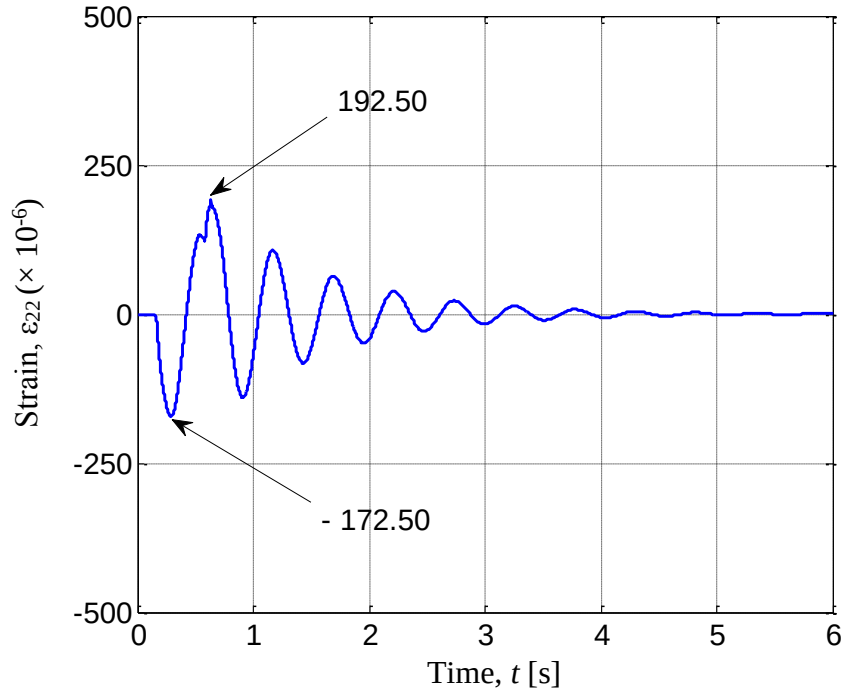

Fig. 4.47 Calculated time history response of strains at Node 22 for Controlled Model C2.4 due to base excitation using AF-controller (K_{pa} = 0.02 [-])

Examining several gains of the P, PD and AF controllers leaded to K_p = 2 [Nm], K_d = 0.6 [Nms] and K_{pa} = 0.02 [-] as the better ones. Figures 4.40 to 4.43 show the calculated time history responses of strains at Node 6 for uncontrolled and controlled Model C2.4. The maximum and minimum strains of uncontrolled system at Node 6 in positive and negative sides were 1388.30×10^{-6} and -1017.00×10^{-6}, as shown in Fig. 4.40. By using P-controller they became 1130.00×10^{-6} and -849.00×10^{-6}, as shown in Fig. 4.41. By adding D-gain they became 641.00×10^{-6} and -625.70×10^{-6}, as shown in Fig. 4.42.Moreover, by using AF-controller they became 754.70×10^{-6} and -587.10×10^{-6}, as shown in Fig. 4.43.

Then, Figs. 4.44 to 4.47 show the calculated time history responses of strains at Node 22 for uncontrolled and controlled Model C2.4. The maximum and minimum strains of uncontrolled system at Node 22 in positive side and negative side were 321.60×10^{-6} and -244.20×10^{-6}, as shown in Fig. 4.44. By using P-controller they became 266.50×10^{-6} and -227.70×10^{-6}, as shown in Fig. 4.45. By adding D-gain they became 190.90×10^{-6} and -189.70×10^{-6}, as shown in Fig. 4.46. Moreover, by using AF-controller they became 192.50×10^{-6} and -172.10×10^{-6}, as shown in Fig. 4.47.

4.6 Conclusions

The equations of motion for the flexible two-link manipulator had been derived using the finite element method. Computational codes had been developed in order to perform dynamic simulations of the system. Calculated results on time history responses, natural frequencies and vibration modes have been presented. The proportional (P), proportional-derivative (PD) and active-force (AF) controls strategies were designed to suppress the vibration of the system. Their performances were compared through the

calculations. Based on the calculated results, the effect of the second piezoelectric actuator was small and not significant compare to the first one. Therefore, using one piezoelectric actuator will be sufficient for experiment. The calculated results have revealed that the proposed control scheme can effectively suppress the vibration of the flexible two-link manipulator even though using only one piezoelectric actuator as well as the effectiveness of the proposed PD-control compared to the P and AF ones to suppress the vibration of the system.

Chapter 5

Experiments on Vibration Control of a Flexible Two-link Manipulator Using a Piezoelectric Actuator

5.1 Introduction

The purposes of study presented in this chapter are to validate the formulation, the computational codes and modeling of the two-link system presented in Chapter 4 through experiments and to investigate the validity of the proposed control scheme and strategies of the flexible two-link manipulator.

The flexible manipulator used in this study consists of two aluminum beams as flexible links, two aluminum clamp-parts, two servo motors to rotate the links, a piezoelectric actuator to control vibration and a base. Experiments on time history responses and FFT (Fast Fourier Transform) processing were carried out to present the dynamic behavior of the link. Furthermore, the P, PD and AF controls strategies were implemented to suppress the vibration of the system. They were carried out using the piezoelectric actuator. Finally, their performances were compared through the experiments.

5.2 Experimental Models

In this chapter, we developed and used two types of experimental models of the flexible two-link manipulator.

5.2.1 Model E1.1

A model of the flexible two-link with the clamp-parts and the servo motors was used as Model E2.1. Figure 5.1 shows Model E2.1. Link 1 and Link 2 are attached to the first and second motors through the clamp-parts. Link 1 and Link 2 are connected through the second motor. The first motor is mounted to the base. Two strain gages are bonded to the position of 0.11 [m] and 0.38 [m] from the origin of the two-link system. In the experiments, the motors were operated by an independent motion controller. Model E2.1 was used to validate the dynamic behavior of the link. In the experiments, the motors were operated by an independent motion controller.

5.2.2 Model E2.2

A model of the two-link manipulator, the clamp-parts, the servo motors and the piezoelectric actuator was defined as Model E2.2. Figure 5.2 shows Model E2.2. The piezoelectric actuator was bonded to a one-side surface on Link 1 of Model 1 in such a way as shown in Fig. 5.2. Figure 5.3 shows the piezoelectric actuator with its clamped mechanism. Model E2.2 was used to implement the control scheme and strategies designed in Chapter 4. In the experiments, the motors were operated by an independent motion controller.

5.2.3 Model E2.3

Figure 5.4 shows model E2.3 that an end-effector is considered for a two-link manipulator with a piezoelectric actuator. Model E2.3 is used to show that the proposed control scheme is also suitable for such system. The end-effector is presented by adding a mass to the end tip of Model E2.2. In the experiments, the motor was operated by an

independent motion controller. Physical parameters of the two-link models and the piezoelectric actuator are shown in Table 4.1.

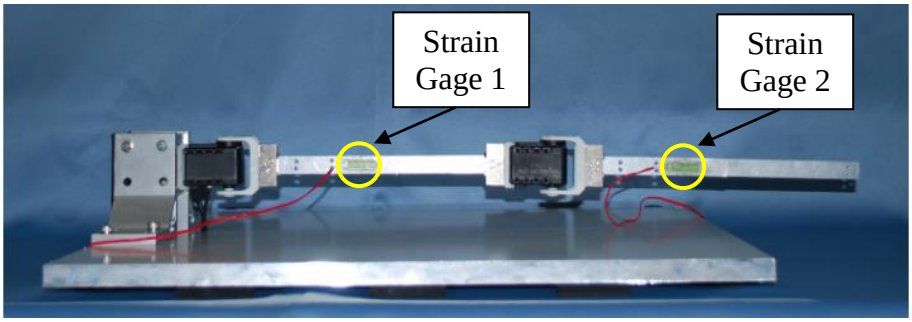

Fig.5.1 Model E2.1: Only flexible two-link

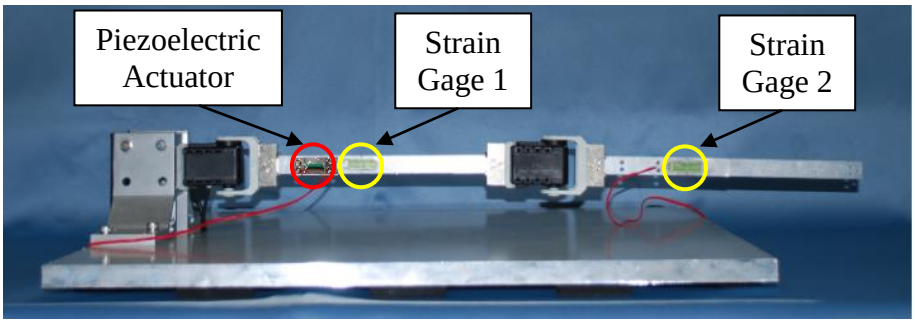

Fig.5.2 Model E2.2: Flexible two -link with a piezoelectric actuator

(a) Front view (b) Top view

Fig.5.3 Piezoelectric actuator with clamped mechanism

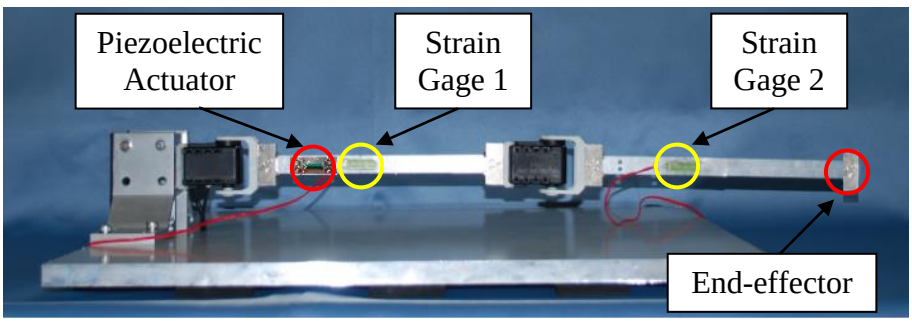

Fig.5.4 Model E2.3: Flexible two -link with a piezoelectric actuator and an end-effector

Table 4.1: Physical parameters of the flexible two-link and the piezoelectric actuators (previously shown in Page 71)

l : Total length	m	4.05×10^{-1}
l_1 : Length of Link 1	m	1.90×10^{-1}
l_2 : Length of Link 2	m	2.15×10^{-1}
l_{c1}, l_{c2} : Length of clamp-parts 1 and 2	m	1.50×10^{-2}
l_{a1}, l_{a2} : Length of Actuators 1 and 2	m	2.00×10^{-2}
S_{l1}, S_{l2} : Cross section area of links 1 and 2	m^2	1.95×10^{-5}
S_{c1}, S_{c2} : Cross section area of clamp-parts 1 and 2	m^2	8.09×10^{-4}
S_{a1}, S_{a2} : Cross section area of actuators 1 and 2	m^2	1.58×10^{-5}
I_{zl1}, I_{zl2} : Cross section area moment of inertia around z-axis of links 1 and 2	m^4	2.75×10^{-12}
I_{zc1}, I_{zc2} : Cross section area moment of inertia around z-axis of clamp-parts 1 and 2	m^4	3.06×10^{-8}
I_{za1}, I_{za2} : Cross section area moment of inertia around z-axis of actuators 1 and 2	m^4	1.61×10^{-11}
E_{l1}, E_{l2} : Young's Modulus of links 1 and 2	GPa	7.03×10^{1}
E_{c1}, E_{c2} : Young's Modulus of clamp-parts 1 and 2	GPa	7.03×10^{1}
E_{a1}, E_{a2} : Young's Modulus of actuators 1 and 2	GPa	4.40×10^{1}
ρ_{l1}, ρ_{l2} : Density of links 1 and 2	kg/m^3	2.68×10^{3}
ρ_{c1}, ρ_{c2} : Density of clamp-parts 1 and 2	kg/m^3	2.68×10^{3}
ρ_{a1}, ρ_{a2} : Density of actuators 1 and 2	kg/m^3	3.33×10^{3}
α_1, α_2 : Damping factor of links 1 and 2	s	2.51×10^{-4}
E_1, E_2 : Maximum input voltages of actuators 1 and 2	V	150.00
F_1, F_2 : Maximum output forces of actuators 1 and 2	N	200.00
m_2 : Mass of the second motor and it's clamping system	g	113.53

5.3 Control Scheme and Strategies

The control scheme used in the experiments was presented in previous chapter.

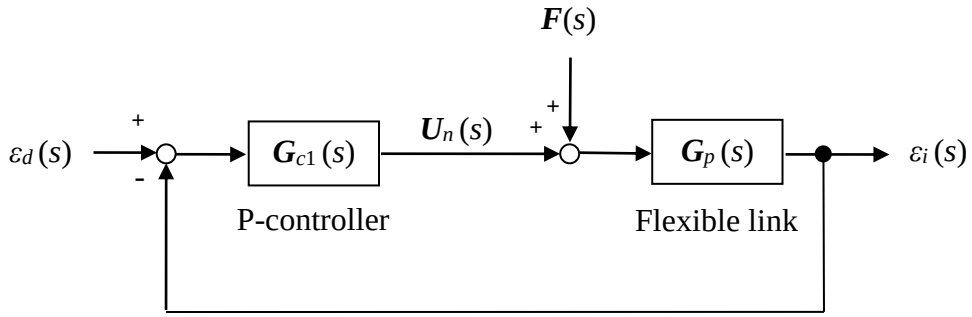

ε_d : Desired strain
$\boldsymbol{F}$: Base excitations
ε_i : Measured strains at Node i
$\boldsymbol{U}_n$: Applied bending moments

Fig. 4.10 Block diagram of proportional control of the flexible two-link manipulator (previously shown in Page 74)

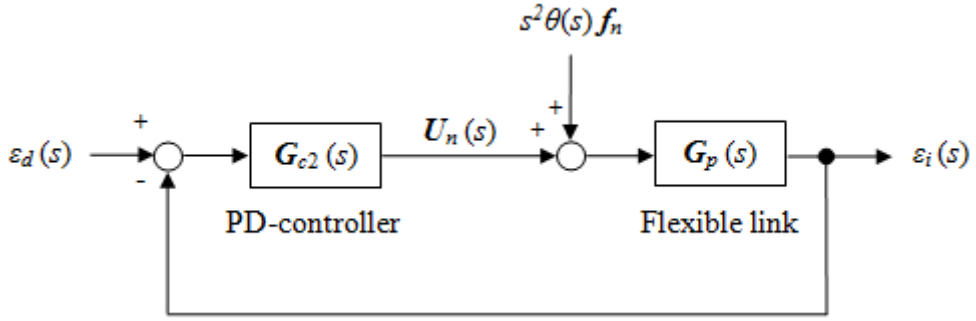

ε_d : Desired strain
$\boldsymbol{F}$: Base excitations
ε_i : Measured strains at Node i
$\boldsymbol{U}_n$: Applied bending moments

Fig. 4.11 Block diagram of proportional-derivative control of the flexible two-link manipulator (previously shown in Page 75)

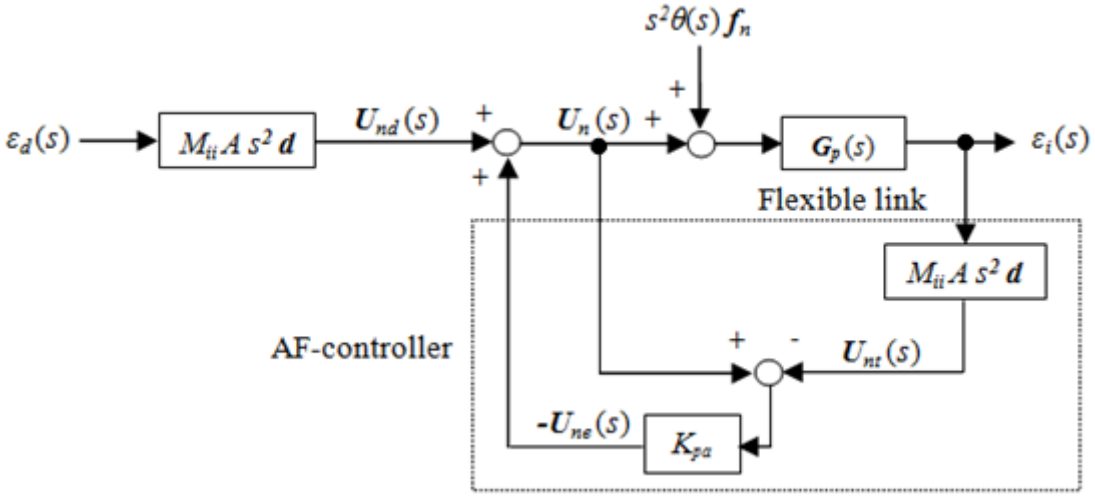

ε_d : Desired strain
θ_1 : Rotation angle of the first motor
A : Conversion from ε_i to v_i
$\boldsymbol{U}_{nd}$: Desired bending moments
$\boldsymbol{U}_{ne}$: Excitation bending moments
ε_i : Measured strains at Node i
M_{ii} : Component of mass matrix
$\boldsymbol{d}$: Position vector
$\boldsymbol{U}_n$: Applied bending moments
$\boldsymbol{U}_{nt}$: Bending moments

Fig. 4.12 Block diagram of active-force control of the flexible two-link manipulator (previously shown in Page 76)

As explained in Chapter 4, to drive the actuator, P, PD and AF control strategies will be implemented. Their performances were compared through the experiments. Figures 4.10 to 4.12 show the block diagrams of the P and AF control strategies.

5.4 Experimental Set-up

In order to investigate the validity of the proposed control strategies for the flexible two-link manipulator, an experimental set-up was designed. The schematic representation and experimental set-up are shown in Figs. 5.5 and 5.6. The flexible two-link manipulator consists of two aluminum beams as flexible links, two aluminum clamp-parts, two servo motors to rotate the links, a piezoelectric actuator to control vibration and a base. Two strain gages are bonded to the position of 0.11 [m] and 0.38 [m] from the origin of the two-link system. In the experiments, the motors were operated by an independent motion controller.

The piezoelectric actuator was attached on one side of the flexible link to provide the blocking force against vibrations. A Wheatstone bridge circuit was developed to measure the changes in resistance of the first strain gage in the form of voltages. An amplifier circuit was designed to amplify the small output signal of the Wheatstone bridge. A PCD-300A Wheatstone bridge - amplifier circuits were used for the second strain gage.

Furthermore, a data acquisition board and a computer that have functionality of A/D (analog to digital) conversion, signal processing, control process and D/A (digital to analog) conversion were used. The data acquisition board connected to the computer through USB port. Finally, the controlled signals sent to a piezo driver to drive the piezoelectric actuator in its voltage range.

All devices used in the experiments for the flexible two-link system have been presented in Chapter 3.

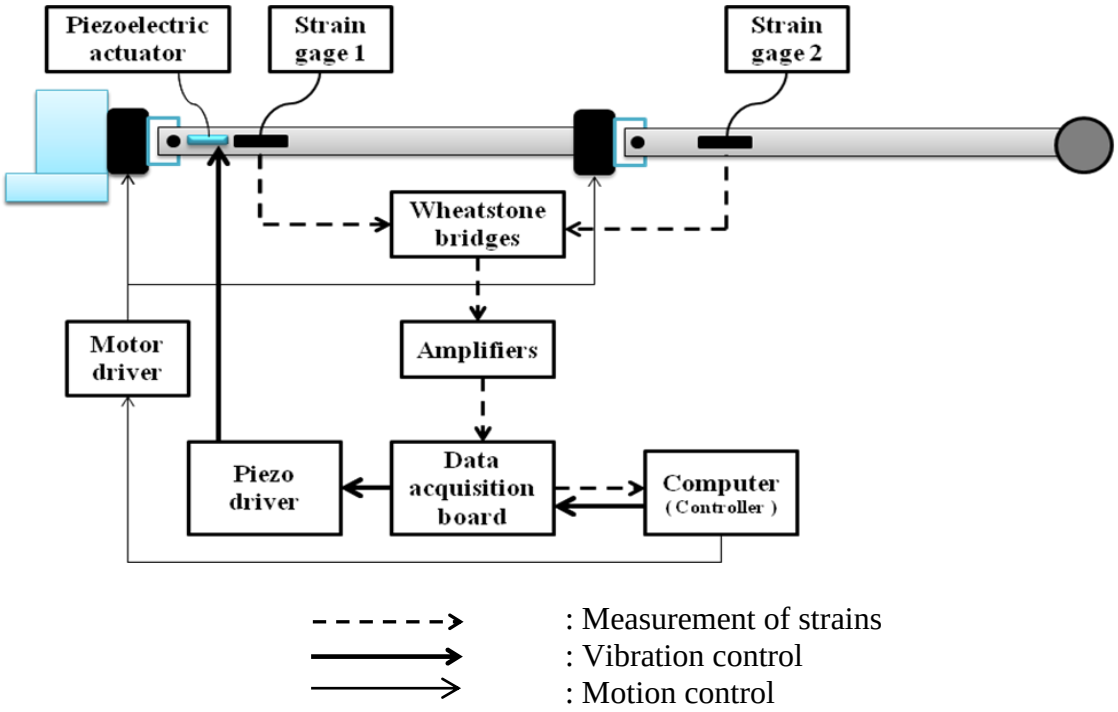

Fig.5.5 Schematics of measurement and control of the flexible two-link manipulator

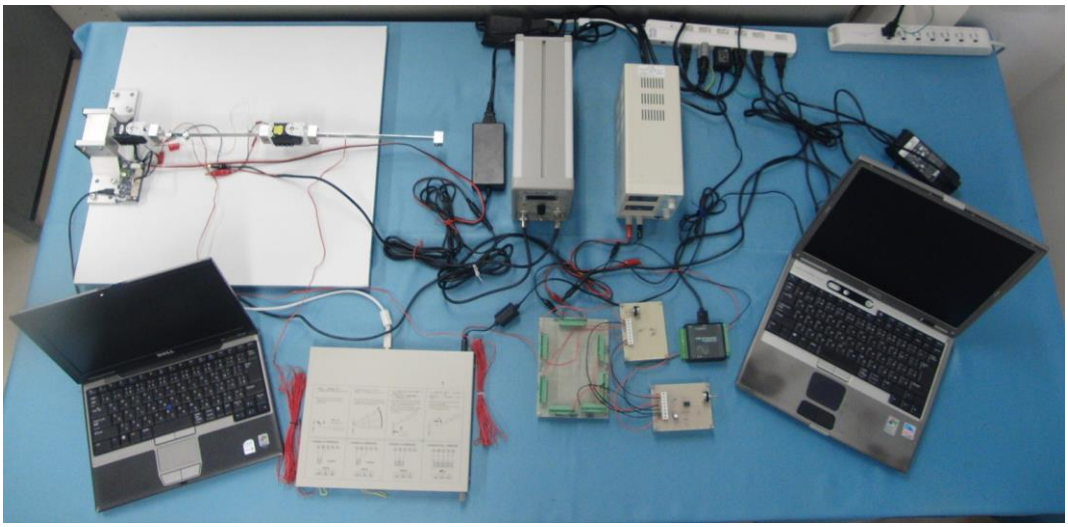

Fig.5.6 Experimental set-up of the flexible two-link manipulator

5.5 Experimental Method

The rotations of the first and second motors were set from 0 to $\pi/4$ radians (45 degrees) and to $\pi/2$ radians (90 degrees) within 0.50 [s], respectively. Outputs of the first strain gage were converted to voltages by the Wheatstone bridge and magnified by the amplifier. The noises that occur in the experiment were reduced by a 100 [μF] capacitor attached to the amplifier. The output voltages of the amplifier sent to the data acquisition board and the computer for control process. The control strategies were implemented in the computer using the visual C++ program. The analog output voltages of the data acquisition board sent to the input channel of the piezo driver to generate the actuated signals for the piezoelectric actuator.

5.6 Experimental Results and Validations of Computational Simulations

5.6.1 Time History Response on Free Vibration

An experiment on free vibration was carried out to measure time history response of strains for the flexible two-link manipulator using an impulse force as an external one. The experiment on free vibration was carried out using Model E2.1 at the same position in the calculation. Figure 5.7 shows the experimental time history response of strains under the impulse force at 0.11 [m] from the origin of the link.

Furthermore, as shown in Chapter 4, Fig. 4.16 shows the calculated time history response of strains at Node 6 of Model C2.1 under the impulse force. The results presented in Figs. 5.7 and 4.16 show the validity of the formulation and computational codes for time history response of strains on free vibration, and the modeling of the two-link system (Model C2.1).

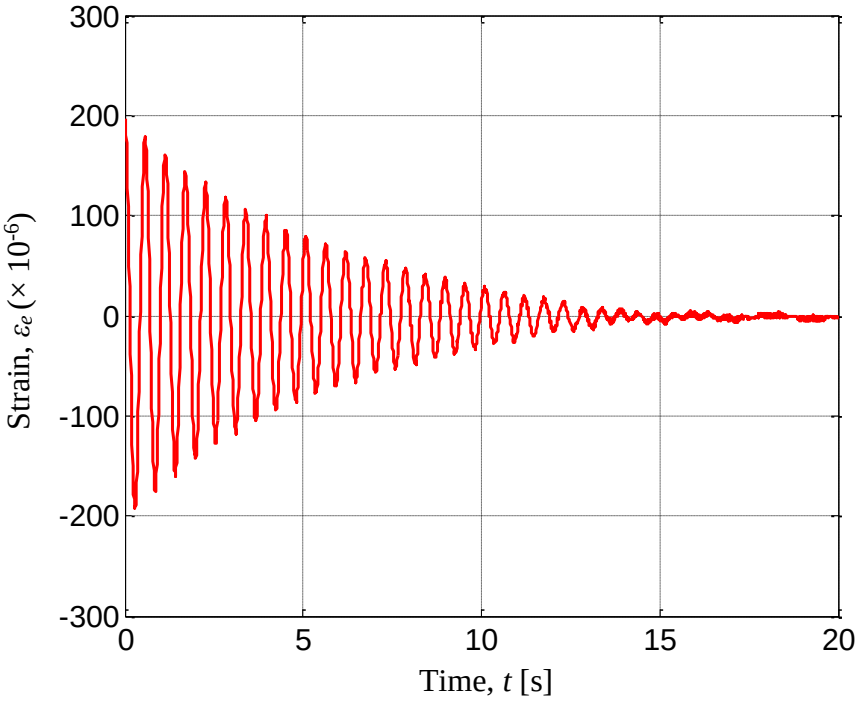

Fig. 5.7 Experimental time history response of strains on free vibration at 0.11 [m] from the origin of the two-link

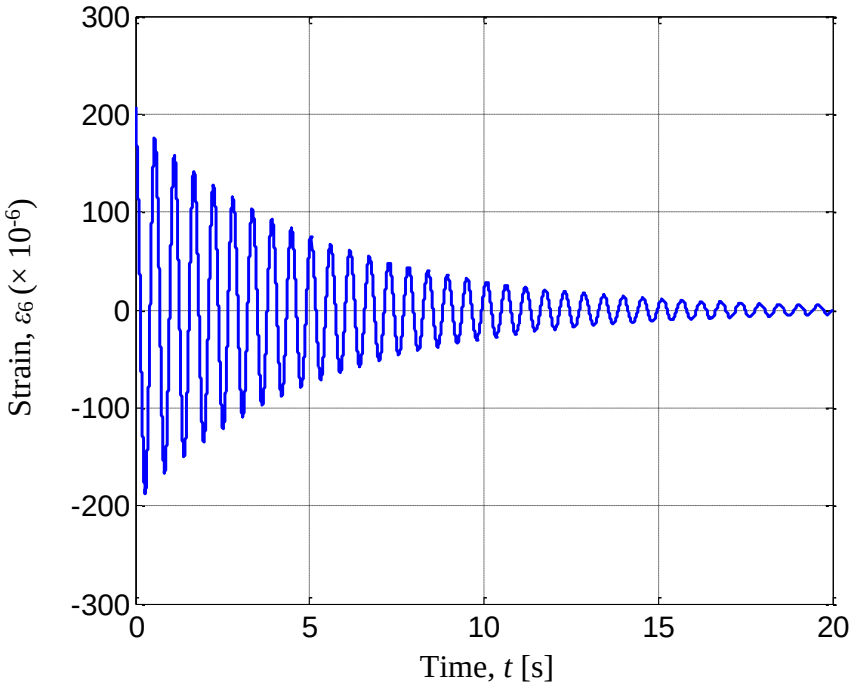

Fig. 4.16 Calculated time history response of strains on free vibration at Node 6 of Model C2.1 (previously shown in Page 82)

5.6.2 Fast Fourier Transform Processing

The experimental time history response of strains on free vibration of the flexible two-link (Model E2.1) was transferred by FFT processing to find its frequencies.

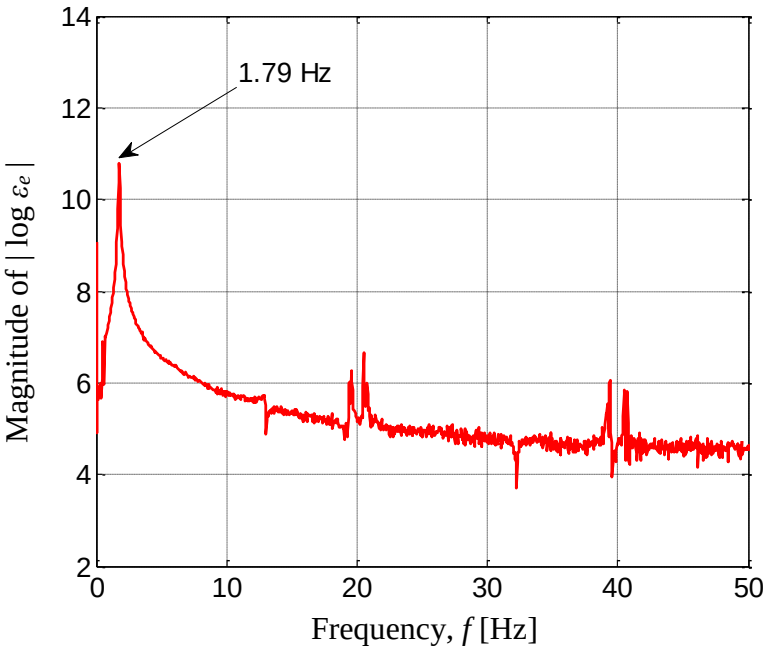

Fig. 5.8 Experimental natural frequency of the flexible two-link

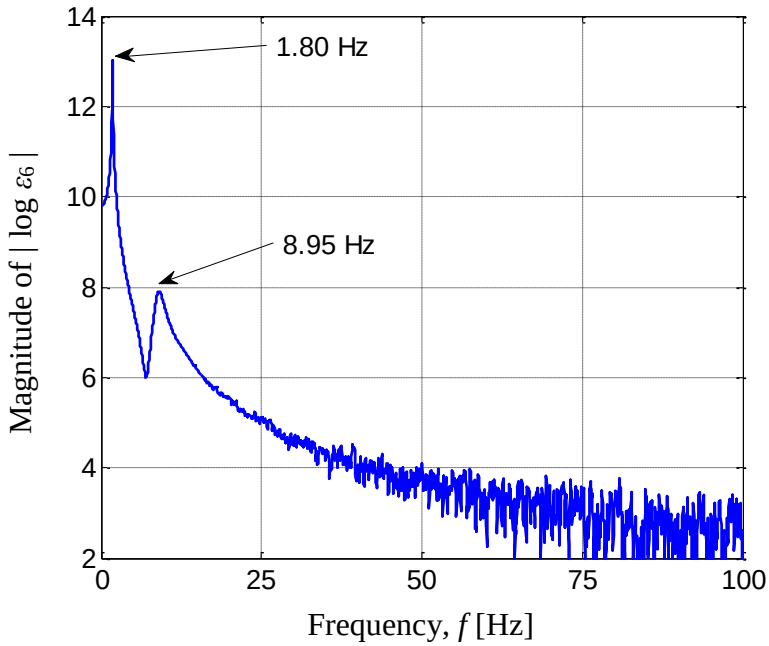

Fig. 4.17 Calculated time history response of strains on free vibration at Node 6 of Model C2.1 (previously shown in Page 83)

Figure 5.8 shows the experimental time history response of strains on the free vibration at the same position in the calculation (0.11 [m] from the origin of the two-link system). Furthermore, as shown in Chapter 4, Fig. 4.17 shows the calculated natural frequencies. The first experimental natural frequency, 1.79 [Hz] agreed with the calculated one, 1.80 [Hz]. The second natural frequency could not be measured. However, in the calculation it could be obtained as 8.95 [Hz]. The results presented in Figs. 5.8 and 4.17 show the validity of the formulation and computational codes for natural frequencies, and the modeling of the two-link system (Model C.21).

5.6.3 Time History Response due to Base Excitation

Another experiment was carried out to investigate time history responses of strains for the flexible two-link manipulator due to the base excitation generated by rotation of the motor. The experiment was carried out using Model E2.1 at the same position in the calculation. In the experiment, the first motor was rotated by the angle of $\pi/2$ radians (90 degrees) within 0.5 [s]. Figures 5.9 and 5.10 show the experimental time history responses of strains for the flexible two-link due to rotation of the first motor at 0.11 [m] and 0.38 [m] from the origin of the link, respectively.

Furthermore, as shown in Chapter 4, Figs. 4.22 and 4.23 shows the calculated time history responses of strains at Nodes 6 and 22 of Model C2.1 due to the base excitation, respectively. The results presented in Figs. 5.9, 5.10, 4.22 and 4.23 show the validity of the formulation and computational codes for time history response of strains due to the base excitation, and the modeling of the two-link system (Model C.21).

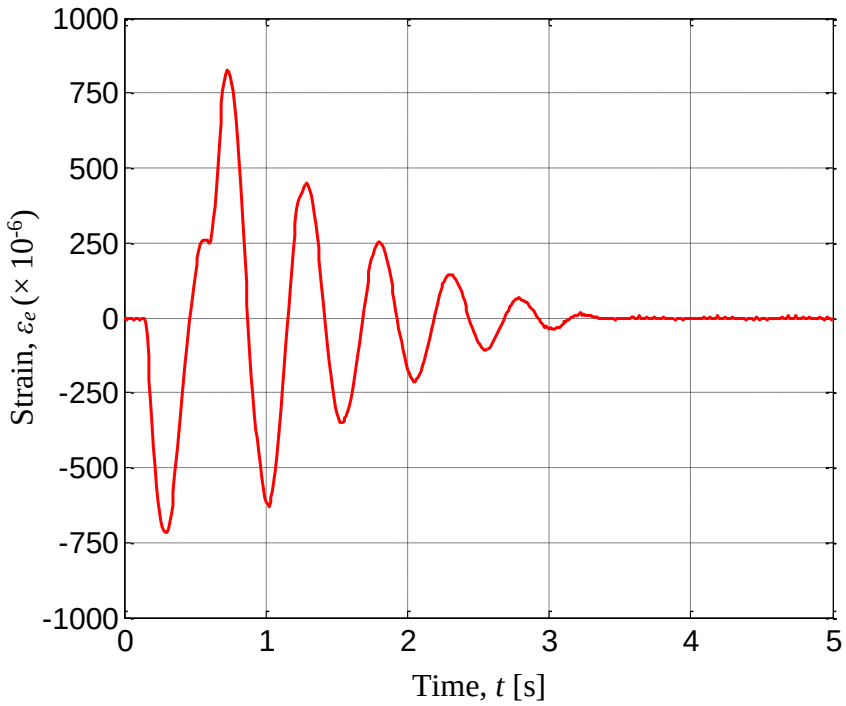

Fig. 5.9 Experimental time history response of strains due to the base excitation at 0.11 [m] from the origin of the two-link

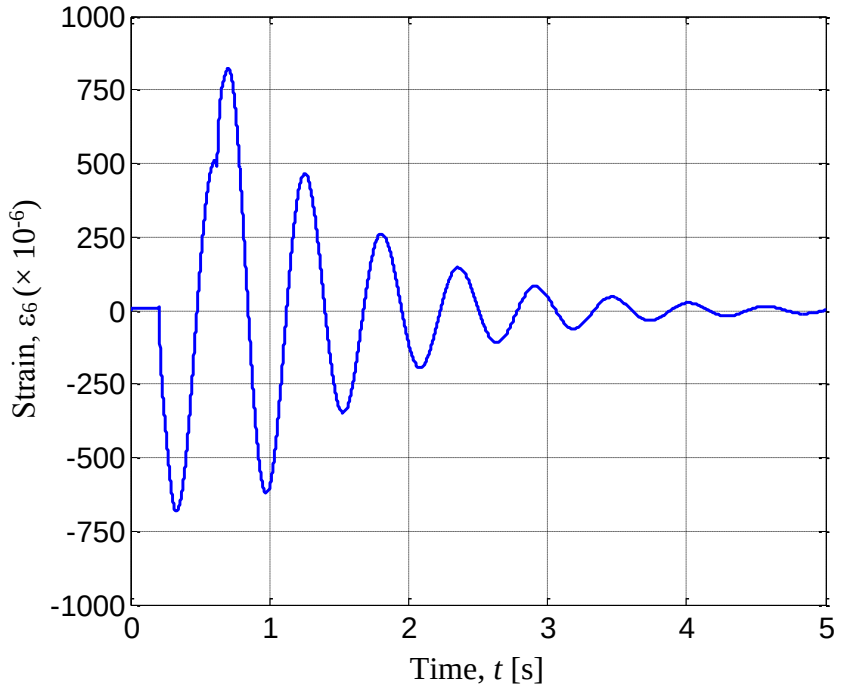

Fig. 4.22 Calculated time history response of strains due to base excitation at Node 6 of Model C2.1 (previously shown in Page 86)

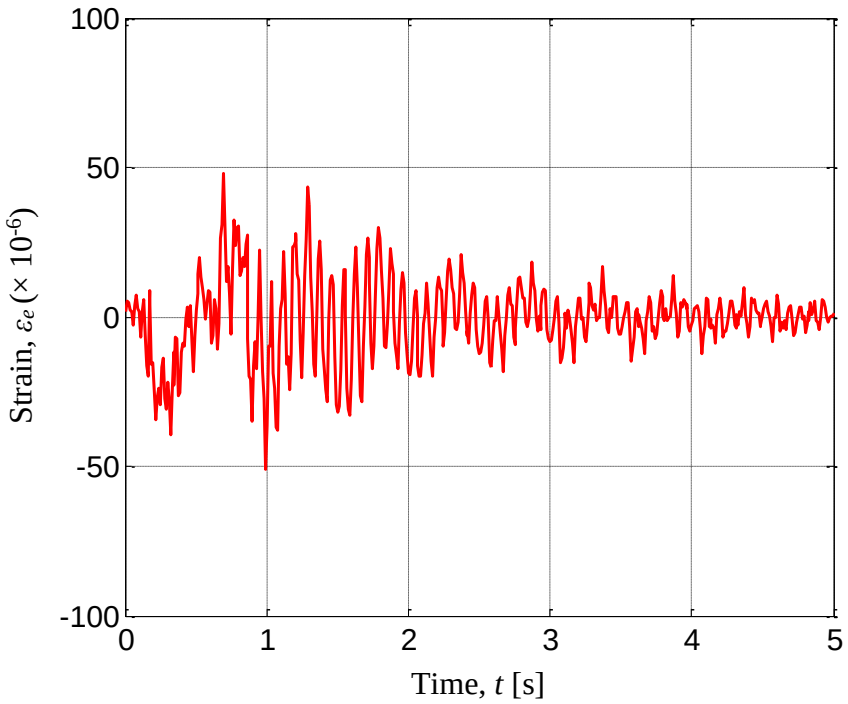

Fig. 5.10 Experimental time history response of strains due to the base excitation at 0.38 [m] from the origin of the two-link

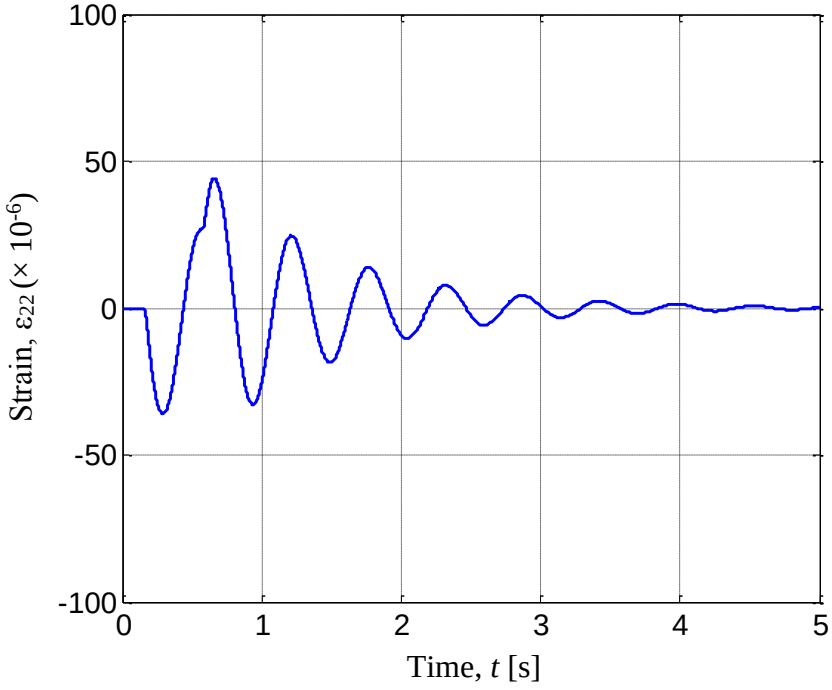

Fig. 4.23 Calculated time history response of strains due to base excitation at Node 22 of Model C2.1 (previously shown in Page 87)

5.6.4 Time History Responses on Uncontrolled and Controlled System for Model E2.2

Experimental time history responses of the strains on the uncontrolled and controlled systems were measured using Model E2.2 when first and second motors rotated by the angle of $\pi/4$ radian (45 degrees) and $\pi/2$ radians (90 degrees) within 0.50 [s], respectively. Experimental time history responses of strains on the controlled system were measured under three control strategies shown in Figs. 4.10 to 4.12.

Furthermore, the experimental proportional, proportional-derivative and active-force gains that are non-dimensional gains, K_p', K_d' and K_{pa}' were examined. The examination of gains leaded to K_p' = 300 [-], K_d' = 0.3 [-] and K_{pa}' = 1.1 [-], as the better ones. Figures 5.11 to 5.14 show the experimental uncontrolled and controlled time history responses of strains at position of 0.11 [m], respectively. The maximum and minimum strains of uncontrolled system at position of 0.11 [m] from the link's origin in positive and negative sides were 954.10×10^{-6} and -836.60×10^{-6}, as shown in Fig. 5.11. By using P-controller they became 763.30×10^{-6} and -707.20×10^{-6}, as shown in Fig. 5.12. By using PD-controller they became 613.10×10^{-6} and -644.10×10^{-6}, as shown in Fig. 5.13. Moreover, by using AF-controller they became 624.40×10^{-6} and -694.50×10^{-6}, as shown in Fig. 5.14

Then, Figs. 5.15 to 5.18 show the experimental uncontrolled and controlled time history responses of strains at position of 0.38 [m], respectively. The maximum and minimum strains of uncontrolled system at position of 0.38 [m] from the link's origin in positive and negative sides were 55.51×10^{-6} and -54.55×10^{-6}, as shown in Fig. 5.15. By using P-controller they became 61.25×10^{-6} and -63.16×10^{-6}, as shown in Fig. 5.16. By using PD-controller they became 39.34×10^{-6} and -54.56×10^{-6}, as shown in Fig. 5.17.

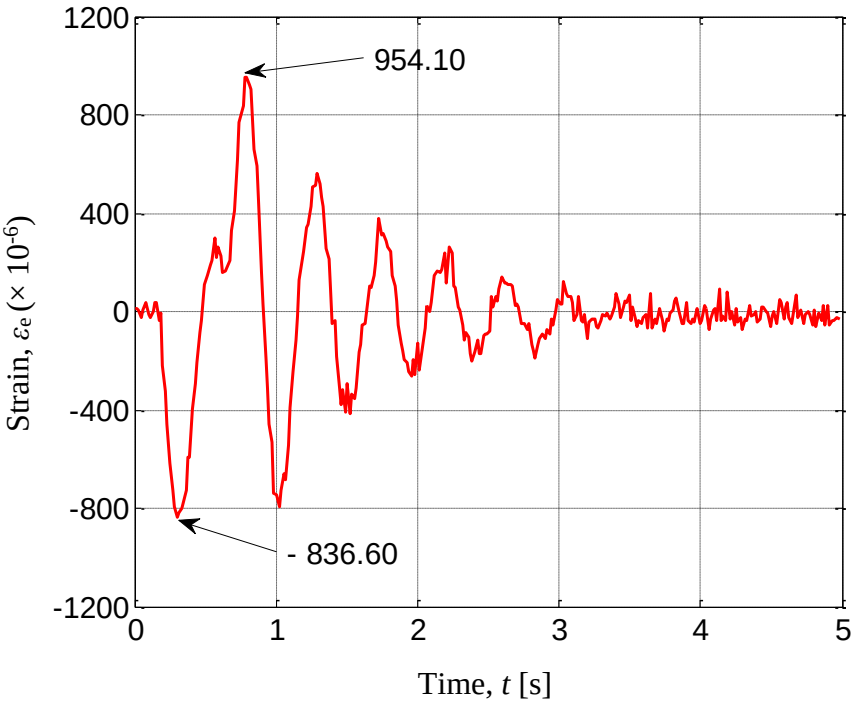

Fig. 5.11 Experimental time history response of strains at 0.11 [m] from the origin of the link for uncontrolled Model E2.2 due to base excitation

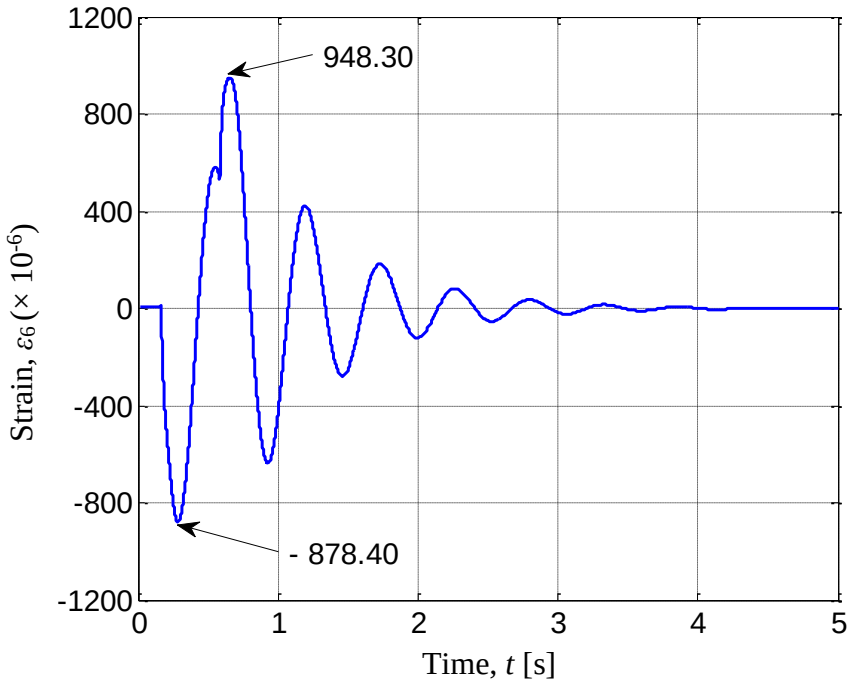

Fig. 4.24 Calculated time history response of strains at Node 6 for uncontrolled Model C2.2 due to base excitation (previously shown in Page 88)

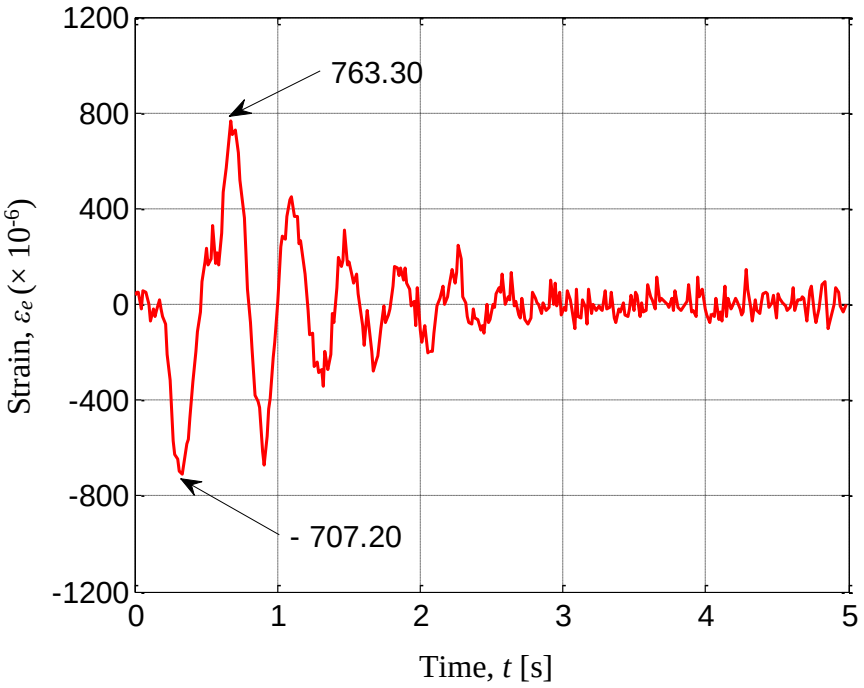

Fig. 5.12 Experimental time history response of strains for controlled Model E2.2 at 0.11 [m] from the origin of the link due to base excitation using P-controller (K_p' = 300 [-])

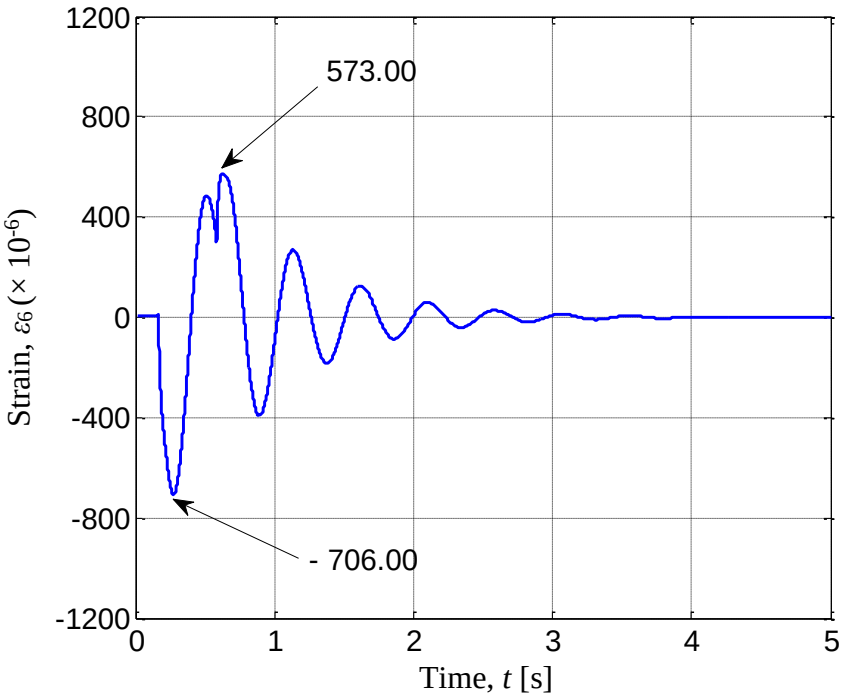

Fig. 4.25 Calculated time history response of strains at Node 6 for controlled Model C2.2 due to base excitation using P-controller (K_p = 2 [Nm]) (previously shown in Page 88)

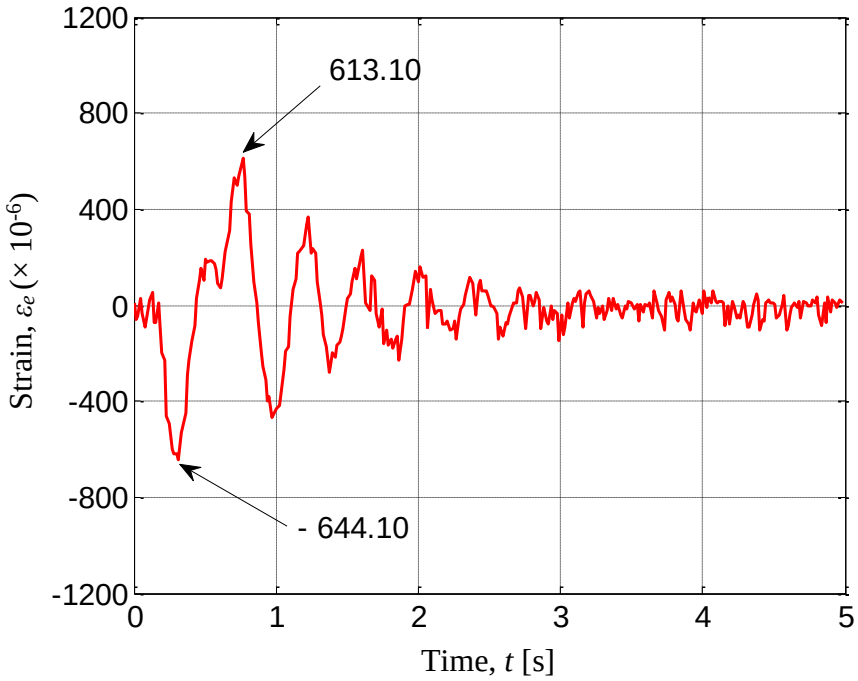

Fig. 5.13 Experimental time history response of strains for controlled Model E2.2 at 0.11 [m] from the origin of the link due to base excitation using PD-controller (K_p' = 300 [-], K_d' = 0.3 [-])

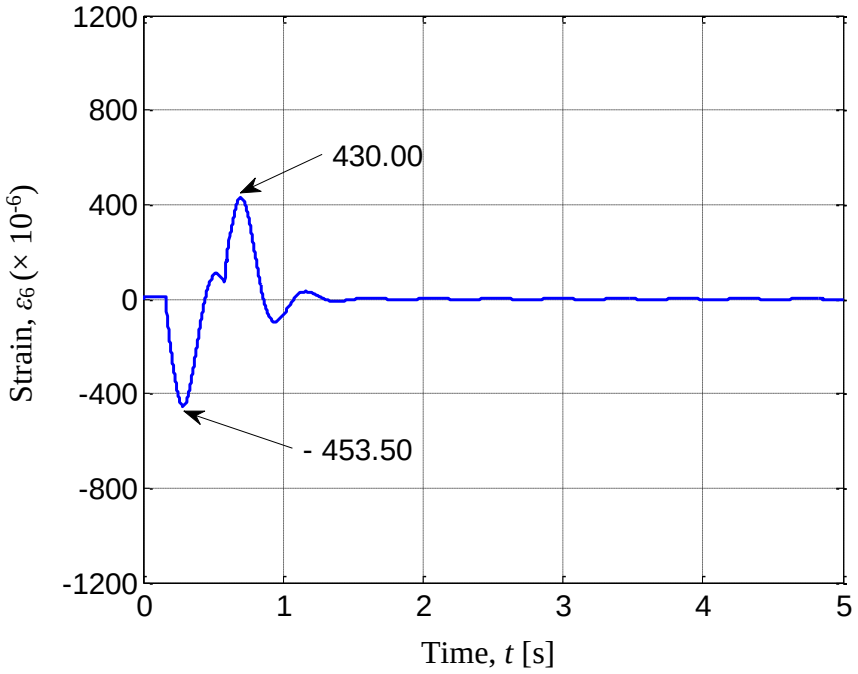

Fig. 4.26 Calculated time history response of strains at Node 6 for controlled Model C2.2 due to base excitation using PD-controller (K_p = 2 [Nm], K_d = 0.6 [Nms]), (previously shown in Page 89)

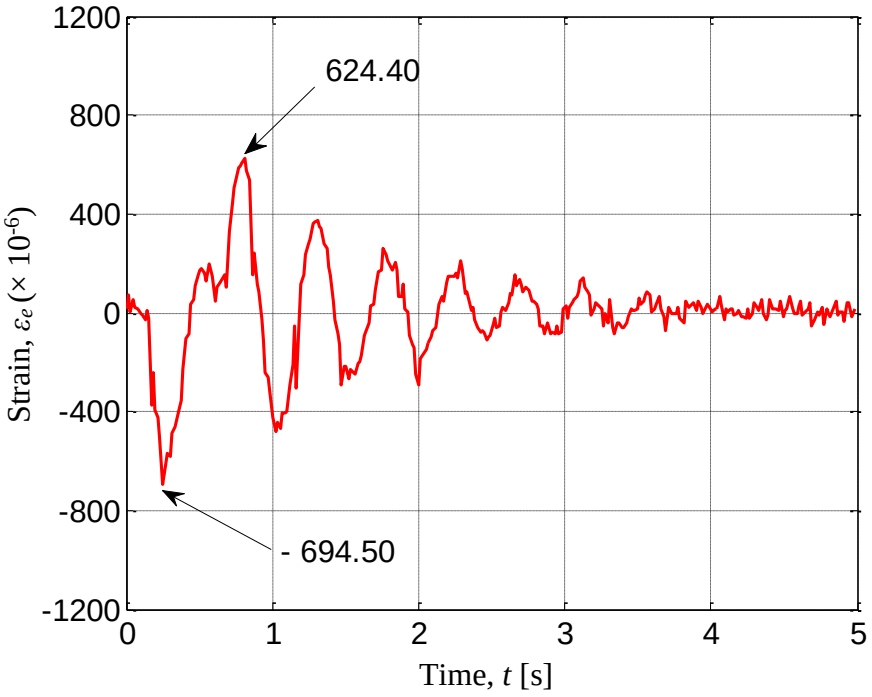

Fig. 5.14 Experimental time history response of strains for controlled system at 0.11 [m] from the origin of the link due to base excitation using AF-controller (K_{pa}' = 1.1 [-])

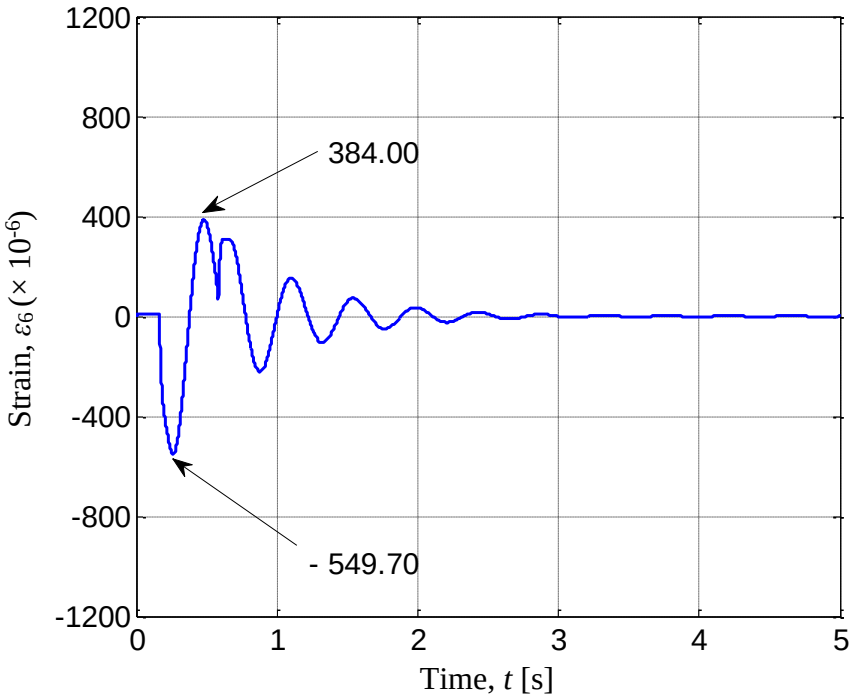

Fig. 4.27 Calculated time history response of strains at Node 6 for controlled Model C2.2 due to base excitation using AF-controller (K_{pa} = 0.02 [-]), (previously shown in Page 89)

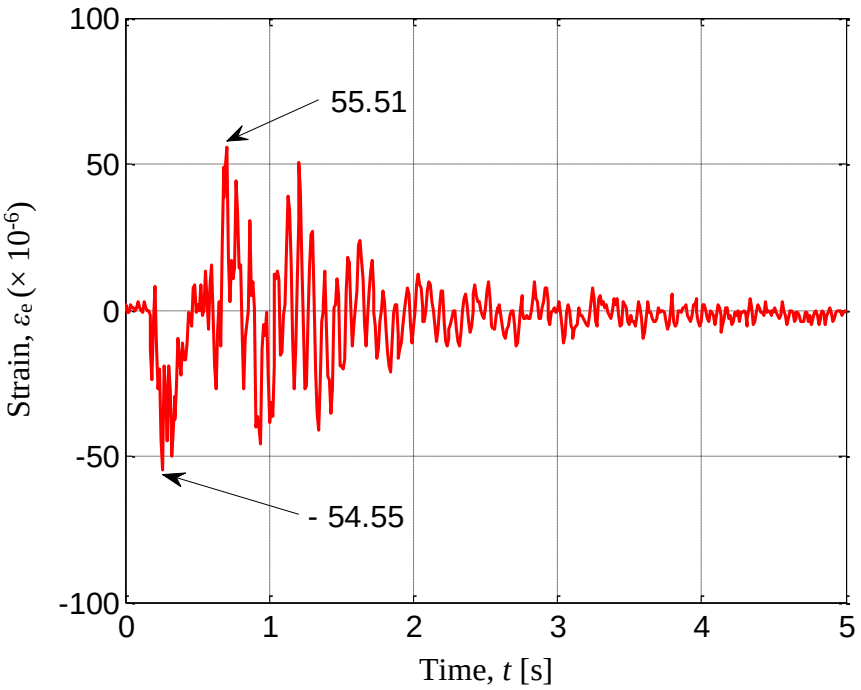

Fig. 5.15 Experimental time history response of strains at 0.38 [m] from the origin of the link for uncontrolled Model E2.2 due to base excitation

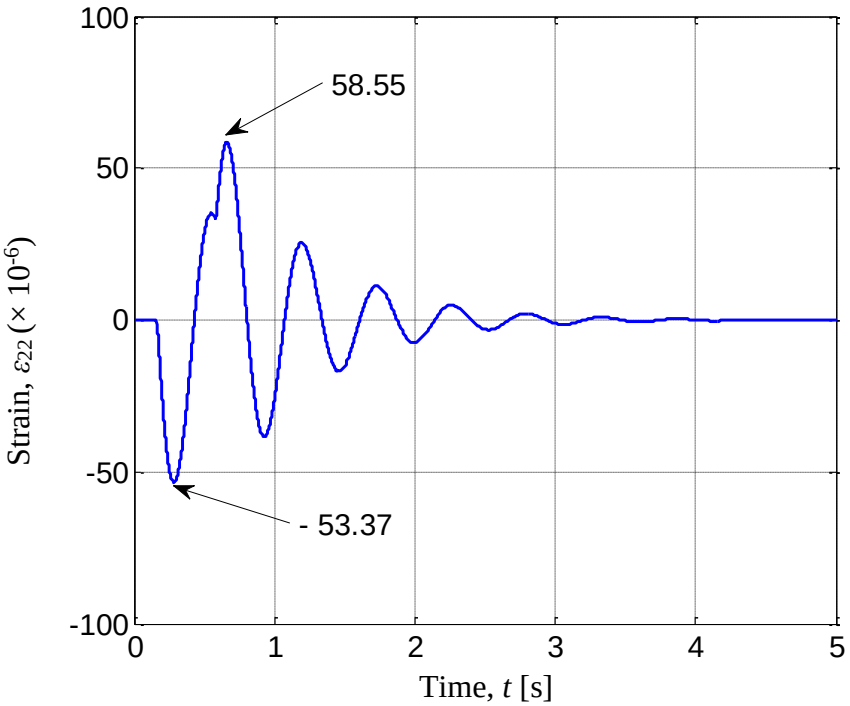

Fig. 4.28 Calculated time history response of strains at Node 22 for uncontrolled Model C2.2 due to base excitation (previously shown in Page 90)

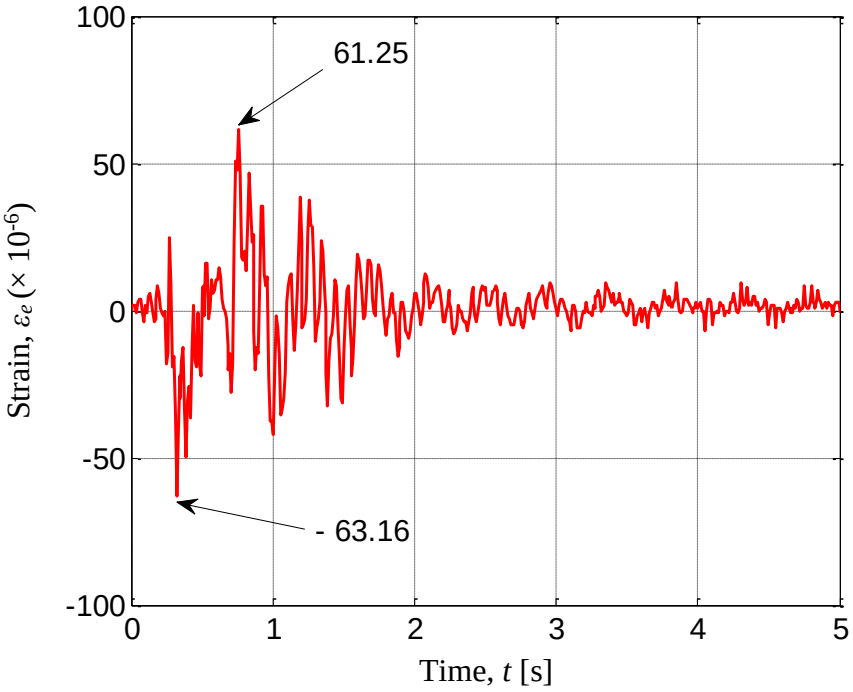

Fig. 5.16 Experimental time history response of strains for controlled Model E2.2 at 0.38 [m] from the origin of the link due to base excitation using P-controller (K_p' = 300 [-])

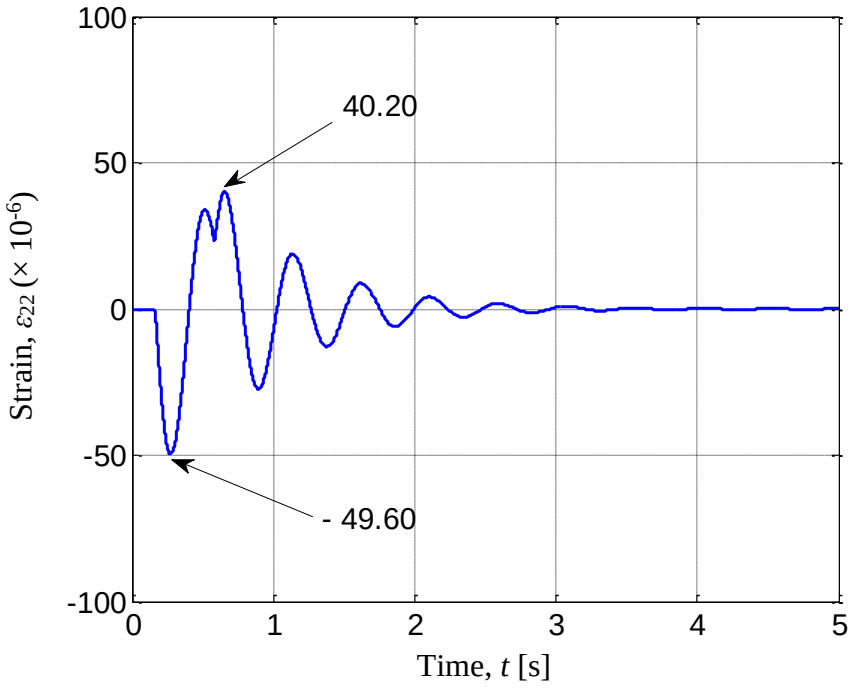

Fig. 4.29 Calculated time history response of strains at Node 22 for controlled Model C2.2 due to base excitation using P-controller (K_p = 2 [Nm]), (previously shown in Page 90)

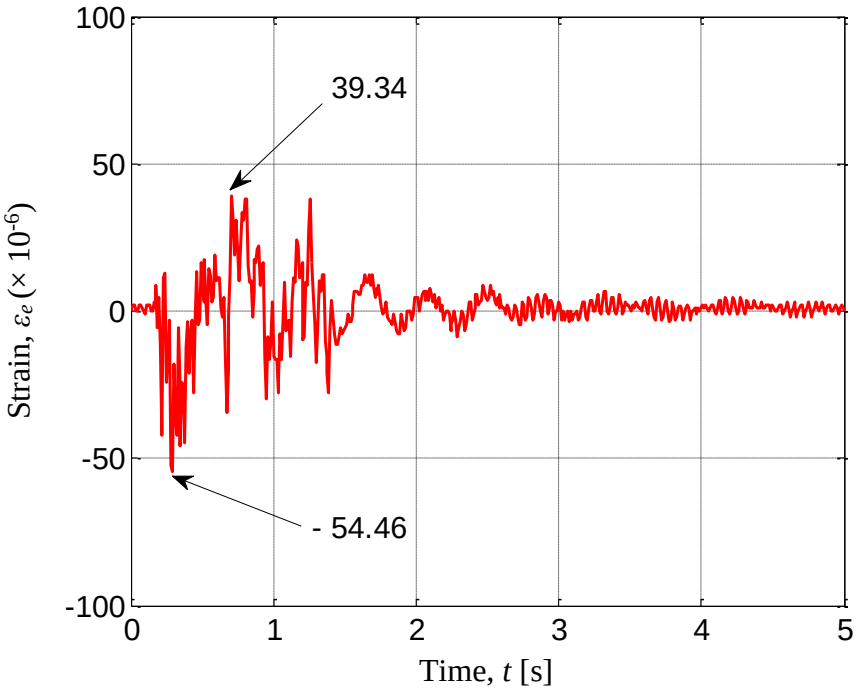

Fig. 5.17 Experimental time history response of strains for controlled Model E2.2 at 0.38 [m] from the origin of the link due to base excitation using PD-controller (K_p' = 300 [-], K_d' = 0.3 [-])

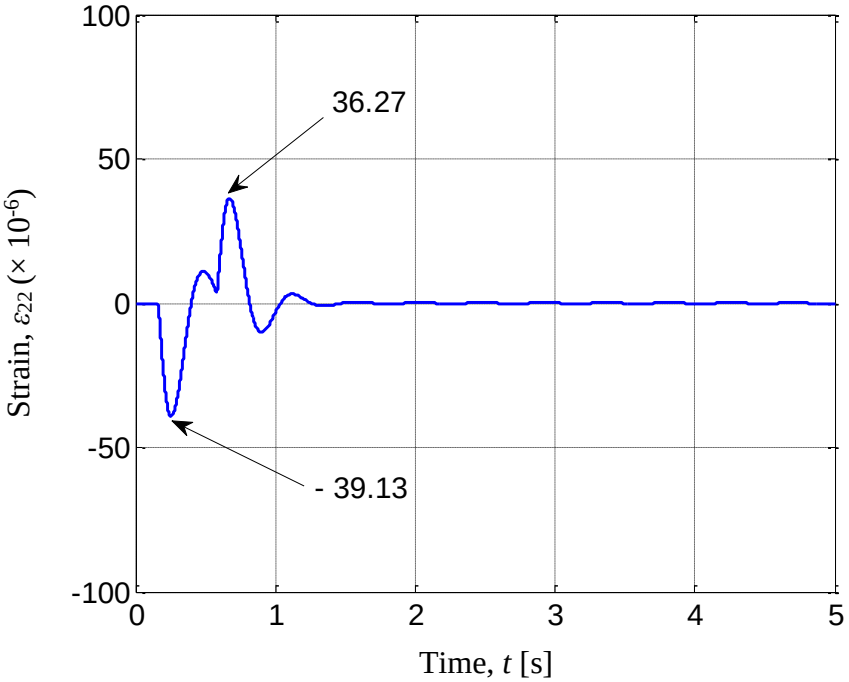

Fig. 4.30 Calculated time history response of strains at Node 22 for controlled Model C2.2 due to base excitation using PD-controller (K_p = 2 [Nm], K_d = 0.6 [Nms]), (previously shown in Page 91)

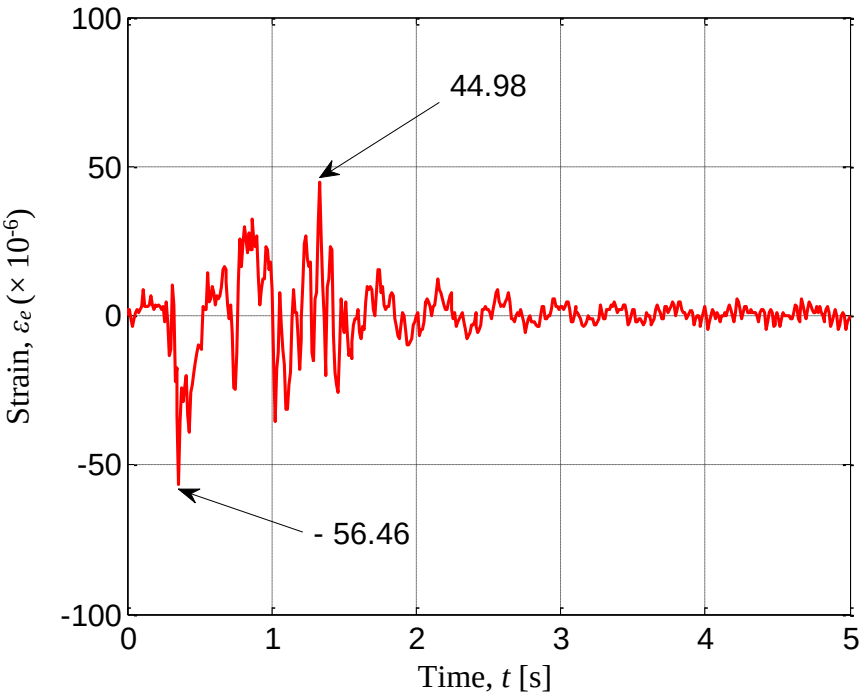

Fig. 5.18 Experimental time history response of strains for controlled Model E2.2 at 0.38 [m] from the origin of the link due to base excitation using AF-controller (K_{pa}' = 1.1 [-])

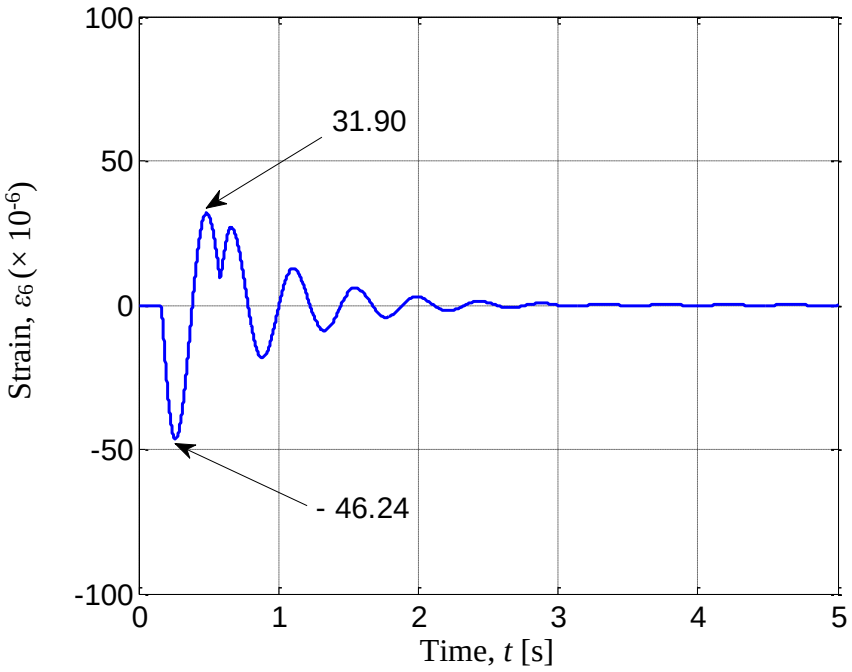

Fig. 4.31 Calculated time history response of strains at Node 22 for controlled Model C2.2 due to base excitation using AF-controller (K_{pa} = 0.02 [-]), (previously shown in Page 91)

Moreover, by using AF-controller they became 44.98×10^{-6} and -56.46×10^{-6}, as shown in Fig. 5.18. It can be observed on Figs. 5.11 to 5.18 that the PD-controller is more effective compared to the P and AF ones to suppress the vibration of the flexible two-link manipulator.

Furthermore, as shown in Chapter 4, Figs. 4.24 to 4.27 and 4.28 to 4.31 show the uncontrolled and controlled calculated time history response of strains at Nodes 6 and 22 of Model C2.2, respectively. The calculated results on the controlled system were obtained using the same control strategies used in the experiments. The Experimental and calculated results for uncontrolled and controlled system show the effectiveness and validity of the proposed control scheme and strategies to suppress the vibration of the flexible two-link manipulator.

5.6.5 Time History Responses on Uncontrolled and Controlled System for Model E2.3

Experimental time history responses of the strains on the uncontrolled and controlled systems were measured using Model E2.3 when first and second motors rotated by the angle of $\pi/4$ radian (45 degrees) and $\pi/2$ radians (90 degrees) within 0.50 [s], respectively. Mass of the end-effector used in the experiments is 14.49 [g]. Experimental time history responses of strains on the controlled system were measured under three control strategies shown in Figs. 4.10, 4.11 and 4.12.

Furthermore, the experimental proportional, proportional-derivative and active-force gains that are non-dimensional gains, K_p', K_d' and K_{pa}' were examined. The examination of gains leaded to K_p' = 300 [-], K_d' = 0.3 [-] and K_{pa}' = 1.1 [-], as the better ones. Figures 5.19 to 5.22 show the experimental uncontrolled and controlled

time history responses of strains at position of 0.11 [m], respectively. The maximum and minimum strains of uncontrolled system at position of 0.11 [m] from the link's origin in positive and negative sides were 1298.10×10^{-6} and -1156.00×10^{-6}, as shown in Fig. 5.19. By using P-controller they became 1064.00×10^{-6} and -939.32×10^{-6}, as shown in Fig. 5.20. By using PD-controller they became 1029.00×10^{-6} and -904.70×10^{-6}, as shown in Fig. 5.21. Moreover, by using AF-controller they became 1036.00×10^{-6} and -911.60×10^{-6}, as shown in Fig. 5.22.

Then, Figs. 5.23 to 5.26 show the experimental uncontrolled and controlled time history responses of strains at position of 0.38 [m], respectively. The maximum and minimum strains of uncontrolled system at position of 0.38 [m] from the link's origin in positive and negative sides were 350.50×10^{-6} and -198.10×10^{-6}, as shown in Fig. 5.23. By using P-controller they became 352.20×10^{-6} and -201.00×10^{-6}, as shown in Fig. 5.24. By using PD-controller they became 348.40×10^{-6} and -197.10×10^{-6}, as shown in Fig. 5.25. Moreover, by using AF-controller they became 349.30×10^{-6} and -198.10×10^{-6}, as shown in Fig. 5.26. It can be observed on Figs. 5.11 to 5.18 that the PD-controller is more effective compared to the P and AF ones to suppress the vibration of the flexible two-link manipulator.

Furthermore, as shown in Chapter 4, Figs. 4.40 to 4.43 and 4.44 to 4.47 show the uncontrolled and controlled calculated time history response of strains at Nodes 6 and 22 of Model C2.4, respectively. The calculated results on the controlled system were obtained using the same control strategies used in the experiments. The Experimental and calculated results for uncontrolled and controlled system show the effectiveness and validity of the proposed control scheme and strategies to suppress the vibration of the flexible two-link manipulator.

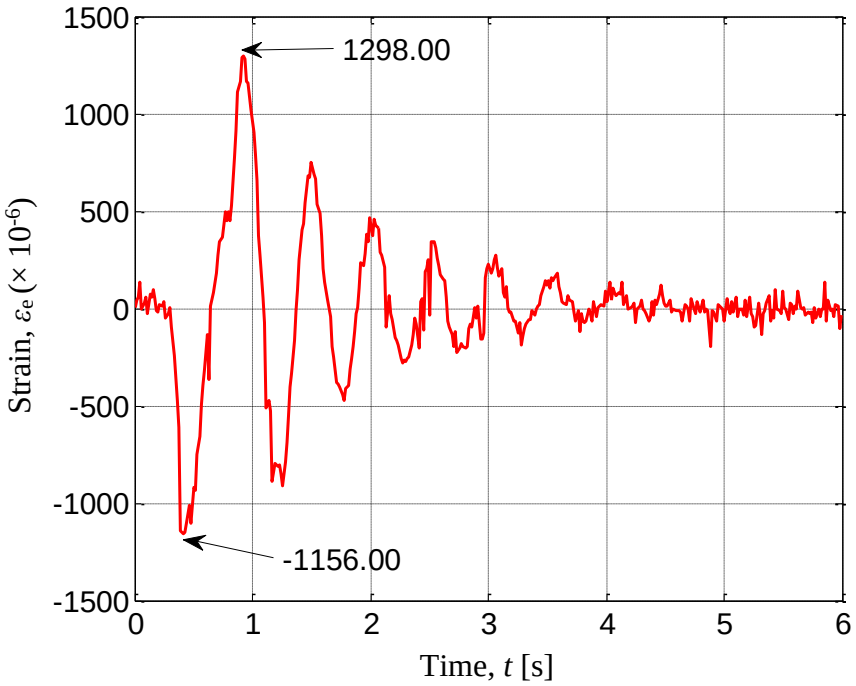

Fig. 5.19 Experimental time history response of strains at 0.11 [m] from the origin of the link for uncontrolled Model E2.3 due to base excitation

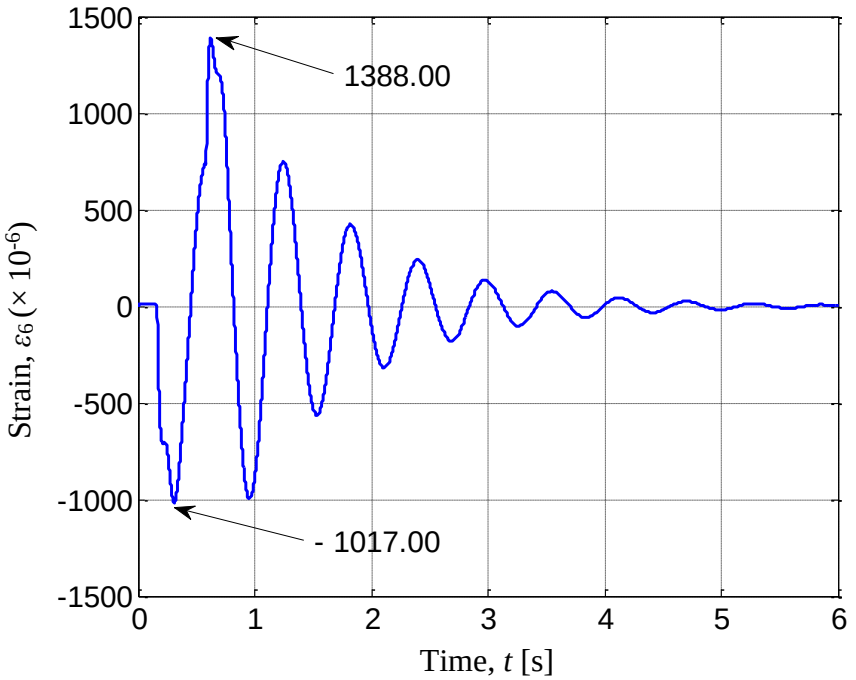

Fig. 4.40 Calculated time history response of strains at Node 6 for uncontrolled Model C2.4 due to base excitation (previously shown in Page 98)

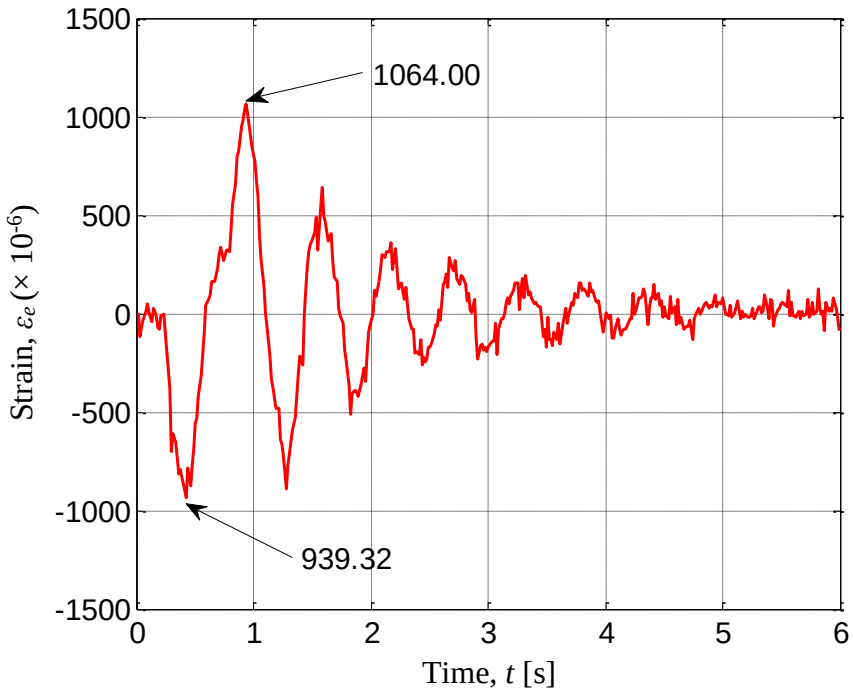

Fig. 5.20 Experimental time history response of strains for controlled Model E2.3 at 0.11 [m] from the origin of the link due to base excitation using P-controller (K_p' = 300 [-])

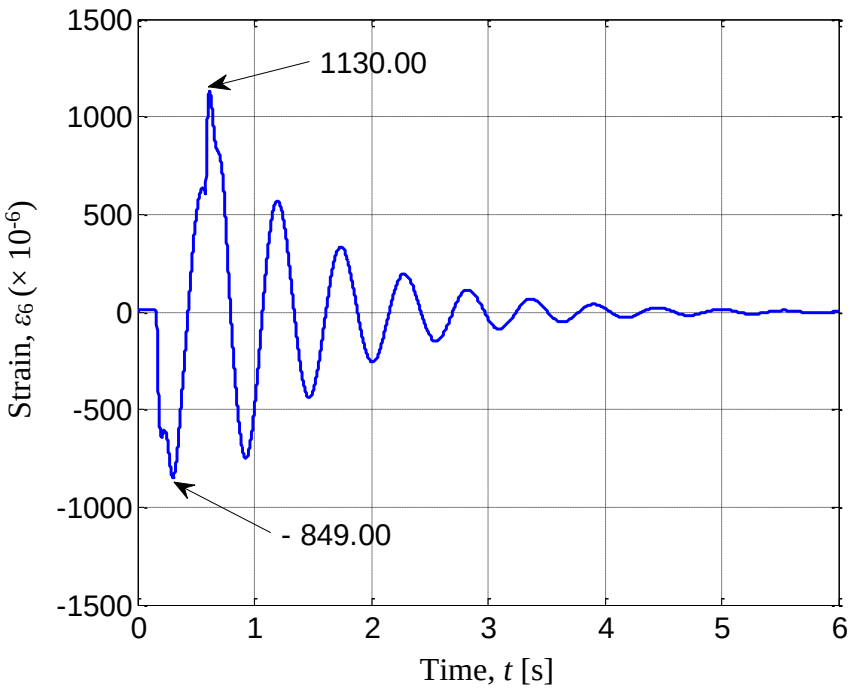

Fig. 4.41 Calculated time history response of strains at Node 6 for controlled Model C2.4 due to base excitation using P-controller (K_p = 2 [Nm]), (previously shown in Page 98)

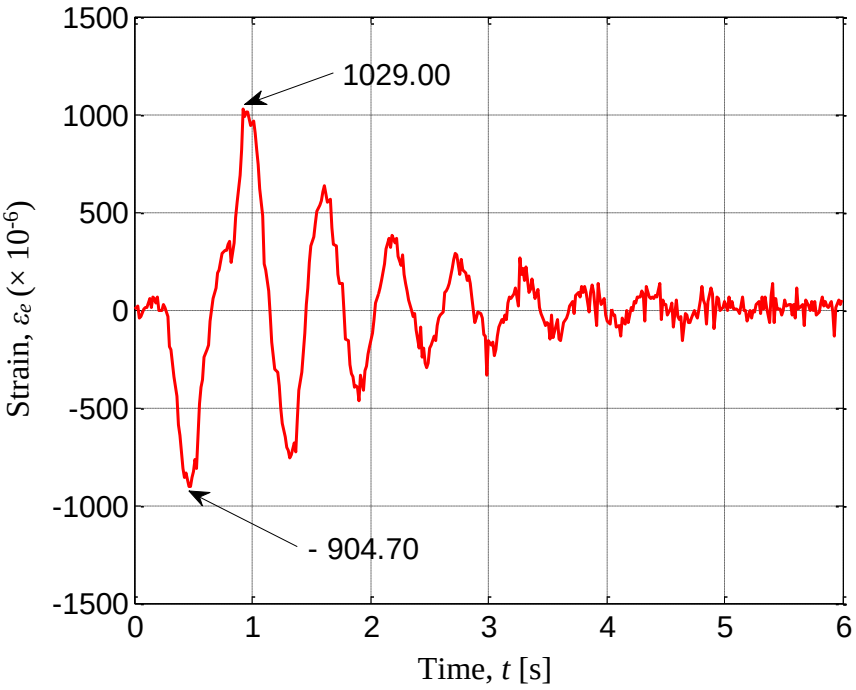

Fig. 5.21 Experimental time history response of strains for controlled Model E2.3 at 0.11 [m] from the origin of the link due to base excitation using PD-controller (K_p' = 300 [-], K_d' = 0.3 [-])

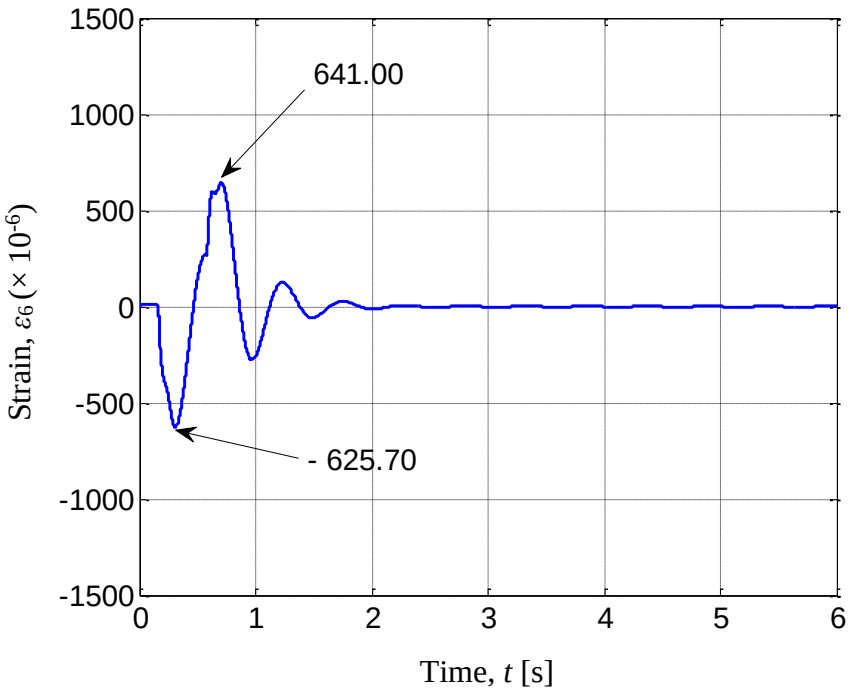

Fig. 4.42 Calculated time history response of strains at Node 6 for controlled Model C2.4 due to base excitation using PD-controller (K_p = 2 [Nm], K_d = 0.6 [Nms]), (previously shown in Page 99)

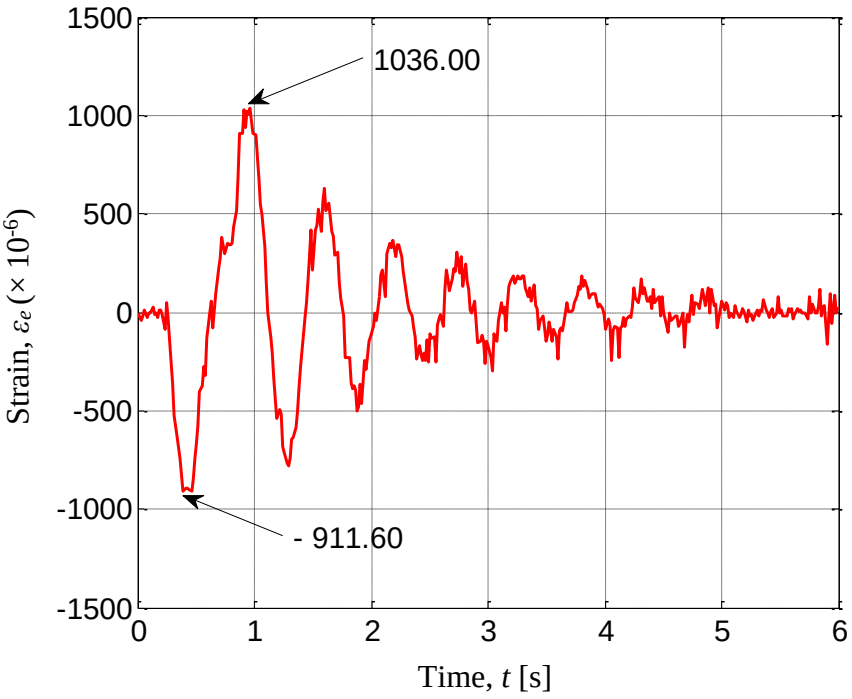

Fig. 5.22 Experimental time history response of strains for controlled system at 0.11 [m] from the origin of the link due to base excitation using AF-controller (K_{pa}' = 1.1 [-])

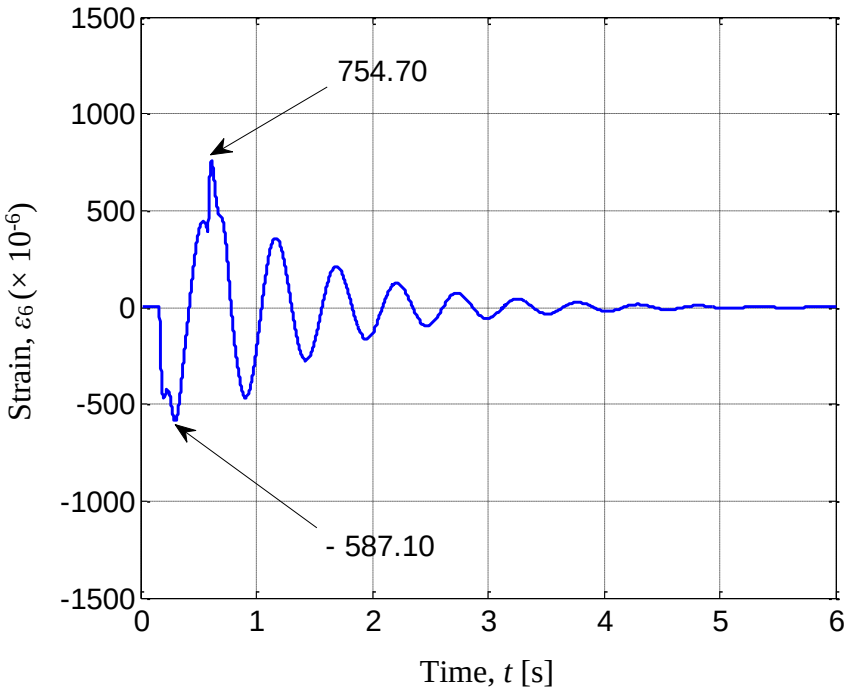

Fig. 4.43 Calculated time history response of strains at Node 6 for Controlled Model C2.4 due to base excitation using AF-controller (K_{pa} = 0.02 [-]), (previously shown in Page 99)

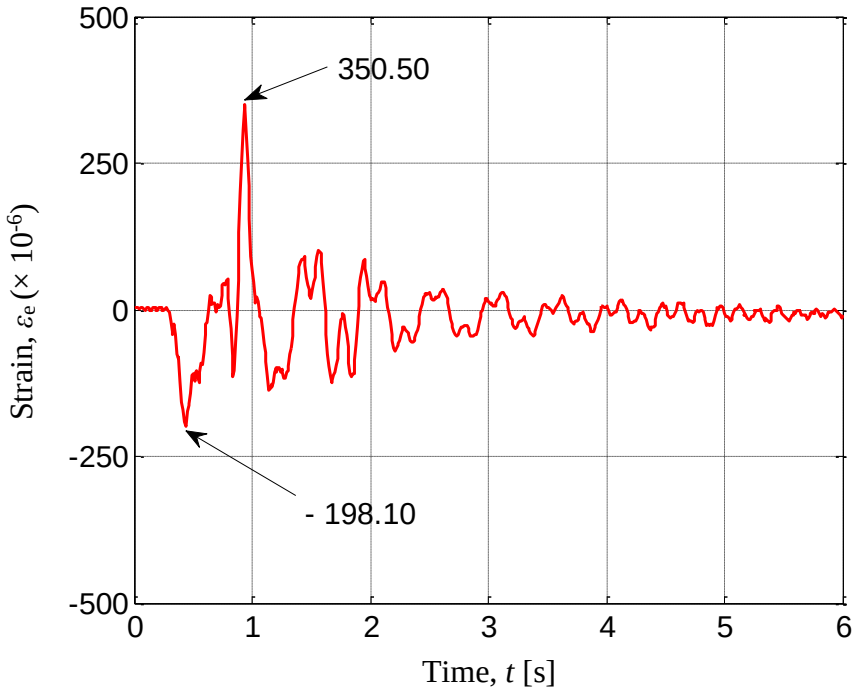

Fig. 5.23 Experimental time history response of strains at 0.38 [m] from the origin of the link for uncontrolled Model E2.3 due to base excitation

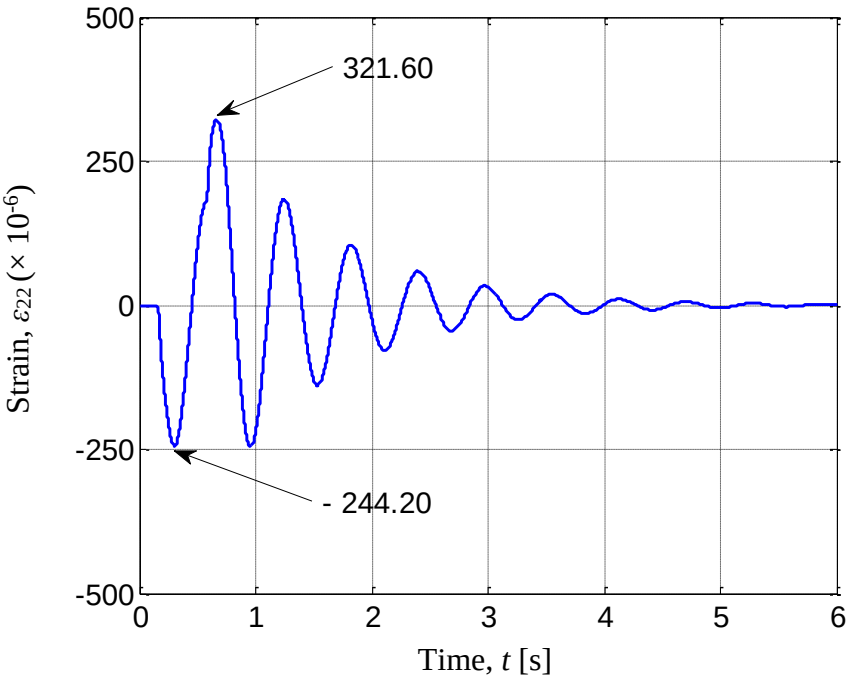

Fig. 4.44 Calculated time history response of strains at Node 22 for uncontrolled Model C2.4 due to base excitation (previously shown in Page 100)

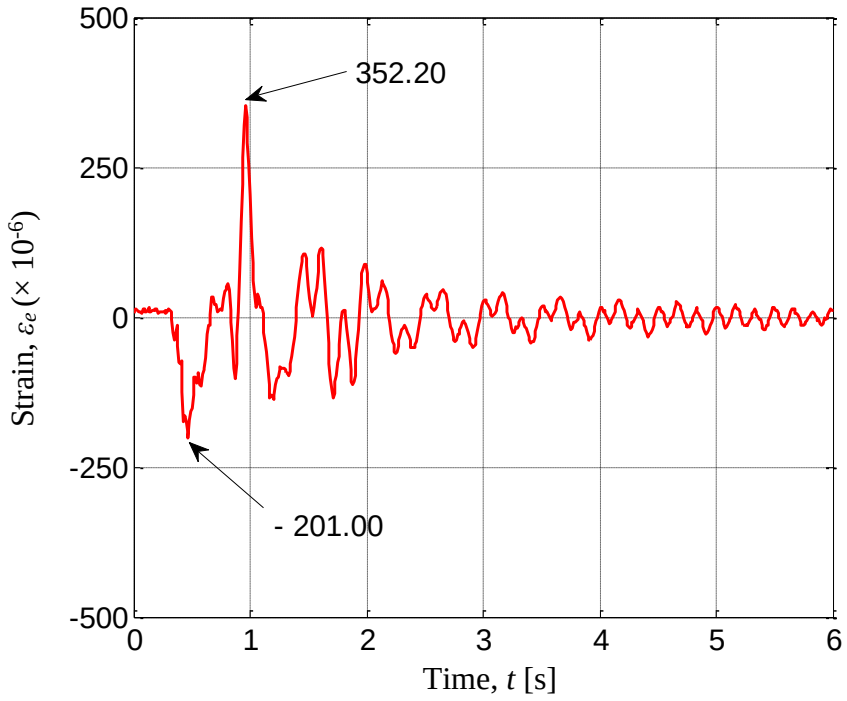

Fig. 5.24 Experimental time history response of strains for controlled Model E2.3 at 0.38 [m] from the origin of the link due to base excitation using P-controller (K_p' = 300 [-])

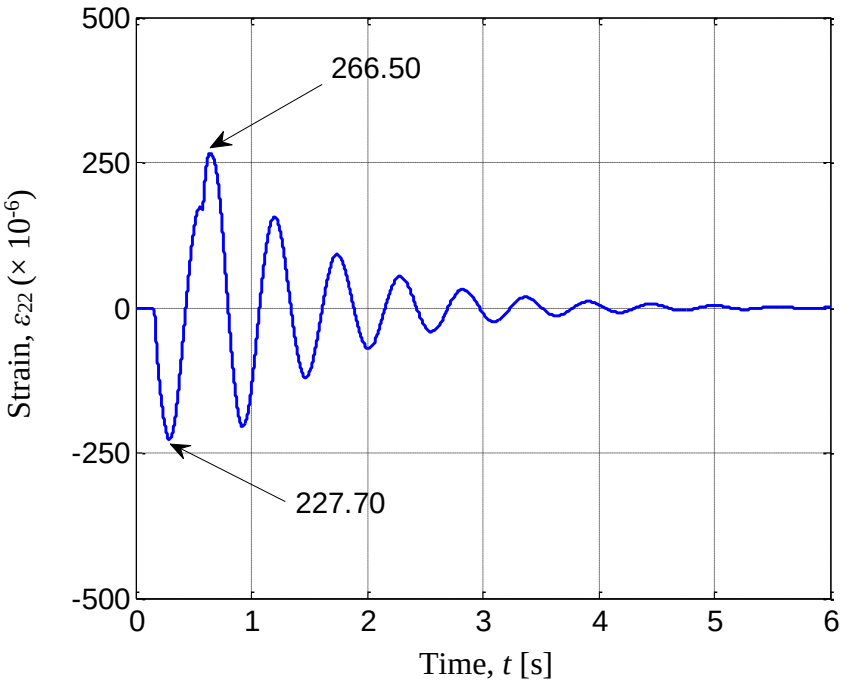

Fig. 4.45 Calculated time history response of strains at Node 22 for controlled Model C2.3 due to base excitation using P-controller (K_p = 2 [Nm]), (previously shown in Page 100)

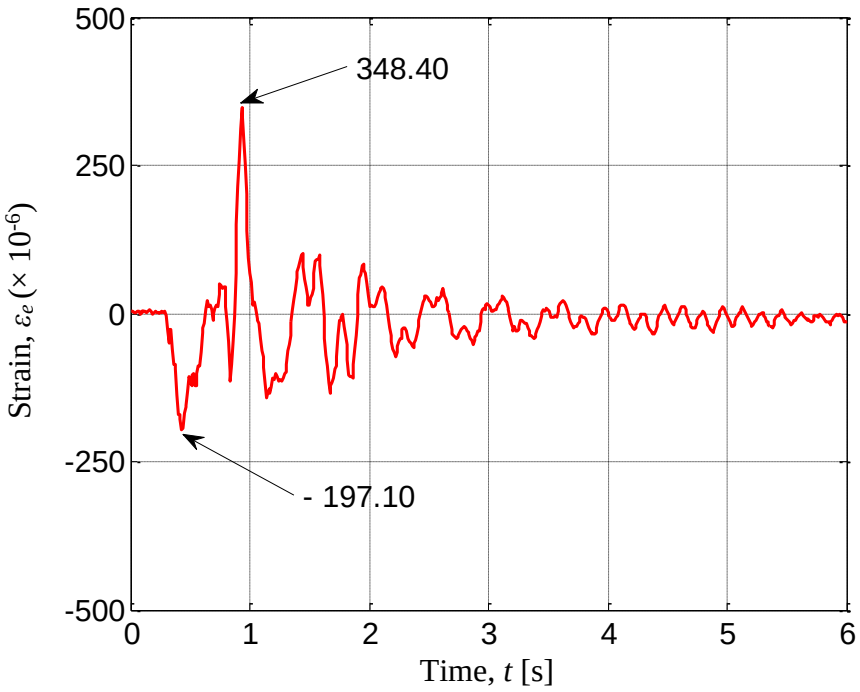

Fig. 5.25 Experimental time history response of strains for controlled Model E2.3 at 0.38 [m] from the origin of the link due to base excitation using PD-controller (K_p' = 300 [-], K_d' = 0.3 [-])

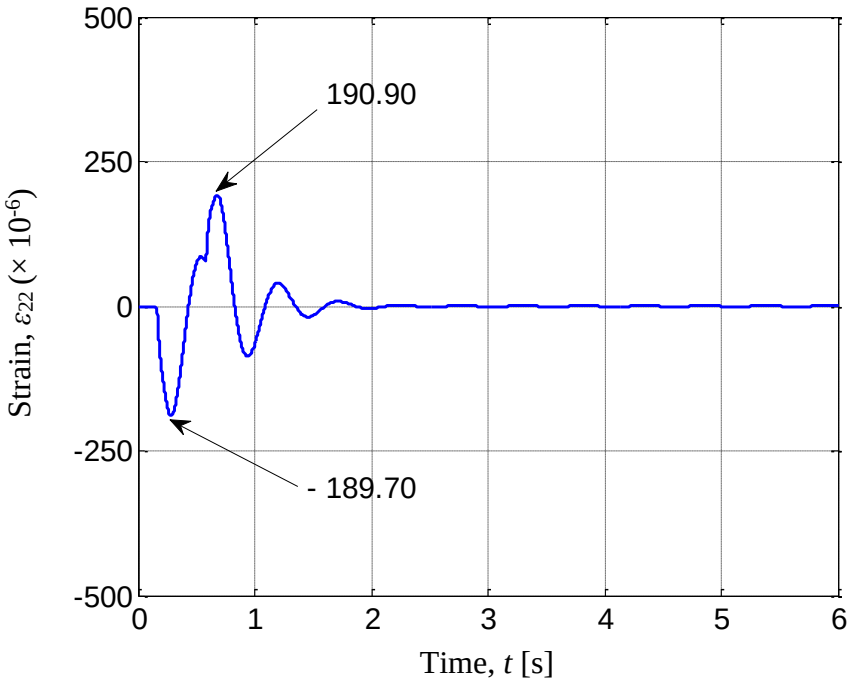

Fig. 4.46 Calculated time history response of strains at Node 22 for controlled Model C2.2 due to base excitation using PD-controller (K_p = 2 [Nm], K_d = 0.6 [Nms]), (previously shown in Page 101)

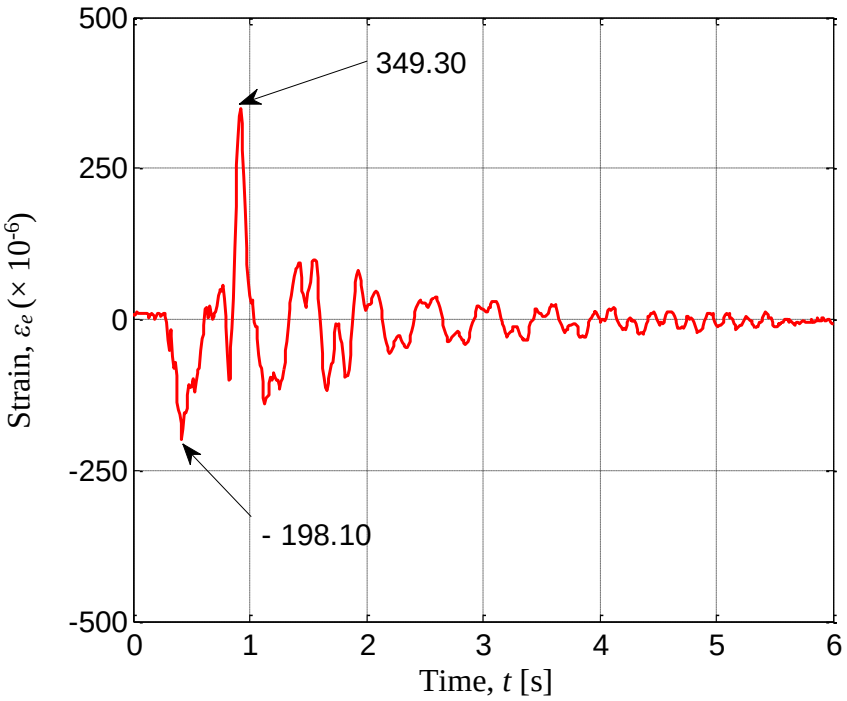

Fig. 5.26 Experimental time history response of strains for controlled Model E2.3 at 0.38 [m] from the origin of the link due to base excitation using AF-controller (K_{pa}' = 1.1 [-])

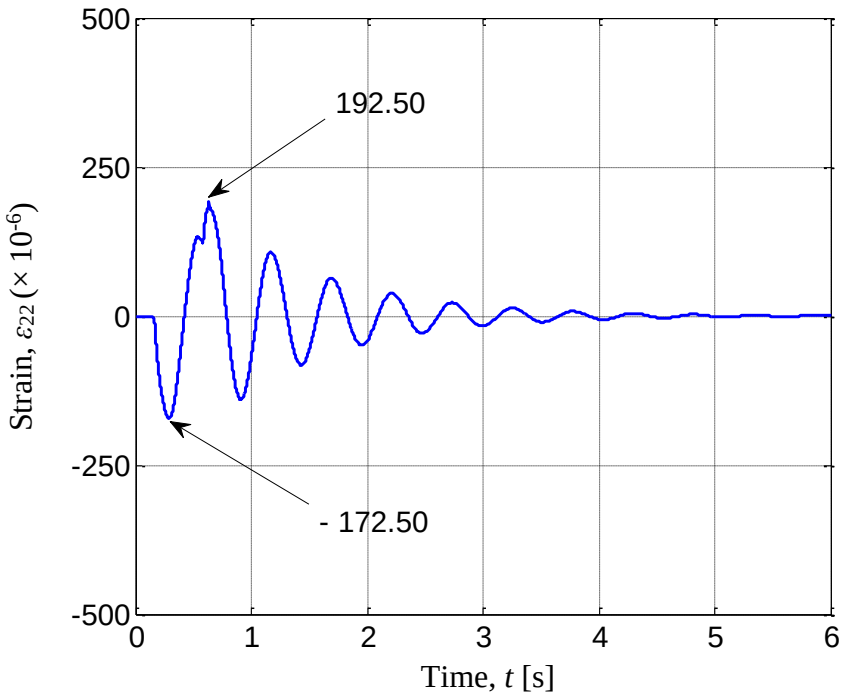

Fig. 4.47 Calculated time history response of strains at Node 22 for Controlled Model C2.4 due to base excitation using AF-controller (K_{pa} = 0.02 [-]), (previously shown in Page 101)

5.7 Conclusions

Experimental models and set-up had been developed in order to carry out dynamic experiments of the flexible two-link system. Experimental results on time history responses and natural frequencies show the validity of the formulation, computational codes and modeling of the system. The proportional (P), proportional-derivative (PD) and active-force (AF) controls were implemented to suppress the vibration of the system. Their performances were compared through the experiments. Experimental results on controlled system show the validity of the proposed control scheme and strategies as well as the effectiveness of the proposed PD-control compared to the P and AF ones to suppress the vibration of the flexible two-link manipulator.

Chapter 6

Conclusions

A modeling technique and control scheme with proportional, proportional-derivative and active-force controls using finite element method to suppress vibrations of flexible manipulators had been proposed in this research. The modeling technique and control scheme had been implemented on flexible single-link and two-link manipulators and confirmed through experiments.

The equations of motion for the flexible single-link manipulator had been derived using the finite element method. Computational codes had been developed in order to perform dynamic simulations of the system. Calculated results on time history responses, natural frequencies and vibration modes have been presented. The proportional (P), proportional-derivative (PD) and active-force (AF) controls strategies were designed to suppress the vibration of the system. Their performances were compared through the calculations. Based on the calculated results, the effect of D-controller was very small compare to P-controller, therefore using a P-controller will be sufficient for experiment. The calculated results show the superiority of the proposed AF control compared to the P and PD ones to suppress the vibration of the flexible single-link manipulator.

Experimental models and set-up had been developed in order to carry out dynamic experiments of the flexible single-link system. Experimental results on time history responses and natural frequencies show the validity of the formulation, computational

codes and modeling of the system. The proportional (P) and active-force (AF) controls were implemented to suppress the vibration of the system. Their performances were compared through the experiments. Experimental results on controlled system show the validity of the proposed control scheme and strategies as well as the superiority of the proposed AF control compared to the P one to suppress the vibration of the flexible single-link manipulator.

The equations of motion for the flexible two-link manipulator had been derived using the finite element method. Computational codes had been developed in order to perform dynamic simulations of the system. Calculated results on time history responses, natural frequencies and vibration modes have been presented. The proportional (P), proportional-derivative (PD) and active-force (AF) controls strategies were designed to suppress the vibration of the system. Their performances were compared through the calculations. Based on the calculated results, the effect of the second piezoelectric actuator was small not significant compare to the first one. Therefore, using one piezoelectric actuator will be sufficient for experiment. The calculated results have been revealed that the proposed control scheme can effectively suppress the vibration of the flexible two-link manipulator even though using only one piezoelectric actuator as well as the effectiveness of the proposed PD-control compared to the P and AF ones to suppress the vibration of the system.

Experimental models and set-up had been developed in order to carry out dynamic experiments of the flexible two-link system. Experimental results on time history responses and natural frequencies show the validity of the formulation, computational codes and modeling of the system. The proportional (P), proportional-derivative (PD) and active-force (AF) controls were implemented to suppress the vibration of the system.

Their performances were compared through the experiments. Experimental results on controlled system show the validity of the proposed control scheme and strategies as well as the effectiveness of the proposed PD-control compared to the P and AF ones to suppress the vibration of the flexible two-link manipulator.

References

[1] C. Nishidome, and I. Kajiwara, "Motion and Vibration Control of Flexible-link Mechanism with Smart Structure", *JSME International Journal*, Vol. 46, No. 2, 2003, pp. 565 – 571.

[2] K. Gurses et al, Vibration Control of a Single-link Flexible Manipulator Using an Array of Fiber Optic Curvature Sensors and PZT Actuators, *Mechatronics* 19, 2009, pp. 167 – 177.

[3] S. S. Ge et al, "A Nonlinear Feedback Controller for a Single-link Flexible Manipulator Based on a Finite Element Model", *Journal of Robotic Systems*, Vol. 14, No. 3, 1997, pp. 165 – 178.

[4] V. O. Gamarra-Rosado and E. A. O., Yuhara, "Dynamic Modeling and Simulation of a Flexible Robotic Manipulator", *Robotica*, Vol. 17, 1999, pp. 523 – 528.

[5] R. G. K. M. Aarts and J. B. Jonker, "Dynamic Simulation of Planar Flexible Link Manipulators Using Adaptive Modal Integration", *Multibody System Dynamic*, Vol. 7, 2002, pp. 31 – 50.

[6] M. O. Tokhi et al, "Dynamic Characterization of a Flexible Manipulator System", *Robotica*, Vol. 19, 2001, pp. 571 – 580.

[7] H. Du et al, "A Nonlinear Finite Element Model for Dynamics of Flexible Manipulators, *Mech. Mach. Theory* Vol. 31, No. 5, 1996, pp. 1109 – 1119.

[8] M. O. Tokhi and Z. Mohamed, “Finite Element Approach to Dynamic Modeling of a Flexible Robot Manipulator: Performance Evaluation and Computational Requirements”, *Communications in Numerical Methods in Engineering*, Vol. 15, 1999, pp. 669 – 678.

[9] M. H. Korayem et al, “Maximum Allowable Dynamic Load of Flexible Mobile Manipulators Using Finite Element Approarch”, *Int. J. Adv Manuf Technol*, Vol. 36, 2008, pp. 606 – 617.

[10] P. E. Gaultier and W. L. Cleghorn, “ A Spatially Translating and Rotating Beam Finite Element for Modeling Flexible Manipulators”, *Mech. Mach. Theory*, Vol. 27, No. 4, 1992, pp. 415 – 433.

[11] P. Kalra and A. M. Sharan, “Accurate Modeling of Flexible Manipulators Using Finite Element Analysis”, *Mech. Mach. Theory*, Vol. 26, No. 3, 1991, pp. 299 – 313.

[12] J. N. Bricout et al, “A Finite Element Model for the Dynamics of Flexible Manipulators”, *Mech. Mach. Theory*, Vol. 25, No. 1, 1990, pp. 119 – 128.

[13] H. S. Tsou and G. C. Wan, “Distributed Structural Dynamics Control of Flexible Manipulators - I: Structural Dynamics and Distributed Viscoelastic Actuator”, *Computer & Structures*, Vol. 35, No. 6. 1990, pp. 669 – 677.

[14] J.R. Hewit et al, “Active Force Control of a Flexible Manipulator by Distal Feedback”, *Mech. Mach. Theory*, Vol. 32, No. 5, 1997, pp. 583 – 596.

[15] B. Yushu et al, “Vibration Reduction of Open-chain Flexible Manipulators by Optimizing Independent Motion of Branch Links”, *Chinese Journal of Aeronautics*, Vol. 21, No. 1, 2008, pp. 79 – 85.

[16] B. Subhudi and A. S. Morris, "Soft Computing Methods Applied to the Control of a Flexible Robot Manipulator", *Applied Soft Computing*, Vol. 9, No. 1, 2009, pp. 149 – 158.

[17] M. S. Alam and M. O. Tokhi, "Designing Feedforward Command Shapers with Multi-Objectives Genetic Optimisation for Vibration Control of a Single-link Flexible Manipulator", *Engineering Applications of Artificial Intelligence*, Vol. 21, No. 2, 2008, pp. 229 – 246.

[18] Z. Mohamed et al, "Vibration Control of a Very Flexible Manipulator System", *Control Engineering Practice*, Vol. 13, No. 3, 2005, pp. 267 – 277.

[19] R. J. Theodore and A. Ghosal, "Robust Control of a Multilink Flexible Manipulators", *Mech. Mach. Theory*, Vol. 38, No. 4, 2003, pp. 367 – 377.

[20] M. Z. Md. Zain et al, "Hybrid Learning Control Schemes with Input Shaping of a Flexible Manipulator System", *Mechatronics*, Vol. 16, No. 3-4, 2006, pp. 209 – 219.

[21] Y. N. Hwang, "A new Approach for Dynamic Analysis of a Flexible Manipulator Systems", *International Journal of Non-Linear Mechanics*, Vol. 40, No. 6, 2005, pp. 925 – 938.

[22] M. Karkoub and K. Tamma, "Modeling and μ-synthesis Control of Flexible Manipulators", *Computer & Structures*, Vol. 79, No. 5, 2001, pp. 543 – 551.

[23] L. Tian and C. Collins, "Adaptive Neuro-Fuzzy Control of Flexible Manipulator", *Mechatronics*, Vol. 15, No. 10, 2005, pp. 1305 – 1320.

[24] M. Karkoub et al, "Robust Control of Flexible Manipulators via μ-synthesis", *Mechatronics*, Vol. 8, No. 7, 2000, pp. 725 – 734.

[25] M. K. Sundareshan and C. Askew, "Neural Network-Assisted Variable Control Scheme for Control of a Flexible Manipulator Arm", *Automatica*, Vol. 33, No. 9, 1997, pp. 1699 – 1710.

[26] J. S. Surdhar and A. S. White, "A Parallel Fuzzy-Controlled Flexible Manipulator Using Optical Tip Feedback", *Robotics and Computer-Integrated Manufacturing*, Vol. 19, No. 3, 2003, pp. 273 – 282.

[27] F. Khorrami et al, "Experimental Results on Adaptive Nonlinear Control and Input Preshaping for Multi-link Flexible Manipulators", *Automatica*, Vol. 31, No. 1, 1995, pp. 83 – 97.

[28] A. Konno and M. Uchiyama, "Vibration Suppression Control of Spatial Flexible Manipulators", *Control Engineering Practice*, Vol. 3, No. 9, 1995, pp. 1315 – 1321.

[29] P. Zhou et al, "Optimal Construction and Control of Flexible Manipulators: A Case Study Based on LQR Output Feedback", *Mechatronics*, Vol. 11, No. 1, 2001, pp. 59 – 77.

[30] X. Zhang and Y-Q. Yu, "Motion Control of Flexible Robot Manipulators via Optimizing Redundant", *Mech. Mach. Theory*, Vol. 36, No. 7, 2001, pp. 883 – 892.

[31] L. Tian and C. Collins, "A Dynamic Recurrent Neural Network-based Controller for a Rigid-flexible Manipulator System", *Mechatronics*, Vol. 14, No. 5, 2004, pp. 471 – 490.

[32] Z. Mohamed and M. O. Tokhi, "Command Shaping Techniques for Vibration Control of a Flexible Robot Manipulator", *Mechatronics*, Vol. 14, No. 1, 2004, pp. 69 – 90.

[33] H. Okayasu et al, "Development of Hydraulic-driven Flexible Manipulators for Neurosurgery", *International Congress Series*, Vol. 1256, 2003, pp. 607 – 612.

[34] P. Gasbarri et al, "Validation of Attitude/Defromation Sensing Techniques for Space Flexible Manipulators", *Acta Astronautica*, Vol. 64, No. 2-3, 2009, pp. 212 – 221.

[35] H-K. Kim et al, "Compliant Control of a Two-link Flexible Robot Featuring Piezoelectric Actuators", *Mech. Mach. Theory*, Vol. 36, No. 3, 2001, pp. 411 – 424.

[36] V. J. Modi et al, "On the Non-linear Dynamic of a Space Platform Based on Mobile Flexible Manipulators", *Acta Astronautica*, Vol. 32, No. 6, 1994, pp. 419 – 439.

[37] Y. L. Yao et al, "Maximum Allowable Load of Flexible Manipulators for Given Dynamic Trajectory", *Robotic and Computer-Integrated Manufacturing*, Vol. 10, No. 4, 1993, pp. 301 – 309.

[38] D. J. Latornell and D. B. Cherchas, "Force and Motion Control of Single Flexible Manipulator Link", *Robotic and Computer-Integrated Manufacturing*, Vol. 9, No. 2, 1992, pp. 87 – 99.

[39] C. Yhen et al, "Dynamic Analysis of a Two-link Flexible Manipulator System Using Extended Bond Graphs", *Journal of the Franklin Institute*, Vol. 330, No. 6, 1993, pp. 1113 – 1134.

[40] F. Karray et al, "Path Planning with Obstacle Avoidance as Applied to a Class of Space Based Flexible Manipulators", *Acta Astronautica*, Vol. 37, 1995, pp. 69 – 86.

[41] V. J. Modi et al, "A Composite Control Scheme for Joint Tracking and Active Vibration Suppression of Mobile Flexible Manipulator Systems", *Acta Astronautica*, Vol. 36, No. 5, 1995, pp. 261 – 270.

[42] J. K. Chan and V. J. Modi, "A Closed-form Dynamical Analysis of an Orbiting Flexible Manipulator", *Acta Astronautica*, Vol. 25, No. 2, 1991, pp. 67 – 75.

[43] F. Li et al, "Centralized, Decentralized, and Independent Control of a Flexible Manipulator on a Flexible Base", *Acta Astronautica*, Vol. 29, No. 3, 1993, pp. 159 – 168.

[44] K. Khorasani and P. V. Kokotovic, "Feedback Linearization of a Flexible Manipulator Near Its Rigid Body Manifold", *Systems and Control Letters*, Vol. 6, No. 3, 1985, pp. 187 – 192.

[45] Y-J. Lin and T-S. Lee, "Comprehensive Dynamic Modeling and Motion/Force Control of Flexible Manipulators", *Mechatronics*, Vol. 2, No. 2, 1992, pp. 129 – 148.

[46] D. Surdilovic and M. Vukobratovic, "Deflection Compensation for Large Flexible Manipulators", *Mech. Mach. Theory*, Vol. 31, No. 3, 1996, pp. 317 – 329.

[47] D. Surdilovic and M. Vukobratovic, "One Method for Efficient Dynamic Modeling of Flexible Manipulators", *Mech. Mach. Theory*, Vol. 31, No. 3, 1996, pp. 297 – 315.

[48] F. Xi and R. G. Fenton, "Special Configurations of Flexible Manipulators", *Mech. Mach. Theory*, Vol. 28, No. 6, 1993, pp. 795 – 807.

[49] F. Boyer and P. Coiffet, "Symbolic Modeling of a Flexible Manipulator via Assembling of Its Generalized Newton Euler Model", *Mech. Mach. Theory*, Vol. 31, No. 6, 1993, pp. 795 – 807.

[50] M. Pascal, "Dynamic Analysis of a Flexible Manipulator Arm", *Acta Astronautica*, Vol. 21, No. 3, 1990, pp. 161 – 169.

[51] H. Bremen and F. Pfeiffer, "Experiments with Flexible Manipulator Arm", *Control Engineering Practice*, Vol. 3, No. 9, 1995, pp. 1331 – 1338.

[52] W-H. Jee and C-W. Lee, "H_∞ Robust Control of Flexible Manipulator Vibration by Using a Piezoelectric-type Servo-damper", *Control Engineering Practice*, Vol. 2, No. 3, 1994, pp. 421 – 430.

[53] S. Choura and A. S. Yigit, "Control of a Two-Link Rigid-Flexible Manipulator with a Moving Payload Mass", *Journal of Sound and Vibration*, Vol. 243, No. 5, 2001, pp. 883 – 897.

[54] K. Liu and X. Sun, "System Identification and Model Reduction for a Single-link Flexible Manipulator", *Journal of Sound and Vibration*, Vol. 242, No. 5, 2001, pp. 867 – 891.

[55] M. H. Korayem and A. Basu, "Automatic Fast Symbolic Modeling of Robotics Manipulator with Compliant Links", *Mathematical and Computer Modeling*, Vol. 22, No. 9, 1995, pp. 41 – 55.

[56] R-F. Fung and H-C. Chang, "Dynamic Modeling of a Non-linearly Constrained Flexible Manipulator with a Tip Mass by Hamilton's Principle", *Journal of Sound and Vibration*, Vol. 216, No. 5, 1998, pp.751 – 769.

[57] R. I. Milford and S. F. Asokanthan, "Configuration Dependent Eigenfrequencies for a Two-link Flexible Manipulator: Experimental Verification", *Journal of Sound and Vibration*, Vol. 222, No. 2, 1999, pp.191 – 207.

[58] M. P. Coleman and L. A. McSweeney, "Analysis and Computation of the Vibration Spectrum of the Cartesian Flexible Manipulator", *Journal of Sound and Vibration*, Vol. 274, No. 1-2, 2004, pp. 445 – 454.

[59] F-Y. Wang and G. Guan, "Influences of Rotary Inertia, Shear and Loading on Vibrations of Flexible Manipulator", *Journal of Sound and Vibration*, Vol. 171, No. 4, 1994, pp. 433 – 452.

[60] S-B. Choi et al, "Vibration Control Robust to Parameter Variations in a Very Flexible Manipulator Fabricated from Composite Laminates", *Journal of Sound and Vibration*, Vol. 162, No. 2, 1994, pp. 195 – 207.

[61] P. P. Coleman, "vibration Eigenfrequency Analysis of a Single-link Flexible Manipulator", *Journal of Sound and Vibration*, Vol. 212, No. 1, 1998, pp. 109 – 120.

[62] N. Popplewell and D. Chang, "Influence of an Off-set Payload on a Flexible Manipulator", *Journal of Sound and Vibration*, Vol. 190, No. 4, 1996, pp. 721 – 725.

[63] A. Shchuka and A. A. Goldenberg, "Tip Control of a Single-link Flexible Arm Using a Feedforward Technique", *Mech. Mach. Theory*, Vol. 24, No. 5, 1989, pp. 439 – 455.

[64] M. Tokhi et al, "Digital Signal Processing and Parallel Processing in the Real-time Simulation of a Flexible Manipulator System", *Mechanical Systems and Signal Processing*, Vol. 10, No. 6, 1996, pp. 729 – 745.

[65] E. M. Nebot et al, "Identification of a Flexible Manipulator Using Neural Networks", *Control Engineering Practice*, Vol. 2, No. 5, 1994, pp. 583 – 586.

[66] D. K. Anand et al, "Adaptive Control of a Flexible Manipulator with Varying Payload", *Control Engineering Practice*, Vol. 2, No. 5, 1994, pp. 567 – 570.

[67] F. Matsumo and T. Asano, "Modeling and Quasi-static Hybrid Position/force Control of a Two-link Flexible Manipulators", *Control Engineering Practice*, Vol. 2, No. 5, 1994, pp. 887 – 892.

[68] M. Lalanne et al, *Mechanical Vibration for Engineers*, John Wiley & Sons Ltd, 1983, pp. 146 – 153.

[69] B. R. Khan, “Active Vibration Control of Flexible Manipulators Using Piezoelectric Actuators”, *Master Thesis, Robotics Laboratory-Ehime University*, 2014, p. 29.

[70] http://www.rex-rental.jp/hkr/pcd-300a.html

List of Papers, a Book and an Award

International Journals (Full papers with reviews)

1. **"**Computational Simulations and Experiments on Vibration Control of a Flexible Two-link Manipulator Using a Piezoelectric Actuator", A.K. Muhammad, S. Okamoto, J.H. Lee, *Engineering Letters*, Vol. 23, No. 3, pp. 200-209, 2015.
2. "Comparisons of Proportional-derivative and Active-force Controls on Vibration Control of a Flexible Single-link Manipulator Using Finite-element Method", A.K. Muhammad, S. Okamoto, J.H. Lee, *International Journal of Artificial Life and Robotics*, Vol. 19, No. 4, pp. 375-381, 2014.
3. "Comparisons of Proportional and Active-force Controls on Vibration Control of a Flexible Link Manipulator Using a Piezoelectric Actuator through Calculations and Experiments", A.K. Muhammad, S. Okamoto, J.H. Lee, *Engineering Letters*, Vol. 22, No. 3, pp. 134-141, 2014.

Proceedings of International Conferences (Full papers with reviews)

1. "Computational Simulations on Vibration Control of a Flexible Two-link Manipulator by Piezoelectric Actuators Using Finite-element Method", A.K. Muhammad, S. Okamoto, J.H. Lee, *Proceeding of APCEAS (Asia-Pasific Conference on Engineering and Applied Sciences)*, pp. 173-188, Osaka, Japan, August 2015.

2. “Computational Simulations and Experiments on Vibration Control of a Flexible Link Manipulator Using a Piezoelectric Actuator”, A.K. Muhammad, B.R. Khan, S. Okamoto, J.H. Lee, *Proceedings of IMECS (the International MultiConference of Engineers and Computer Scientists) 2014*, Vol. 1, pp. 262-267, Hong Kong, March 2014.
3. “Computer Simulations on Vibration Control of a Flexible Single-link Manipulator Using Finite-element Method”, A.K. Muhammad, S. Okamoto, J.H. Lee, *Proceeding of the 19th International Symposium on Artificial Life and Robotics (AROB 19th 2014)*, pp. 381-386, Beppu, Japan, January 2014

Proceedings of Domestic Conferences

1. “Development and Vibration Control of a Flexible Single-link Manipulator Using a Piezoelectric Actuator”, A.K. Muhammad, S. Okamoto, J.H. Lee, *Proceeding of SICE (Society of Instrumentation and Control Engineers), Shikoku Branch, 2014*, pp. 139-144, Matsuyama, Japan, November 2014.
2. “Computer Simulation of a Vibration Control Scheme for a Flexible Single-link Manipulator Using Finite-element Method”, A.K. Muhammad, S. Okamoto, J.H. Lee, *Proceeding of SICE (Society of Instrumentation and Control Engineers), Shikoku Branch, 2014*, pp. 199-203, Takamatsu, Japan, November 2013.

Book (The First Chapter)

"Transactions on Engineering Technologies: International MultiConference of Engineers and Computer Scientists 2014", *Chapter 1: Active-force Control on Vibration of a Flexible Single-link Manipulator Using a Piezoelectric Actuator*, pp. 1-15, A.K. Muhammad, S. Okamoto, J.H. Lee, Published by Springer.

Award

Best Student Paper Award: IMECS 2014, *IAENG (International Association of Engineers) International Conference on Control and Automation*, Hong Kong, 12-14 March 2014.

Acknowledgments

Be grateful and all glory to the Almighty God ALLAH SWT for having given a great opportunity to carry out this research. Salawat is addressed to Rasulullah SAW.

Expression of gratitude is deservedly given to Directorate General of Higher Education of Indonesia, the State Polytechnic of Ujung Pandang and Ehime University for having given the opportunity to be a doctoral student in Robotic Laboratory-Ehime University. Great and special thanks go to Prof. Shingo Okamoto and Assoc. Prof. Jae Hoon Lee for their guidance support and being a helpful main supervisor and co-supervisor to me.

A big appreciation and gratitude is surely addressed to my parents, my wife and my children for their endless support, care, love, patience and prays. Finally, special thanks are expressed to B. R. Khan as member of the research team and all members of Robotics Laboratory-Ehime University, my relatives and friends who support me during the period of this study.

Curriculum Vitae

Name	: Abdul Kadir Muhammad
Place/Date of Birth	: Parepare, Indonesia / April 2, 1975
Gender	: Male
Education Background	
1. Master (M.Eng)	: Control System Engineering (Mechatronics), HAN Univeristy of Applied Sciences, Netherlands, (2007-2009).
2. Bachelor (B.Sc)	: Mechanical Engineering (Mechanical Design), Hasanuddin University, Indonesia (1994-1999).
Occupation	: Lecturer
Institution	: State Polytechnic of Ujung Pandang, Indonesia
Department	: Mechanical Engineering
Study Program	: Mechatronics
Personal Email Address	: kadir_muhammad@yahoo.co.id